ACS Photonics

pubs.acs.org/journal/apchd5

Review

Nonlinear Dielectric Nanoantennas and Metasurfaces: Frequency Conversion and Wavefront Control

Gustavo Grinblat*

Cite This: https://doi.org/10.1021/acsphotonics.1c01356

Read Online

ACCESS | Metrics & More | Article Recommendations

ABSTRACT: High-index dielectric nanostructures can support optical resonances of electric and magnetic character with ultralow linear absorption. In contrast to plasmonics, they can be engineered to confine electromagnetic fields inside the resonator, amplifying intrinsic nonlinearities of the dielectric. In this Review I examine the ability of dielectric nanoantennas and metasurfaces for efficient harmonic generation and wave-mixing processes, as well as nonlinear wavefront manipulation of the incident and radiated light. A detailed comparison is made between the many nanoscopic dielectric configurations reported in the literature, evaluating the influence of the material, crystal symmetry, structure geometry, and the different resonances involved (electric and magnetic Mie modes, Fano resonances, and quasi-nonradiative states, including anapoles and quasi-bound states in the continuum). The nonlinear performance of the nanosystems is analyzed, with emphasis on frequency conversion efficiency and emission directionality control, also discussing recent advances in nonlinear imaging, nonlinear holography, and all-optical switching. The role of topology in nonlinear nanophotonics is reviewed in the end, and potential future directions in the field are laid out.

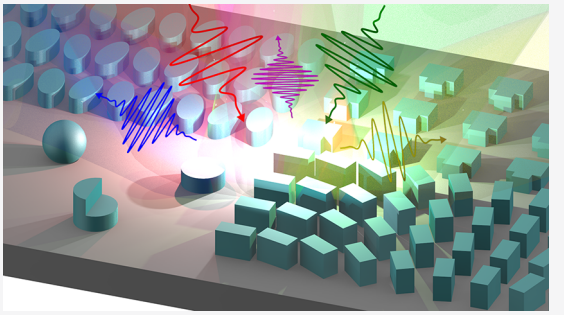

KEYWORDS: *dielectric nanophotonics, nonlinear optics, harmonic generation, high-harmonic generation, wave mixing, nonlinear wavefront control, all-optical switching, topological photonics*

Nonlinear optical effects are naturally weak and arise when intense light beams interact with matter. They cover mainly nonlinear frequency conversion processes, where one or more input frequencies are coherently mixed to produce new frequencies, as well as light-induced refractive index changes, where the complex refractive index of the material at the pump or other wavelengths is modified. In macroscopic media with sufficiently high nonlinear susceptibilities, nonlinear phenomena can become important due to the long interaction lengths, where the phase-matching condition needs to be further satisfied for the frequency conversion effects. In nanoscopic structures, however, characteristic distances can be as small as a fraction of the light wavelengths involved, and therefore, additional strategies to enhance the nonlinear processes in this regime need to be developed. The potential applications of nonlinear optical phenomena on the nanoscale are vast and include ultrasensitive sensing,[1−3] high-resolution optical microscopy,[4−6] holography,[7−9] entangled photon pairs generation,[10] ultrafast all-optical switching,[11,12] integrated optoelectronics,[13] and all-optical computing and communication.[14,15]

Given that the strength of a nonlinear optical effect scales as a power law of the incident light intensity, metallic nanoantennas and metasurfaces have been widely investigated for nonlinear phenomena at subwavelength volumes due to their field-enhancement capabilities.[16−20] Moreover, since they can be designed to manipulate the wavefront of the nonlinear output light,[21] full control over the nonlinear process can be achieved, delivering the desired directionality, phase, and polarization state. However, the mechanisms responsible for these properties rely on the collective oscillation of free electrons (plasmons), leading to ohmic losses and heat generation. This directly restricts the pump power that can be employed without material degradation and, consequently, the nonlinear efficiency that can be attained. In addition, since plasmonic nanostructures confine the fields exclusively to their surfaces, the effective nonlinear interaction volume is minimal, due to the small penetration depths of metals, further reducing the nonlinear performance. To address this issue, nanomaterials with high nonlinear susceptibilities placed in engineered electric field plasmonic hot spots have been investigated, showing significant improvement.[22,23] Nonetheless, the volume

Received: September 6, 2021

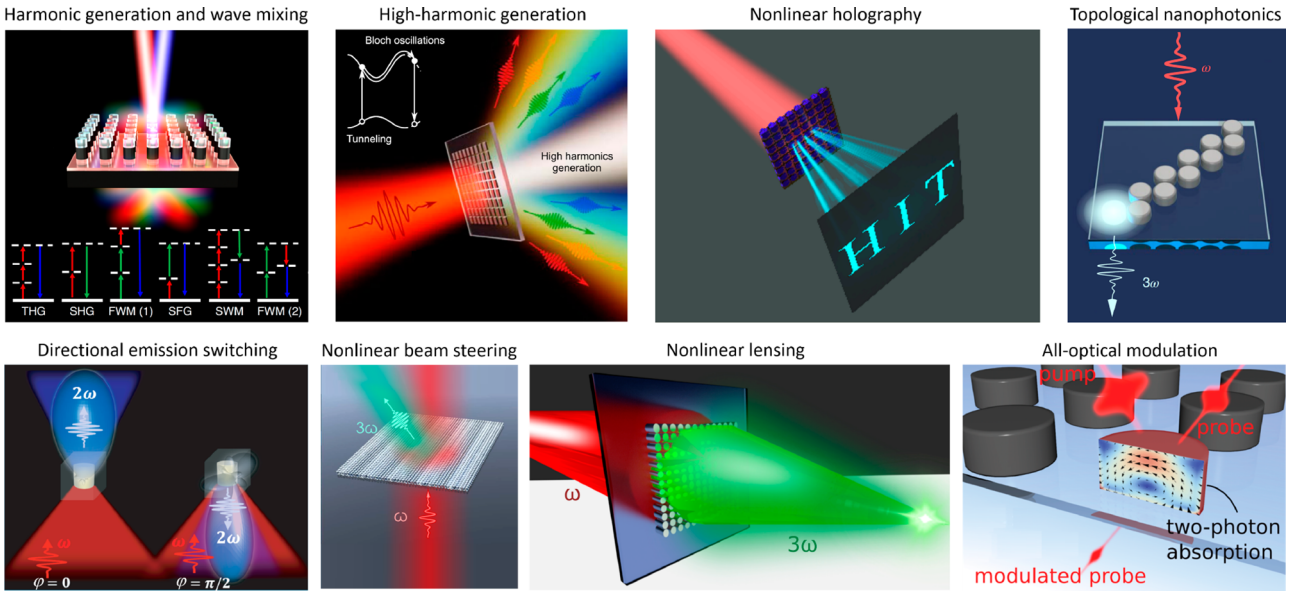

Figure 1. Nonlinear optics with dielectric nanostructures. Schematic depiction of representative nonlinear phenomena examined in this Review. Harmonic generation (SHG and THG) and wave-mixing processes (SFG, FWM, SWM) with two-color pumping. Adapted with permission from ref 29. Copyright 2018 Springer Nature. Forward-to-backward nonlinear emission switching by incident polarization rotation. Adapted with permission from ref 30. Copyright 2020 American Chemical Society. High-harmonic generation (fourth and higher harmonics). Reprinted with permission from ref 31. Copyright 2021 Springer Nature. Wavefront control of the harmonic emission (beam steering,[32] lensing,[33] and holography[7]). Reprinted with permission from ref 32 (Copyright 2018 American Chemical Society), ref 33 (Copyright 2020 American Chemical Society), and ref 7 (Copyright 2018 American Chemical Society). Topologically protected edge states for enhanced harmonic generation. Adapted with permission from ref 34. Copyright 2018 Springer Nature. Ultrafast all-optical modulation through Kerr-type nonlinearities. Adapted with permission from ref 11. Copyright 2015 American Chemical Society.

of excited nonlinear material is still very small compared to the size of the composite nanodevice, highly limiting the overall response.

Less than 10 years ago, nanoantennas and metasurfaces made of high refractive index dielectrics emerged,[24−27] showing several advantages for use in nonlinear nanooptics compared to their plasmonic counterparts. Like nanostructured metals, they have the ability to spectrally selective tailor light scattering and efficiently confine electromagnetic fields below the diffraction limit. However, nanostructured dielectrics support optical resonances driven by nondissipative displacement currents (oscillating bound electrons) whose amplitude increases with the refractive index of the material. In this scenario, negligible losses occur if the energies of the participating wavelengths are smaller than the bandgap energy of the dielectric, enabling the use of high excitation powers. Furthermore, following Miller's rule,[28] a high refractive index entails a large third-order susceptibility and, if the crystal structure is noncentrosymmetric, also a high second-order susceptibility. In addition, different to the case of plasmonics, geometric resonances in dielectrics can confine electromagnetic fields inside the resonator, maximizing the nonlinear interaction volume. All these factors combined place dielectric nanoantennas and metasurfaces as highly promising candidates for efficient nonlinear phenomena with engineered characteristics on the nanometer scale.

In this invited Review I present and examine recent advances in nanostructured dielectrics for nonlinear photonics (see Figure 1). The Review is organized as follows: First, I explore second harmonic generation (SHG) and third harmonic generation (THG). I start by introducing the fundamental properties of the dielectric materials used for manufacturing nonlinear nanoantennas and metasurfaces. I then analyze the influence of resonances of varying nature on the efficiencies of the nonlinear processes, also evaluating directionality and polarization state control of the emitted nonlinear waves based on the geometrical design of the resonators and the symmetry of the underlying crystal structure. I expand the analysis to high harmonic generation (HHG, i.e., fourth harmonic generation and higher harmonics) and also wave mixing effects, including four-wave mixing (FWM), six-wave mixing (SWM), and sum-frequency generation (SFG). Next, I analyze the capability of dielectric resonators to manipulate the wavefront of the radiated nonlinear light, considering reported uses for beam steering, holography, and imaging, among others. I also discuss the nonlinear dynamics of photoexcited processes in the dielectric with a focus on enhanced ultrafast modulation of optical properties. Finally, I briefly introduce the concept of topology in physics and describe recent studies on topologically protected photonic states for harmonic generation in arrays of dielectric nanostructures. To conclude, I present a summary of the main aspects reviewed and outline potential future avenues in the field.

SECOND HARMONIC GENERATION

Second harmonic generation (SHG) is a second-order nonlinear effect that coherently doubles the frequency of the input radiation. It relies on the second order nonlinear susceptibility, $\chi^{(2)}$, which acts as a third-rank tensor when considering the vectorial nature of the fields. In the electric dipole approximation of light−matter interaction, all elements of $\chi^{(2)}$ vanish in uniform media with a centrosymmetric crystal structure, channeling most of the research on SHG in nanostructured dielectrics toward the use of high-index (n > 3) noncentrosymmetric III−V semiconductors, such as GaAs,[30,35−40] AlGaAs,[41−56] and GaP.[57−59] The basic optical

https://doi.org/10.1021/acsphotonics.1c01356
ACS Photonics XXXX, XXX, XXX−XXX

Table 1. Basic Optical Properties of High-Index and Mid-Index Noncentrosymmetric Dielectrics Explored for Nanoscale SHG[a]

material	transparency range (nm)	refractive index	$\lvert\chi^{(2)}_{il}\rvert$ (pm·V^{-1})
GaAs	$\lambda > 870$[78]	3.55–3.36 (870–2000 nm)[78,79]	$\lvert\chi^{(2)}_{36}\rvert$ = 238, 340 (1533 nm, 1064 nm)[80]
$Al_{0.22}Ga_{0.78}As$	$\lambda > 720$[78]	3.60–3.27 (720–2000 nm)[78,81]	$\lvert\chi^{(2)}_{36}\rvert$ = 320 (1064 nm)[82]
GaP	$\lambda > 460$[83]	3.80–3.04 (460–2000 nm)[83,84]	$\lvert\chi^{(2)}_{36}\rvert$ = 74, 142, 318 (1313 nm, 1064 nm, 852 nm)[80]
ZnO	$\lambda > 400$[85]	2.22–1.92 (400–2000 nm)[84,85]	$\lvert\chi^{(2)}_{31}\rvert$ = 1.4 (1064 nm)[86]
			$\lvert\chi^{(2)}_{33}\rvert$ = 14.4 (1064 nm)[86]
α-SiC	$\lambda > 310$[87]	2.9–2.6 (310–2000 nm)[88]	$\lvert\chi^{(2)}_{31}\rvert$ = 4 (1064 nm)[89]
			$\lvert\chi^{(2)}_{33}\rvert$ = 24 (1064 nm)[89]
$BaTiO_3$	$\lambda > 400$[90]	2.6–2.3 (400–2000 nm)[91]	$\lvert\chi^{(2)}_{31}\rvert$ = 28 (1064 nm)[92]
			$\lvert\chi^{(2)}_{33}\rvert$ = 11 (1064 nm)[92]
$LiNbO_3$	$\lambda > 320$[93]	2.8–2.2 (320–2000 nm)[94,95]	$\lvert\chi^{(2)}_{22}\rvert$ = 4.2 (1064 nm)[96]
			$\lvert\chi^{(2)}_{31}\rvert$ = 6.4, 9.2, 9.6 (1313 nm, 1064 nm, 852 nm)[80]
			$\lvert\chi^{(2)}_{33}\rvert$ = 39, 50.4, 51.4 (1313 nm, 1064 nm, 852 nm)[80]

[a]Transparency range, refractive index, and nonzero independent elements of $\chi^{(2)}$ of noncentrosymmetric crystalline dielectrics investigated for resonant SHG on the nanoscale.

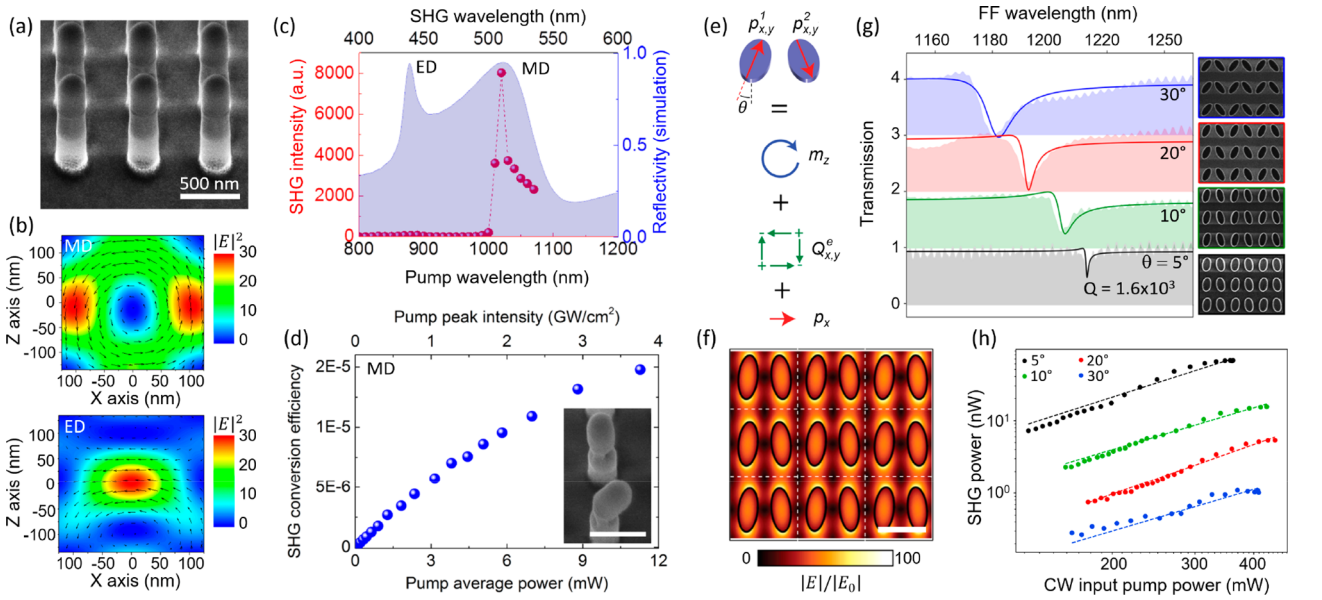

Figure 2. SHG studies on Mie and quasi-BIC resonant dielectric metasurfaces. (a) SEM image of a (100)-GaAs disk metasurface supported by low-index $(Al_xGa_{1-x})_2O_3$ pillars, with the etch mask used for the fabrication as a cap on top. (b) Corresponding numerical simulations of the electric field intensity inside a meta-atom at the magnetic dipole (MD) and electric dipole (ED) modes. (c) Simulated reflectivity spectrum (purple shaded curve) and experimental SH intensity (dots linked by dashed line) of the metasurface, where the optical response at the ED and MD modes can be observed. (d) Measured SHG conversion efficiency at varying pumping power at the MD mode. The inset shows a damaged pillar after illumination at ~8 GW/cm^2. Scale bar, 500 nm. (e) Illustration of the unit cell of a quasi-BIC resonant GaP metasurface, including the modes participating in the formation of the high-Q state. Induced electric dipoles in each particle ($p^1_{x,y}$ and $p^2_{x,y}$) add up to produce an out-of-plane magnetic dipole (m_z) and an in-plane electric quadrupole (Q^e_{xy}), together with an electric dipole pointing in the x-direction (p_x), whose magnitude depends on θ. (f) Simulated electric field distribution of the array for an angle of θ = 5°. Scale bar, 500 nm. (g) Experimental transmission of the metasurface for different angles θ, with corresponding SEM images on the right. (h) Measured CW pump power dependence of the SH signal at different angles θ. (a–d) Adapted with permission from ref 35. Copyright 2016 American Chemical Society. (e–h) Adapted with permission from ref 58. Copyright 2020 American Chemical Society.

properties of these three compounds are presented in Table 1, including their transparency range, refractive index, and nonzero independent elements of $\chi^{(2)}$ in the contracted notation (assuming the Kleinman symmetry condition). All these semiconductors possess a zincblende crystal structure with a cubic symmetry described by the $\bar{4}3m$ point group, making $\chi^{(2)}_{36}$ the only nonzero independent element of $\chi^{(2)}$.[28]

Mid-index ($2 < n < 3$) noncentrosymmetric dielectrics with an extended nonabsorbing window toward the ultraviolet (i.e., with larger bandgap), such as α-SiC (IV–IV family),[60] ZnO (II–IV),[61−63] and perovskites $BaTiO_3$[64−67] and $LiNbO_3$,[68−72] have also been considered in nanoscale SHG studies and are represented in Table 1 as well. ZnO and α-SiC have hexagonal lattices characterized by the $6mm$ point group, while $BaTiO_3$ and $LiNbO_3$ have tetragonal ($4mm$) and trigonal ($3m$) crystal structures, respectively. In agreement with Miller's rule, all these dielectrics exhibit smaller $\chi^{(2)}$ components compared to the higher-index III–V semiconductors.

Although weaker, nanostructures made of centrosymmetric materials also exhibit SHG as the inversion symmetry breaks at interfaces. Polycrystalline Si (poly-Si),[73] amorphous Si (a-Si),[74] a-GaP,[75] and a-Se[76,77] have been studied in this regard.

https://doi.org/10.1021/acsphotonics.1c01356
ACS Photonics XXXX, XXX, XXX−XXX

Table 2. SHG Performance of Several Nanoscale Dielectric Resonators[a]

dielectric material	structure and surrounding	resonant mode	pump wavelength (nm)	pump intensity (GW/cm^2)	η_{SHG} (ξ_{SHG})
GaAs[39]	cylinder nanoantenna embedded in benzocyclobutene	electric and magnetic dipole at FW and high order modes at SH wavelength	1556	1	2.5×10^{-5} (4×10^{-6} W^{-1})
AlGaAs[42]	cylinder nanoantenna embedded in benzocyclobutene	electric and magnetic dipole at FW and high order modes at SH wavelength	1556	10	1.5×10^{-4} * (2×10^{-6} W^{-1})*
GaAs[37]	L-shaped meta-atom metasurface on $(Al_xGa_{1-x})_2O_3$	Fano resonance at FW	990	2.7	6×10^{-6} (1×10^{-6} W^{-1})
AlGaAs[51]	cylinder nanoantenna on SiO_2/ITO/SiO_2	quasi-BIC at FW and high order mode at SH wavelength	1570	0.07	1×10^{-4} * (5×10^{-5} W^{-1})*
GaP[58]	elliptical disk meta-atom metasurface embedded in SiO_2	quasi-BIC at FW	1225	0.01	4×10^{-5} (8×10^{-4} W^{-1})
				1×10^{-6} (CW)	2×10^{-7} (4×10^{-2} W^{-1})
$LiNbO_3$[68]	cube nanoparticle on ITO/fused quartz	electric and magnetic dipole at FW and several multipoles at SH wavelength	720	1.7	5×10^{-7} (1×10^{-7} W^{-1})
ZnO[63]	cylinder meta-atom metasurface on fused quartz	magnetic dipole at FW	394	1.5	7×10^{-9} (9×10^{-9} W^{-1})
				4	1×10^{-8} (saturation region)
a-Si:H[73]	nanosphere on glass	magnetic dipole at FW and high order modes at SH wavelength	1050	30	8×10^{-7} (7×10^{-9} W^{-1})

[a]Experimental values of η_{SHG} and ξ_{SHG} of the most efficient high-index dielectric nanostructures for each reported resonator design and noncentrosymmetric dielectric. Representative cases of nanostructured centrosymmetric crystals and mid-index dielectrics are also included. FW stands for fundamental wavelength. Values followed by a star symbol (*) account for the experimental collection efficiency, as estimated by the authors.

Optical Resonances and Efficiency. In the perturbative regime, the power of the SHG signal (P_{SHG}) increases with the square of the input power (P_{pump}), that is, $P_{SHG} = \xi_{SHG} P_{pump}^2$, where ξ_{SHG} is a nonlinear coefficient that characterizes the strength of the second-order effect. The corresponding conversion efficiency is defined as $\eta_{SHG} = P_{SHG}/P_{pump} = \xi_{SHG} P_{pump}$, growing linearly with P_{pump}, and so $\xi_{SHG} = \eta_{SHG}/P_{pump}$ is also referred to as the normalized conversion efficiency. To enhance ξ_{SHG} and η_{SHG} (at fixed P_{pump}) in resonant nanostructures, a high field confinement inside the resonator at the fundamental wavelength is desired, so that the effective power exciting the nonlinear process is enlarged. In this manner, the nonlinear polarization at frequency 2ω ($\mathcal{P}(2\omega)$), induced by the fundamental local field at ω ($\boldsymbol{E}(\omega)$), $\mathcal{P}(2\omega) = \varepsilon_0 \chi^{(2)} : \mathbf{E}(\omega)\mathbf{E}(\omega)$, will be amplified. To further enhance the second-order effect, the nonlinear coupling between the optical modes supported at the fundamental and second harmonic (SH) wavelengths, as mediated by $\chi^{(2)}$, needs also to be maximized.[97−99] The nonlinear coupling factor can be calculated as the overlap integral between $\mathcal{P}(2\omega)$ and $\boldsymbol{E}(2\omega)$, the electric field distribution describing the mode at 2ω, computed over the nonlinear volume Ω, that is, $\Gamma_{SHG} = \left| \int_\Omega \mathcal{P}(2\omega)\bar{\mathbf{E}}(2\omega)\, d\Omega \right|$, where the norm is taken so that Γ_{SHG} is a positive real number. This quantity, which depends on the magnitude and symmetry of $\chi^{(2)}$ and the nature of the photonic modes involved measures the proclivity of the energy to flow from ω to 2ω. Finally, the scattering cross section at the SH wavelength will dictate the radiation efficiency of the generated light.[100]

To standardize the criteria for the calculation of ξ_{SHG} and η_{SHG} across the different reports taken from the literature, the following method is adopted in this Review. When dealing with single nanoresonators significantly smaller than the excitation spot, P_{pump} will be computed as the doubled amount of power impinging the top surface of the nanoantenna.[51] For structures with circular cross section of radius r, this proportion is simply calculated as $\kappa = 2(1 - e^{-2r^2/w_0^2})$, where w_0 is the spot waist radius (computed as $w_0 = 0.61\lambda/\mathrm{NA}$ if not specified by the authors, where NA is the numerical aperture of the focusing lens). If the resonator is of comparable size to the excitation spot (i.e., $\kappa > 100\%$), then the full power is assumed. For periodic arrays of nanostructures, efficiencies will be calculated as per unit cell to enable direct comparison with single nanoantennas (the total surface area of the unit cell, and not just that of the meta-atom, will be taken into account). When the report uses pulsed excitation, peak powers, as opposed to average powers, will be considered to make quantities independent of laser repetition rate and pulse duration.

Supporting a vast number of optical modes, the geometry of the cylinder has been the most studied shape to enhance SHG in nanoscale dielectrics. By structuring a (100)-GaAs thin film into an array of nanodisks on low-index ($n \sim 1.6$) AlGaO (see scanning electron microscopy, SEM, micrograph of the array in Figure 2a), Liu et al.[35] demonstrated an increase of the SH signal of 4 orders of magnitude when pumping at the magnetic dipole mode (λ_{pump} = 1020 nm). This impressive SHG improvement can be explained by considering that (i) a field enhancement ($|E|/|E_0|$) of up to 5.5 takes place inside the dielectric at the fundamental wavelength (see top image in Figure 2b); (ii) the reference $|E|/|E_0|$ value for the unstructured film is less than 1, given the large Fresnel reflection coefficient at the air/GaAs interface; and (iii) the SH emission intensity is proportional to the fourth power of the fundamental electric field. Compared to the magnetic dipole mode, exciting at the electric dipole mode (λ_{pump} = 890 nm) revealed a nonlinear response that is 2 orders of magnitude lower (see Figure 2c), which can be understood from its reduced mode volume at same field enhancement (Figure 2b) and the increased absorption of GaAs at the corresponding (shorter) SH wavelength. The measured conversion efficiency at the

https://doi.org/10.1021/acsphotonics.1c01356
ACS Photonics XXXX, XXX, XXX−XXX

magnetic dipole was reported to be $\eta_{SHG} \sim 8 \times 10^{-6}$ at a peak pump intensity $I_{pump} = 1.5$ GW/cm^2 (see graph in Figure 2d), with an associated normalized conversion efficiency $\xi_{SHG} = 1.5 \times 10^{-6}$ W^{-1}. These values should be taken as lower bounds as they do not account for the emission collection efficiency, that is, only a portion of the SH radiation was actually collected by the objective lens. The authors also described that increasing I_{pump} above 1.5 GW/cm^2 showed higher η_{SHG}, but with the consequence of irreversible damage of the sample, mainly due to the excitation of free carriers through two-photon-absorption, followed by thermal damage. An alternative to further amplify this nonlinear response has been proposed and experimentally verified by Marino et al.,[56] who showed that a three-layer stacked dielectric metasurface at the magnetic dipole mode can produce up to more than 1 order of magnitude larger conversion efficiency with respect to the single layer case.

Similar SHG studies were performed on individual (110)-GaAs[30] and (111)-GaAs[39] nanodisks embedded in benzocyclobutene ($n \sim 1.5$). Note that no significant variations in efficiency are expected by only changing the crystal orientation,[39] as long as the adequate pump polarization is used. The directionality of the emission, in contrast, will be greatly altered, as discussed later in the text. Obtained SHG efficiencies in those works reached $\xi_{SHG} = 4 \times 10^{-6}$ W^{-1} ($\lambda_{pump} = 1556$ nm) and $\eta_{SHG} = 2.5 \times 10^{-5}$ ($I_{pump} = 1$ GW/cm^2). The large nonlinear responses were attributed in part to the presence of higher order multipoles at the SH wavelengths, though they were damped due to material absorption. This seemingly improved nonlinear performance compared to the (100)-GaAs report presented in Figure 2a−d is primarily a consequence of the relatively low density of disks per unit area in the metasurface (each of them occupying only a seventh of a unit cell), lowering its computed efficiency.

Table 2 summarizes the experimental SHG results of the most efficient dielectric nanostructures for each kind of resonator reported in the literature. For reference, a plasmonic nanoantenna with engineered mode-matching condition yields conversion efficiencies of $\xi_{SHG} = 5.1 \times 10^{-10}$ W^{-1} ($\lambda_{pump} = 1550$ nm) and $\eta_{SHG} = 6.4 \times 10^{-9}$ ($I_{pump} = 0.8$ GW/cm^2).[101] As can be seen from the table, an AlGaAs nanodisk exhibits a similar nonlinear coefficient ξ_{SHG} compared to the described GaAs findings. However, a larger absolute conversion efficiency $\eta_{SHG} \sim 10^{-4}$ could be achieved, given the larger pump intensity utilized, as enabled by the negligible absorption of AlGaAs at the emission wavelength of $\lambda_{SHG} = 778$ nm, and its low two-photon absorption at $\lambda_{pump} = 1556$ nm (relative to that experienced by GaAs at $\lambda_{pump} = 1020$ nm in Figure 2d).[102] It should be stated that a correction factor of ×3 was applied in this case to account for the SH collection efficiency, as estimated by the authors through numerical simulations based on the computed radiation pattern.

Placing the AlGaAs nanodisk on an epsilon-near-zero (ENZ) substrate[103,104] has been proposed and theoretically shown to enhance the nonlinear performance by 2 orders of magnitude. A ENZ material is characterized by a permittivity spectrum with a zero-crossing of the real component, acting as a conductor or an insulator depending on the wavelength. When tuning the SH emission at the ENZ condition, the mode-matching between the fundamental and SH wavelengths enlarges, while the excitation of plasmon polaritons on the ENZ substrate at the fundamental (where it features a metallic behavior) couples with the magnetic dipole mode in the nanodisk, producing increased field confinement inside the dielectric.

The remaining high-index nonlinear dielectric listed in Table 1, GaP, has also been studied experimentally for SHG in the form of Mie-resonant single nanodisks.[57] However, as they were obtained by nanostructuring the surface of a thick GaP wafer, a significantly smaller efficiency was observed (not included in Table 2), given the lack of index contrast between the resonator and the substrate.

Vabishchevich et al.[37] evaluated the more complex design of a GaAs metasurface with broken-symmetry L-shaped meta-atoms supporting a Fano resonance. Fano resonances originate from the interference between broad bright super-radiant and resonant dark subradiant modes, producing high Q-factor asymmetric peaks or dips in the transmittance/reflectance spectrum, accompanied by strong light confinement. In the reported metasurface, the Fano resonance arises from the mixing of transverse (bright) and longitudinal (dark) dipole modes and is characterized by a 2 nm spectral width with a Q factor of about 500. Compared to low-order Mie resonances, this Q factor is more than 1 order of magnitude larger and yields field enhancement ratios inside the dielectric as high as $|E|/|E_0| > 20$. However, given the wide pulse spectrum of the laser beam employed to pump the metasurface (11 nm spectral width), less than 30% of the power coupled to the high-Q resonance, leading to a similar measured nonlinear response compared to the case of the nanodisks (see Table 2 for numerical values).

More recently, resonances originating from bound states in the continuum (BICs) have been studied for nonlinear nanophotonics. BICs are characteristic of all wave phenomena and consist of perfectly confined ("bound") states with eigen-energies embedded in a continuum of extended states, from which they are completely decoupled.[105] A symmetry-protected BIC, for example, occurs when a bound state of a certain symmetry group sits in the continuous spectrum of another symmetry group with forbidden interaction between them due to symmetry constraints. Since BICs are fully localized and entirely detached from radiating channels, they have zero leakage and possess an infinite quality factor. By reciprocity, they cannot be excited by external waves and are, in this sense, invisible. Given that BIC-related fields need to be zero in the surrounding medium, they only exist in structures that are infinitely extended in at least one dimension (an exception occurs for zero or infinite permittivity/permeability materials). For a single particle with finite permittivity and permeability, continuity of the fields at interfaces requires them to be zero everywhere in space if they are to be zero outside the particle, so a BIC cannot form.

In nanophotonics, metasurfaces represent excellent platforms to explore the occurrence of these nonradiative states. However, to make a BIC accessible, a small structural defect or symmetry-breaking perturbation must be added to the system to enable minimum, but appreciable, coupling to the continuum, giving rise to a high-Q quasi-BIC.[106] Moreover, while BICs are forbidden in (realistic) single structures, quasi-BICs are not. In individual resonators, they can arise from the destructive interference in the far field between two modes with similar radiation patterns in the strong coupling regime.[107,108] Their interaction increases the damping rate of one of the modes, while that of the other decreases until it nearly vanishes and the quasi-BIC emerges.

https://doi.org/10.1021/acsphotonics.1c01356
ACS Photonics XXXX, XXX, XXX−XXX

Experimental demonstrations of SHG on the nanoscale through high-Q quasi-BICs have been performed in GaP metasurfaces[58,59] and AlGaAs single nanodisks.[51] Figure 2e schematizes the unit cell of the GaP metasurface studied by Anthur et al.[58] and the optical modes involved in the quasi-BIC formation. The unit cell is composed by a pair of elliptical cylinders tilted in opposite directions at an angle θ with respect to the vertical direction. When $\theta = 0°$, a BIC is sustained due to the in-phase collective oscillation of an out-of-plane magnetic dipole (m_z) and an in-plane electric quadrupole (Q^e_{xy}).[109] When breaking the structural symmetry ($\theta \neq 0°$), the electric dipole component in the x-direction (p_x) becomes finite and opens an input and output leakage radiation channel, turning the state into a quasi-BIC. Because of symmetry restraints, p_x is the only one of the modes that can couple to an incident (x-polarized) plane wave, providing access to the high-Q resonance. Figure 2g shows the measured transmission spectra of the metasurface for varying θ, displaying minima at the quasi-BIC resonances. The quality factor is found to increase with decreasing θ (i.e., when approaching the BIC condition), reaching values close to 2000 at an experimental limit of $\theta = 5°$. Figure 2f presents the corresponding electric field distribution at $\theta = 5°$, revealing $|E|/|E_0|$ ratios as high as >50 inside the dielectric. In this situation, the metasurface was evaluated for SHG using both pulsed and continuous-wave (CW) illumination, resulting in record-breaking $\xi_{SHG} = 4 \times 10^{-2}$ W^{-1} for CW excitation (vs 8×10^{-4} W^{-1} for pulsed pumping), where no incident power is cut by the narrow width of the quasi-BIC resonance (<1 nm full width at half-maximum, fwhm). Compared to reports based on Mie and Fano resonances, this performance is substantially superior (refer to Table 2 for detailed information). The authors state that because of experimental limitations, power intensities larger than 1 kW/cm^2 could not be used to purse η_{SHG} values higher than $\sim 2 \times 10^{-7}$ (see Figure 2h for pump power dependence SHG curves at different θ).

A theoretical work engineering a quasi-BIC in an array of AlGaAs disks with noncentered slots as the symmetry-breaking defect, demonstrated a quality factor close to 10^4 and $|E|/|E_0|$ factors near 200 inside the dielectric, leading to SHG efficiencies as high as 10% at only 5 MW/cm^{-2} ($\xi_{SHG} = 2.5$ W^{-1}).[110] A similar response has been predicted by Moretti et al.[111] for an array as that in Figure 2f, but taller (200 nm height instead of 150 nm), supporting a quasi-BIC characterized by in-plane magnetic dipole and out-of-plane electric quadrupole contributions. However, it has also been suggested that due to nonlinear refraction and multiple photon absorption appreciably affecting the high-Q resonant condition at >0.01 MW/cm^{-2}, the ultimate maximum nonlinear efficiency would not exceed 0.1%.[112]

Enhanced SHG through a quasi-BIC resonance was also demonstrated in a single AlGaAs cylindrical resonator on a SiO_2/indium tin oxide (ITO)/SiO_2 substrate[51] (see schematic of the experiment in Figure 3a and SEM image of the sample in the inset of Figure 3b). ITO features a ENZ condition around 1200 nm, acting as a conductor (insulator) above (below) this wavelength (Figure 3c). The mirror-like property of the ITO layer was used to control the interference between magnetic dipolar modes in the strong coupling regime (Figure 3b) to produce a quasi-BIC at 1570 nm. At the corresponding SH wavelength, ITO behaves like glass, enabling collection of the radiated light both in the forward and backward directions. To maximize the coupling of the pump beam to the quasi-BIC,

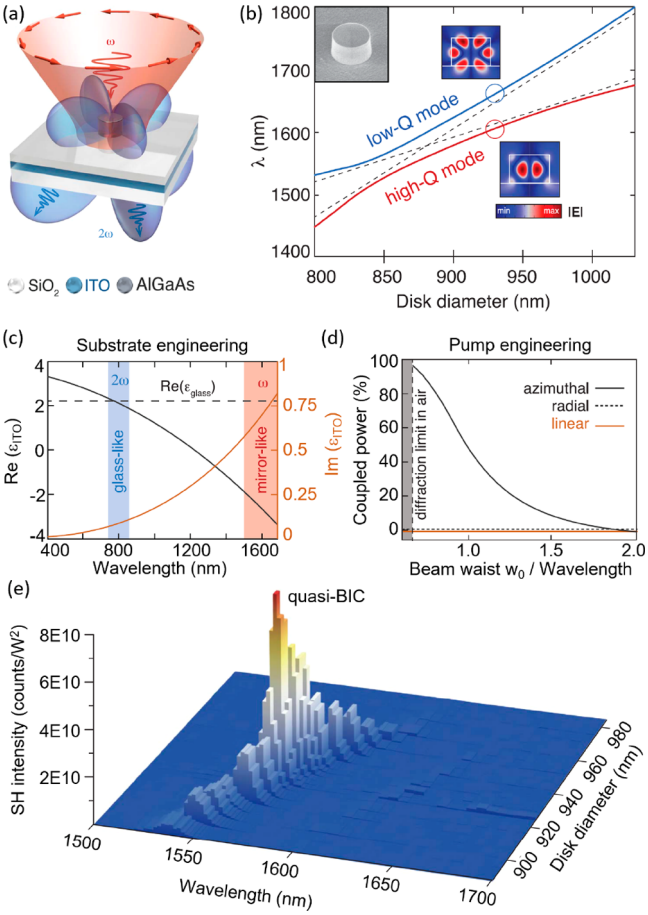

Figure 3. SHG from a quasi-BIC resonant single nanostructure. (a) Illustration of a AlGaAs nanodisk on a SiO_2/ITO/SiO_2 substrate excited with azimuthally polarized light. (b) Simulated mode wavelength vs disk diameter for the two modes involved in the quasi-BIC formation. Their near-field patterns in the hybrid regime are included as insets. The top-left inset shows the SEM image of a fabricated resonator of 930 nm diameter. (c) Experimental real and imaginary parts of the permittivity of ITO. The mirror-like and glass-like regions of interest are highlighted. (d) Calculated proportion of pump power coupled to the quasi-BIC resonance for varying spot size at different polarization states. (e) Measured SH intensity as a function of resonator diameter and excitation wavelength when pumping with azimuthally polarized light. Adapted with permission from ref 51. Copyright 2020 The American Association for the Advancement of Science.

azimuthally polarized incident light was used to better match the field profile of the excited hybrid mode (Figure 3d). An experimental Q-factor close to 200 was obtained, highly amplifying the SH signal, further boosted by a high-order Mie mode at the SH wavelength with a Q-factor of ~65 (see nonlinear measurement in Figure 3e). The SHG process produced a conversion efficiency $\eta_{SHG} = 1 \times 10^{-4}$ at $I_{pump} = 0.07$ GW/cm^2 (pulsed illumination), measured just below the laser damage threshold, representing a significant improvement compared to standard Mie single nanoantennas. A picosecond pulsed laser (~3 nm line width) was used in this case to effectively pump the ~8 nm fwhm mode. To further increase the quality factor to the 500−1200 range in compact resonators, different composite nanostructures were theoretically proposed. Volkovskaya et al.[108] modeled a AlGaAs disk enclosed by four Au rods on the sides that acted as two pairs of

https://doi.org/10.1021/acsphotonics.1c01356
ACS Photonics XXXX, XXX, XXX−XXX

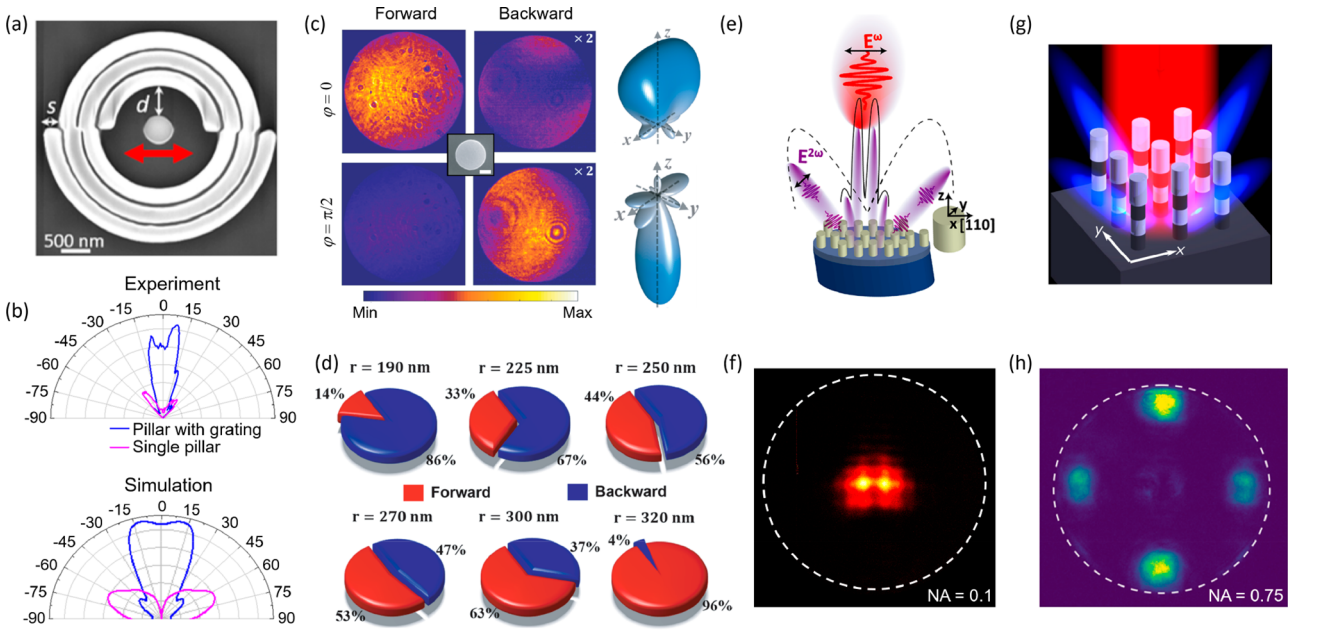

Figure 4. Directionality control of the SH emission of nanoantennas and metasurfaces. (a) SEM image of a (100)-AlGaAs nanodisk placed in the center of an asymmetric grating of the same material, designed to redirect the intrinsic lateral SH emission of the bare nanodisk toward the normal direction. (b) Experimental and simulated nonlinear radiation diagrams of the pillar with and without the grating. (c) Left: Experimental two-dimensional projections of the SH radiation distribution of a single (110)-GaAs nanodisk in the forward and backward directions for two orthogonal pump polarizations. Scale bar of SEM micrograph, 200 nm. Right: Corresponding simulated three-dimensional nonlinear radiation diagrams. (d) Experimentally determined proportions of the SH emission radiated in the forward and backward directions for different disk radii (r) at fixed pump polarization. (e–h) (100)-AlGaAs (e, f) and (100)-GaAs (g, h) disk metasurfaces designed to emit SH light preferentially in the zero or first diffraction orders, correspondingly. In (e), solid and dashed lines represent SH radiation lobes of the metasurface and a single meta-atom, respectively. In (f) and (h), the dashed lines indicate the numerical aperture (NA) of SH collection. (a, b) Adapted with permission from ref 53. Copyright 2018 American Chemical Society. (c, d) Adapted with permission from ref 30. Copyright 2020 American Chemical Society. (e, f) Reprinted with permission from ref 54. Copyright 2019 American Chemical Society. (g, h) Reprinted with permission from ref 36. Copyright 2018 American Chemical Society.

parallel mirrors to mimic an infinite lattice of disks, while Gandhi et al.[113] studied a core/shell AlGaAs nanowire with the shell supporting enhanced losses with respect to the core to sustain a quasi-BIC.

Mid-index ($2 < n < 3$) dielectric resonators explored for SHG present smaller refractive index and second-order nonlinear susceptibility compared to GaAs, AlGaAs, or GaP (see Table 1), but have the advantage of an extended transparency range toward higher frequencies, enabling SHG at near-ultraviolet wavelengths. Mie-resonant ZnO, $BaTiO_3$, and $LiNbO_3$ single nanoparticles or metasurfaces with characteristic sizes about 200–300 nm have demonstrated enhanced SHG in the ∼200–450 nm emission wavelength range, with conversion efficiencies up to $\xi_{SHG} = 1 \times 10^{-7}$ W^{-1} and $\eta_{SHG} = 5 \times 10^{-7}$ ($I_{pump} = 1.7$ GW/cm^2).[63,64,66,68,72] Improved performances were observed in $LiNbO_3$ metasurfaces,[69,70] which have shown $\eta_{SHG} \sim 10^{-6}$ at similar peak pump intensities, although such reports did not explore the ultraviolet emission range. Moreover, irregular nanoparticles made of α-SiC yielded conversion efficiencies around 10^{-5}.[60] However, no control over the nanoparticle shape could be attained, and given that spherical-like α-SiC nanoparticles showed $\eta_{SHG} \sim 10^{-7}$, the further enhancement was attributed to surface nonlinearities. It is worth mentioning that a direct comparison of AlGaAs and $BaTiO_3$ nanospheres in air was numerically investigated to evaluate differences in the conversion efficiency in the same conditions. At 1 GW/cm^2, obtained η_{SHG} values were 5×10^{-4} and 1×10^{-5}, when exciting at the magnetic dipole mode ($\lambda_{pump} = 1050$ nm), with emission at high order modes.[114] Larger efficiencies for nanostructured $LiNbO_3$ have been theoretically predicted for Fano[115] and quasi-BIC[116] resonant metasurfaces, where the latter report used the meta-atom design featured in Figure 2e (with $\theta = 8°$), resulting in $\eta_{SHG} = 2 \times 10^{-3}$ at 0.33 MW/cm^2 ($\lambda_{pump} \sim 800$ nm).

SHG studies have also been carried out in centrosymmetric high-index and mid-index dielectric nanostructures, where second-order nonlinearities arise only from surface effects and volume magnetic dipole and electric quadrupole contributions (the electric dipole term vanishes, while higher orders can be neglected). Among them, surface SHG is expected to be the dominant component, following numerical studies on Si nanoantennas.[117] In this scenario, a-Se nanoparticles and metasurfaces[76,77] have shown experimental SH conversion efficiencies up to 10^{-6}, while a similar nonlinear response was measured for single poly-Si nanoparticles,[73] where the inversion symmetry is broken at the many interfaces between the inner grains.

Polarization and Directionality. The polarization, intensity, and spatial distribution of the SH emission depend strongly on the polarization nature and incidence angle of the fundamental beam, as well as on the geometry and crystal symmetry of the excited structure. This complex relationship between several factors can be used not only to control the directionality[30,36,38,39,52–54,71,118–120] and polarization state[49] of the SH radiation, but also to characterize different properties of the resonator,[50] the excitation light,[52] and the nonlinear process itself.[35,45] For example, polarization studies in the

https://doi.org/10.1021/acsphotonics.1c01356
ACS Photonics XXXX, XXX, XXX–XXX

GaAs nanodisk metasurface presented in Figure 2a−d were used to determine whether the nonlinear emission originated only from the bulk, or if the influence of the surface was also significant.[35] The authors observed a relative orientation of the polarization of the emitted light with respect to that of the pump, which could not be explained by considering pure volume nonlinearity, but could be qualitatively described instead through the coherent interference between bulk and surface nonlinear emissions. In contrast, other studies have found that modeling the SHG with bulk nonlinearity only was sufficient to reproduce the experimental results.[43,44,46] However, different to the case of the GaAs metasurface, which used λ_{pump} = 1020 nm, such other investigations were performed in the nonabsorbing region of the dielectric for both pump and SH wavelengths (λ_{pump} > 1500 nm), which could have masked surface contributions as no losses limited the extraction of the nonlinear light generated in the volume.

Analyzing the structure of the SH polarization in high-index nanoantennas has also been used to determine the relative contribution of nonlinear responses of electric and magnetic character. Kruk et al.[45] observed that a single (100)-AlGaAs disk pumped with linearly polarized light at a superposition of electric and magnetic dipole modes resulted in SH emission with a rather complex polarization structure, including radial-like and azimuthal-like polarization distributions, as measured from back-focal plane images. These polarization patterns were theoretically shown to arise from the electric (radial) and magnetic (azimuthal) multipoles composing the SH radiation. The authors further found that electric (magnetic) modes dominated the emission when the input polarization was set at 45° (0°) with respect to the [100] crystal direction. The continuous transition between electric and magnetic nonlinearities could then be characterized by simply tuning the polarization of the pump beam and observing the polarization state of the SH radiation.

One of the main aspects to consider in nonlinear conversion processes at the nanoscale beyond efficiency is the directionality of the emission. The most studied condition of the (100) zinc-blend III−V nanodisk excited at the magnetic dipole mode with normal incidence shows preferential backward radiation with a doughnut-shaped pattern and no signal in the vertical direction. This low SH directivity is a consequence of the particular symmetry of the second-order susceptibility tensor, which induces a phase shift between the nonlinear currents generated in opposite halves of the cylinder, leading to destructive interference in the far-field along the normal direction.[120] When tilting the incidence angle by 45°, however, the generated SH fields can radiate along the vertical axis, increasing the collected nonlinear signal through a finite numerical aperture by 1 order of magnitude.[52,118] It has been theoretically proposed that vertical SH emission can also be achieved at normal incidence by adding a bar next to the cylinder.[119] The broad electric dipole resonance supported by the bar can control the magnetic dipole excitation of the cylinder, producing a field distribution inside that is equivalent to that of the isolated disk at 45° tilted incidence. Alternatively, introducing a height difference between two halves of the nanodisk can also break the field symmetry inside the dielectric, leading to SH nonlinear currents radiating in the vertical direction,[120] as has been experimentally demonstrated (refer to Figure 9a).[121]

Ghirardini et al.[53] tested a different strategy by studying the response of a (100)-AlGaAs nanodisk surrounded by an asymmetric grating of the same material to control the SH directionality (see SEM image of the composite structure in Figure 4a). The grating was added to redirect the lateral lobes of the intrinsic SH emission of the central cylinder to the normal direction. The asymmetric character of the grating, determined by the displacement distance s highlighted in Figure 4a, was needed to generate a phase shift between the SH signals emitted on each halve of the nanodisk, converting the quadrupolar-like SH emission profile of the bare cylinder into a dipolar-like radiation pattern. In this manner, the collection efficiency within a 0.2 numerical aperture was increased with respect to the isolated pillar by 2 orders of magnitude, as can be seen in the radiation diagrams shown in Figure 4b.

As the second-order susceptibility tensor becomes reoriented under crystal rotation, the directionality of the nonlinear emission can also be manipulated by choosing different crystal cuts of the dielectric material. The differences in the emission patterns of (100)-GaAs, (110)-GaAs, and (111)-GaAs single nanodisks embedded in benzocyclobutene were recently studied in detail,[30,39] in terms of the interference between the generated nonlinear multipoles, when pumping at a mixture of magnetic and electric dipole modes at normal incidence. Attaining unidirectional enhanced forward emission requires in-phase forward radiating multipoles with simultaneous out-of-phase backward scattering, that is, interfering multipoles of opposite parity, with respect to vertical reflection symmetry, and balanced weight (in terms of backward radiation). Having all components of the same parity would enhance the backward emission. Also important are the intervening azimuthal indices m within each polar order l (dipole, quadrupole, etc.), which determine whether there will be radiation along the optical axis or not. (100)-GaAs nanoantennas produce SH multipoles with only even values of m (0, ±2), resulting in no SH emission in the normal direction, as previously discussed, while nonlinear currents in (111)-GaAs nanoantennas also create multipoles with odd m values (±1, ±3, ±5), carrying nonzero vertical radiation. The symmetry of the (111) crystal, however, limits the possibility of tuning interference conditions for further directivity control, as the nonlinear multipolar composition is preserved under pump polarization rotation, although the relative weight of the different m excited within each l can be altered. For (110)-GaAs, in contrast, only SH multipoles with odd m values are present, and their relative contribution (for both azimuthal and polar orders) can be modified by simply rotating the pump polarization. In this way, unidirectional emission was experimentally demonstrated in individual (110)-GaAs nanoantennas, with the possibility to switch from forward to backward emission by just rotating the input polarization by 90° (see schematic illustration in Figure 1). Figure 4c shows the measured back-focal plane SH images in the forward and backward directions for two orthogonal incident polarizations, together with the simulated radiation diagrams. The obtained experimental forward-to-backward ratios ran from 0.16 ($\varphi = \pi/2$) to >45 ($\varphi = 0$), accompanied by only a small change in conversion efficiency. The forward-to-backward ratio could also be modified by changing the disk radius (r) at fixed pump polarization, as is exhibited in Figure 4d.

Saerens et al.[38] characterized the SHG properties of nanoantennas made of wurtzite-structure GaAs, as opposed to zinc-blend GaAs, where the resonators were defined by using a focused ion beam to slice bottom-up grown GaAs

https://doi.org/10.1021/acsphotonics.1c01356
ACS Photonics XXXX, XXX, XXX−XXX

Table 3. Basic Optical Properties of High-Index and Mid-Index Dielectrics Explored for Nanoscale THG[a]

material	transparency range (nm)	refractive index	$\chi^{(3)}$ ($nm^2 \cdot V^{-2}$)
Si	$\lambda > 700$[141]	3.77–3.45 (700–2000 nm)[141,143]	$\chi^{(3)}_{1111} = 0.25$ (1550 nm)[144]
a-Si	$\lambda > 930$[142]	3.71–3.44 (930–2000 nm)[142]	$\chi^{(3)}_{1111} = 0.6$ (1550 nm)[145] [a-Si:H]
Ge	$\lambda > 1090$[146]	4.33–4.04 (1090–2000 nm)[146]	$\chi^{(3)}_{1111} = 0.4$ (2000 nm)[144]
a-Ge	$\lambda > 1300$[147]	4.67–4.35 (1300–2000 nm)[147]	$\chi^{(3)}_{1111} = 0.57$ (1650 nm)[137]
$Al_{0.22}Ga_{0.78}As$	$\lambda > 720$[78]	3.60–3.27 (720–2000 nm)[78,81]	$\chi^{(3)}_{eff} = 0.07$ (1554 nm)[148]
ZnO	$\lambda > 400$[85]	2.22–1.92 (400–2000 nm)[84,85]	$\chi^{(3)}_{1111} = 0.03$ (1500 nm)[149]
TiO_2 (thin film)	$\lambda > 370$[150]	2.84–2.26 (370–2000 nm)[150,151]	$\chi^{(3)}_{1111} = 0.02$ (1550 nm)[152]

[a]Transparency range, refractive index, and primary component or effective value of $\chi^{(3)}$ of crystalline and amorphous dielectrics investigated for resonant THG on the nanoscale.

Table 4. THG Performance of Several Nanoscale Dielectric Resonators[a]

dielectric material	structure and surrounding	resonant mode	pump wavelength (nm)	pump intensity (GW/cm^2)	η_{THG} (ξ_{THG})
Si[24]	cylinder meta-atom metasurface on glass	magnetic dipole at FW	1260	4.5	8×10^{-8} (1×10^{-10} W^{-2})
poly-Si[123]	cylinder-bar unit cell metasurface on glass	Fano resonance at FW	1350	1.1	1.2×10^{-6} (3×10^{-8} W^{-2})
a-Ge[138]	cylinder nanoantenna on glass	high order anapole excitation at FW	1650	0.8	5×10^{-6} (5×10^{-9} W^{-2})
				2.0	1×10^{-5} (saturation region)
a-Si[136]	cylinder on Au surface	anapole excitation at FW	1550	1.8	5×10^{-5}* (3×10^{-8} W^{-2})*
Si[106]	T-shape meta-atom metasurface on quartz	Q-BIC resonance at FW	1587	0.06	9×10^{-7} (1×10^{-5} W^{-2})
TiO_2[153]	cylinder meta-atom metasurface on glass	anapole excitation at FW	555	3.8	5×10^{-8} (3×10^{-9} W^{-2})
				9	2×10^{-7} (saturation region)

[a]Experimental values of η_{THG} and ξ_{THG} of the most efficient high-index and mix-index dielectric nanostructures for each reported resonator design and dielectric material. FW stands for fundamental wavelength. Values followed by a star symbol (*) account for the experimental collection efficiency, as estimated by the authors.

nanowires with a wurtzite crystal lattice. Due to the particular crystal symmetry, such nanoantennas provided SH emission mainly along the vertical axis. In addition, by forming phase arrays of two nanoparticles, the SH radiation could be further squeezed in the same direction (symmetric dimer) or even redirected up to 30° (asymmetric dimer) with respect to the optical axis, due to the generated interferences.

Unlike nanoantennas, periodic metasurfaces behave like gratings at the SH wavelength, channeling the emission into the different diffraction orders. As governed by the ratio between wavelength and lattice period, only a few of the lowest diffraction orders can propagate, with the proportion of power going into each of them depending on the nature of the excited modes. In the simplest approximation, when the period is large enough, the metasurface lattice acts as a modulation factor over the multipolar radiation structure of the individual meta-atoms, as determined by their shape and crystal symmetry.[54,120] The response of the metasurface can then be estimated as the product between the far-field emission pattern of a single unit cell and an array coefficient which contains only the diffraction information. With this concept, nanodisk periodic metasurfaces have been engineered to direct most of the light to the zero[54] (Figure 4e,f) or first[36,71] (Figure 4g,h) diffraction orders. A more sophisticated approach to manipulate the propagation of the generated SH beam consists of metasurfaces with engineered phase gradients, as discussed later on in this Review.

THIRD HARMONIC GENERATION

Third harmonic generation (THG) is a third-order nonlinear process that coherently converts photons of frequency ω into photons of frequency 3ω. The corresponding third-order nonlinear polarization at 3ω induced by the fundamental field at ω is $\mathcal{P}(3\omega) = \varepsilon_0 \chi^{(3)} : \mathbf{E}(\omega)\mathbf{E}(\omega)\mathbf{E}(\omega)$, where the third order-susceptibility $\chi^{(3)}$ is a fourth-rank tensor. As the strength of this effect increases with the third power of the intensity of the incident radiation, it can be largely enhanced in nanoscale resonators showing high-field confinement. Also, same as with SHG, maximizing the nonlinear coupling between the modes supported at the fundamental and third harmonic (TH) wavelengths can further amplify the nonlinear process.[97] The third-order nonlinear coupling factor can be computed as the overlap integral in the nonlinear volume Ω between $\mathcal{P}(3\omega)$ and the electric field distribution $\boldsymbol{E}(3\omega)$ characterizing the mode at 3ω, that is, $\Gamma_{THG} = \left| \int_\Omega \mathcal{P}(3\omega)\bar{\mathbf{E}}(3\omega)\, d\Omega \right|$, where the norm is taken so that Γ_{THG} is a positive definite quantity.

Unlike second-order effects, third-order nonlinearities are not nulled in centrosymmetric environments, making both crystalline and amorphous media of equal interest to study THG. Explored high-index and mid-index dielectric materials for THG at subwavelength volumes include Si,[24,122−136] Ge,[137,138] AlGaAs,[50] TiO_2,[139] and ZnO,[61] whose basic optical properties are summarized in Table 3. For cubic crystals belonging to the $\bar{4}3m$ point group, such as the first three materials listed, there are two independent elements of $\chi^{(3)}$ for the THG process, while for their amorphous (isotropic) versions, there is only one.[28] Moreover, as the anisotropy in

https://doi.org/10.1021/acsphotonics.1c01356
ACS Photonics XXXX, XXX, XXX−XXX

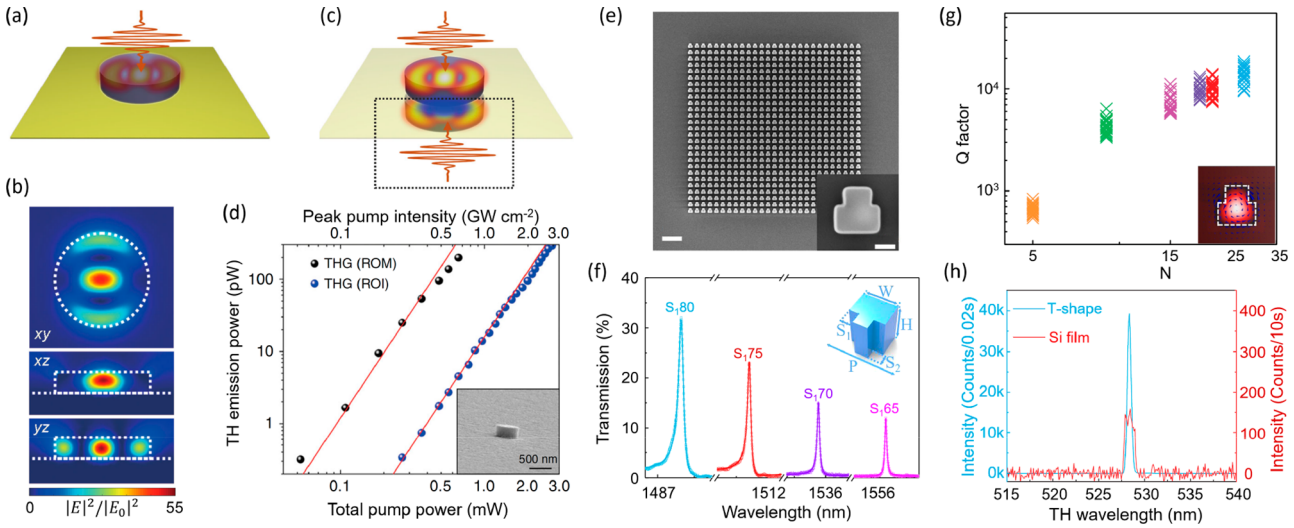

Figure 5. THG studies on anapole and quasi-BIC resonant dielectric nanostructures. (a, b) Illustration of a Si disk on Au excited at the anapole state (a), with associated field intensity pattern in (b). (c) Representation of the mirror image of the excited nanodisk generated by the Au film, which coherently enhances the nonlinear response. (d) Measured power dependence of the THG signal for the resonator-on-metal (ROM) and resonator-on-insulator (ROI) configurations. (e) SEM micrograph of a T-shape Si meta-atom metasurface supporting a quasi-BIC resonance. Scale bars, 2 μm (main image) and 200 nm (inset). (f) Transmission measurement of the metasurface for different sizes of the defect parameter S_1 (displayed in nm; see schematic of the meta-atom in the inset), with S_2 = 160 nm. (g) Experimental values of the resonance quality factor when varying the number of elements in the $N \times N$ array. The inset displays the electromagnetic field distribution for $N \to \infty$, where the color code indicates the amplitude of the magnetic field and the arrows represent the vectorial character of the in-plane electric field. (h) THG signal of the metasurface with N = 9 excited at resonance. The response of the unstructured Si film is included for reference. (a–d) Adapted with permission from ref 136. Copyright 2018 Springer Nature. (e–h) Adapted with permission from ref 106. Copyright 2019 American Physical Society.

$\chi^{(3)}$ is relatively low in many ordered crystals, assuming isotropic conditions usually represents a good approximation.[140] In Table 3, only the primary component or effective value of $\chi^{(3)}$ is quoted in each case.

In the following, the absolute and normalized THG conversion efficiencies will be calculated as $\eta_{THG} = P_{THG}/P_{pump}$ and $\xi_{THG} = P_{THG}/P_{pump}^3$, respectively. The same considerations as those described for SHG will be applied to evaluate the nonlinear parameters (i.e., for small single resonators P_{pump} will be computed as the doubled fraction of input power hitting the top geometric area of the nanoantenna, while for metasurfaces, all quantities will be calculated as per unit cell).

Optical Resonances and Efficiency. The first report on nonlinear frequency conversion on dielectric nanoantennas or metasurfaces was published by Shcherbakov et al.[24] in 2014 through the study of THG in an array of Si nanodisks on SiO_2. Pumping the metasurface at the magnetic dipole mode showed a maximum field enhancement inside the dielectric $|E|/|E_0| \sim 5$, producing a TH signal a factor of 4 higher than the electric dipole mode and 2 orders of magnitude larger with respect to the bulk. After this report, which showed $\xi_{THG} = 1 \times 10^{-10}$ W^{-2} (λ_{pump} = 1260 nm) and a maximum absolute efficiency close to $\eta_{THG} = 1 \times 10^{-7}$ (I_{pump} = 4.5 GW/cm^2), many demonstrations on different structures followed, some of which are described in Table 4.

One year later, a better THG performance was achieved by Y. Yang et al.[123] in a Si metasurface featuring a Fano-resonance with a Q-factor of 466 (~3 nm spectral width), which demonstrated an enhancement of 5 orders of magnitude with respect to the unpatterned film. The meta-atom was composed by a cylinder coupled to a rectangular bar, both made from poly-Si (same design as that in Figure 7a). When pumped by normal incident light, the bar supports an electric dipole mode which excites an out-of-plane magnetic dipole in the disk that otherwise remains dark, leading to a Fano resonance with $|E|/|E_0|$ values as high as 45 inside the dielectric cylinder. The measured THG nonlinear efficiencies were $\xi_{THG} = 3 \times 10^{-8}$ W^{-2} (λ_{pump} = 1350 nm) and $\eta_{THG} = 1.2 \times 10^{-6}$ (I_{pump} = 1.1 GW/cm^2). However, given that the line width of the pulsed laser employed was 5× that of the Fano resonance, the excitation process was highly restricted and prevented the system from producing an optimized response. A comparable conversion efficiency was reported on quadrumers of hydrogenated a-Si (a-Si:H) disks excited at oblique incidence,[124] when pumping at a Fano resonance generated by the interference between individual and collective magnetic modes. In this case, a relatively wide Fano resonance was excited (spectral width >20 nm) and no coupling issues with the fundamental beam arose.

THG has also been studied in single a-Ge nanodisks at first- and second-order anapole states.[137,138] Anapole excitations are characterized by a minimum in the scattering cross section and a high field confinement inside the resonator. The nonradiative character of the fundamental anapole develops from the destructive interference in the far field between the radiation patterns of Cartesian electric and toroidal dipoles excited in the structure.[154] The second-order anapole state can be understood in terms of a hybridization between the first-order anapole and a Fabry–Perot resonance.[155,156] The higher-order condition demonstrated a THG enhancement of 4 orders of magnitude with respect to the bulk, outperforming by more than 1 order of magnitude the fundamental anapole excitation, due to the further enhanced field confinement at the second-order state. A saturation behavior of the conversion efficiency was observed at pump intensities higher than 0.8 GW/cm^2 (without reaching the damage threshold), attributed to nonlinearly induced changes in the refractive index, driving

https://doi.org/10.1021/acsphotonics.1c01356
ACS Photonics XXXX, XXX, XXX–XXX

the structure off-resonance, and a maximum η_{THG} of 1×10^{-5} was measured at 2.0 GW/cm^2. A mid-index TiO_2 nanodisk meta-atom metasurface was also explored at the anapole state for THG,[153] but analyzing its performance at λ_{pump} = 555 nm for emission at ultraviolet wavelengths, exploiting TiO_2 low transparency onset (see Table 3). Compared to the reference unstructured film, an enhancement of more than 2 orders of magnitude was observed. However, the obtained η_{THG} value from the metasurface did not surpass the order of 10^{-7} even at I_{pump} > 10 GW/cm^2, given the relatively low intrinsic response from this dielectric.

Larger THG efficiencies have been reported in hybrid dielectric/metal antennas supporting an enhanced fundamental anapole excitation.[135,136] Two such kind of systems were experimentally analyzed, both utilizing a Si disk as the dielectric component, with the metal (Au) entering as a ring surrounding the dielectric in one case,[135] or as the surface over which the disk rested in the other.[136] The latter structure is illustrated in Figure 5a, with the corresponding calculated field intensity distribution displayed in Figure 5b. Compared to the situation of the dielectric disk on glass, the addition of the metal boosts the excitation of both electric and toroidal dipole moments producing the anapole condition, increasing the field intensity inside the dielectric by a factor of 8. Moreover, the metal forms a mirror image of the nonlinear source (the disk), as schematized in Figure 5c, further amplifying the nonlinear signal. As can be observed in Figure 5d, these effects lead to an enhancement of the THG emission of 2 orders of magnitude with respect to the anapole in the disk-on-insulator configuration, delivering $\eta_{THG} = 5 \times 10^{-5}$ at I_{pump} = 1.8 GW/cm^2. Yin et al.[157] later calculated theoretically that adding an additional metallic component to this system (a Au ring on top of the Si disk) could additionally amplify the THG efficiency by 1 order of magnitude.

Metasurfaces excited at quasi-BIC resonances have demonstrated the highest normalized conversion efficiencies for THG.[106,158,159] Figure 5e–h summarizes the main results from the investigation performed by Liu et al.,[106] who studied a metasurface composed by T-shape meta-atoms (SEM image in Figure 5e). The associated BIC, with an out-of-plane magnetic dipole nature, occurs for the meta-atom with a square cross section (i.e., $S_{1,2} = 0$ in the diagram included in Figure 5f), while making $S_{1,2} \neq 0$ breaks the symmetry of the system turning the BIC into a quasi-BIC. Figure 5f exhibits the transmission spectra for metasurfaces with varying S_1 at fixed S_2, where a narrowing of the resonance (and a reduction in transmission) is observed as S_1 decreases. The Q-factor is also found to increase when extending the number N^2 of cells in the $N \times N$ array, as shown in Figure 5g. For the largest N (N = 27), a quality factor as large as $\sim 2 \times 10^4$ was attained (<0.1 nm line width), whose origin was found to be almost purely radiative, as the nonradiative Q-factor, covering surface roughness and other imperfections, was estimated at the order of 10^5 (i.e., $1/Q = 1/Q_{nr} + 1/Q_r \approx 1/Q_r$, where Q_r and Q_{nr} are the radiative and nonradiative quality factors, respectively). A metasurface with N = 9 ($Q \sim 4 \times 10^3$) was selected for the THG experiments, where the low N number was chosen to match the spectral width of the resonance with that of the pulsed laser beam. A normalized efficiency as high as $\xi_{THG} = 1 \times 10^{-5}$ W^{-2} was demonstrated, with an associated enhancement of more than 5 orders of magnitude with respect to the unpatterned Si film, as can be deduced from Figure 5h.

Koshelev et al.[158] studied the effect of the critical coupling condition on the THG efficiency in quasi-BIC resonant metasurfaces. This condition maximizes the coupling of the incoming wave to the resonator and is fulfilled when radiative losses equal their nonradiative counterpart ($Q_r = Q_{nr}$). Figure 6a shows the investigated a-Si:H periodic array, where the unit cell is composed by a pair of parallel rectangular bars of the same length and different widths w and $w - \delta w$. The high-Q resonance supported by the structure arises from the interaction between oppositely directed magnetic dipoles with slightly different amplitudes, as is evidenced by the

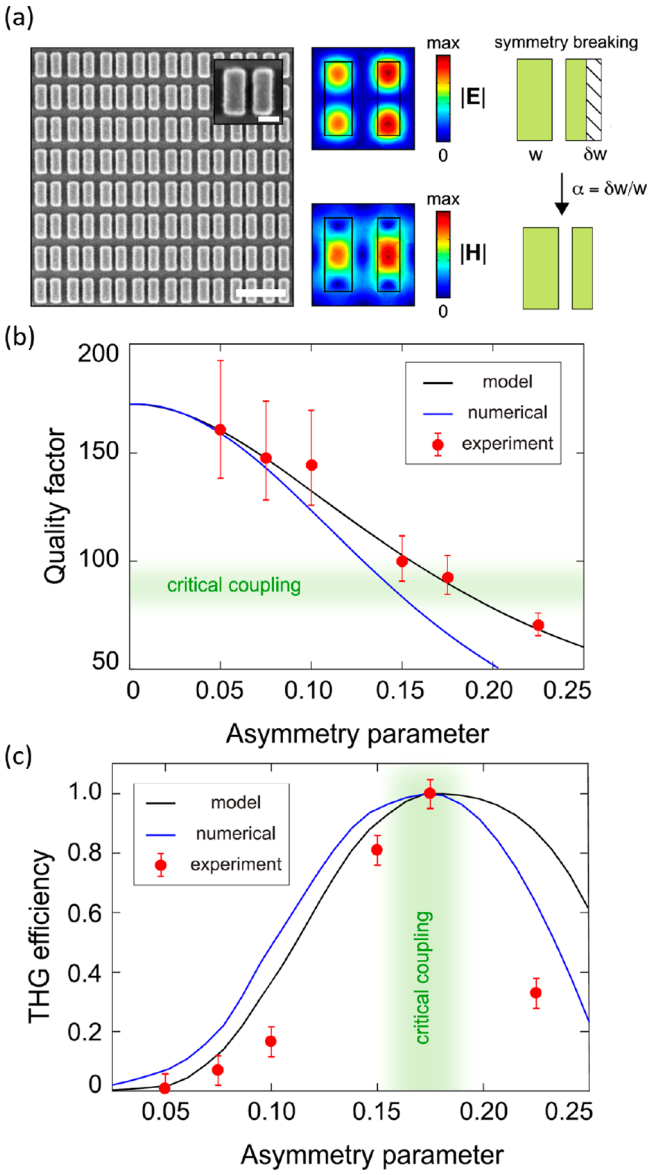

Figure 6. Critical coupling condition in a metasurface supporting a quasi-BIC resonance. (a) SEM image of a a-Si:H metasurface (left), with electromagnetic field distribution and illustration of the introduced asymmetry in a unit cell (right). Scale bars, 1 μm (main micrograph) and 200 nm (inset). (b) Measured dependence of the quasi-BIC resonance quality factor on the asymmetry parameter α. Solid lines correspond to the analytical (blue) and numerical models (black). (c) Corresponding experimental and theoretical THG efficiency. Adapted with permission from ref 158. Copyright 2019 American Chemical Society.

https://doi.org/10.1021/acsphotonics.1c01356
ACS Photonics XXXX, XXX, XXX−XXX

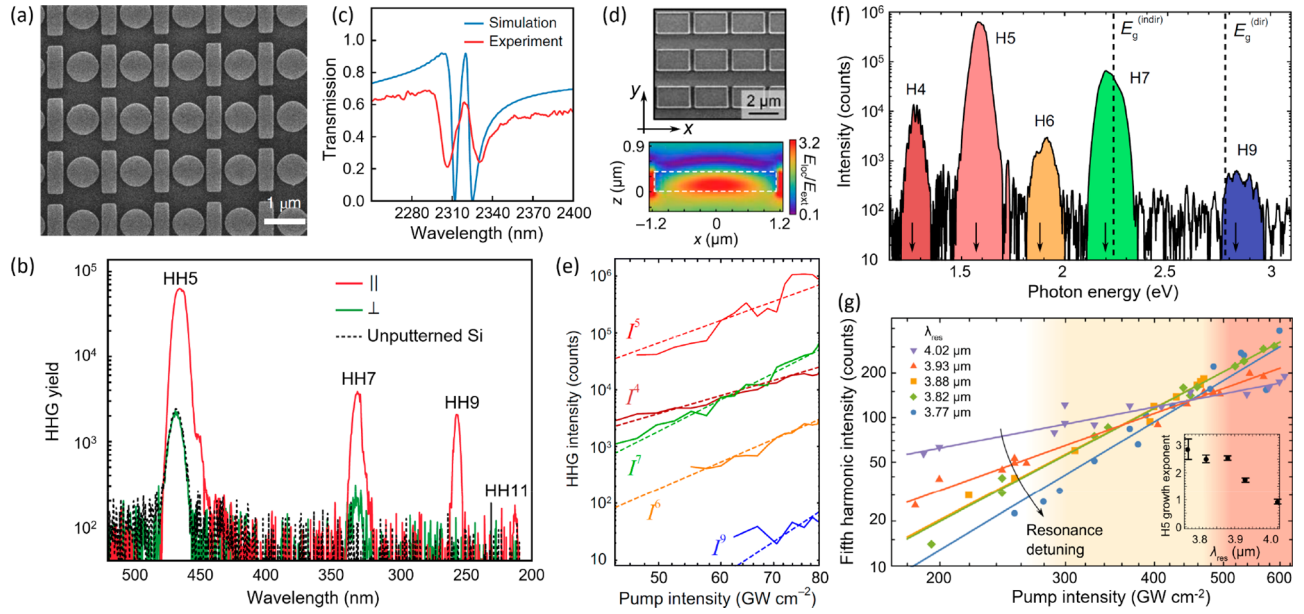

Figure 7. HHG in dielectric metasurfaces. (a) SEM image of a Fano-resonant Si metasurface studied for HHG. (b) HHG spectrum of the Si metasurface measured by pumping at 2320 nm at ~70 GW/cm^2, for incident light polarized parallel and perpendicular to the long axis of the bar. The case of unpatterned Si is included for reference. (c) Experimental and simulated transmission spectrum of the dielectric array showing a Fano resonance at ~2320 nm. (d) SEM micrograph of a GaP metasurface (top) and electric field distribution at its electric dipole resonance (3950 nm wavelength; bottom image). (e) Power dependence measurement of the HHG signals when pumping at resonance, showing a perturbative character. (f) HHG spectrum of the GaP metasurface when exciting at 3950 nm wavelength at 80 GW/cm^2. The eight harmonic was not detected as a consequence of the smaller efficiency of the even-order processes (as compared to the odd-order processes, for the employed crystal orientation), and the nonzero harmonic light reabsorption at the corresponding wavelength. (g) Single-pulse measurements of the fifth harmonic intensity at different pump wavelengths in the nonperturbative regime, showing how the growth exponent increases when detuning from the resonance. The beginning of the light orange shaded region (~280 GW/cm^2) marks the damage threshold of the resist mask covering the metasurface, while the dark-orange region (starting at ~480 GW/cm^2) indicates optical damage of the actual metasurface. (a−c) Adapted with permission from ref 167. Copyright 2018 Springer Nature. (d−g) Adapted with permission from ref 31. Copyright 2021 Springer Nature.

near-field distributions in Figure 6a. The symmetry-breaking parameter characterizing the quasi-BIC is defined as $\alpha = \delta w/w$, so that when $\alpha \to 0$, $Q_r \to \infty$ and $Q \to Q_{nr}$. Figure 6b shows the dependence of the resonance quality factor on α, from which a value of $Q_{nr} \sim 175$ was extracted. Notably, as is observed in Figure 6c, the THG efficiency is not maximum at the largest Q, but it is when the critical coupling condition is satisfied, that is, when $Q \sim 90$ ($Q_r = Q_{nr}$). It is pointed out that this regime was not reached in the T-shape metasurface described in Figure 5e−h, as Q_{nr} was much higher than Q_r, and therefore, the metasurface stood on the far right side of the critical coupling curve, which is also the limit assumed in most theoretical works. In this regard, numerical predictions on quasi-BIC resonances (neglecting nonradiative losses) compute THG normalized conversion efficiencies around 10^{-5} W^{-2} for a single Si resonator on SiO_2/ITO/SiO_2 (same configuration as that in Figure 3a),[160] and about 10^{-2} W^{-2} for a metasurface similar to the one in Figure 6, but where the asymmetry is introduced in the length of one of the bars rather than in the width.[161] Such a metasurface was found to feature a local maximum in the quality factor on the order of 10^5 for a relatively large asymmetry parameter ($\alpha \sim 0.25$) due to the concurrent destructive interference of different leakage channels forming an "accidental" BIC.

Polarization and Directionality. The control of the TH emission directionality and polarization can be exploited in an analogous way to SHG. However, an important difference is that of the symmetry of the second- and third-order processes, where in many cases the THG third-order susceptibility tensor can even be reduced to a constant. In isotropic or low-anisotropy crystals, the vectorial nature of the excited modes at the fundamental wavelength has a direct effect in the generated TH fields. In this scenario, Melik-Gaykazyan et al.[127] demonstrated high-intensity TH emission with a polarization character beyond linear polarization by structuring the pump beam for the selective excitation of magnetic or electric resonances in a-Si nanodisks. By choosing either azimuthal or radial input polarizations, exclusive excitation of magnetic or electric quadrupolar modes was achieved, changing accordingly the polarization state of the nonlinear emission.

The directionality of the TH radiation in single cylinder resonators was theoretically addressed by Smirnova et al.[140] An individual a-Si nanodisk can produce either forward or backward nonlinear emission by appropriately tuning the contribution of the different nonlinear multipoles excited, in a similar way as for SHG using (110)-AlGaAs disks[30] (Figure 4c,d), but without the possibility of forward-to-backward switching through pump polarization rotation, due to the more symmetrical nature of the third-order susceptibility tensor. This characteristic will be further analyzed below in the text when discussing THG wavefront control. Wang et al.[162] explored the TH radiation of a dimer of Si nanodisks excited at a superposition of (mainly) electric and magnetic dipole modes, attaining 11:1 forward-to-backward ratio for linear input polarization along the axis joining the disks. The emission could be turned off when uncoupling the nanodisks by rotating the pump polarization by 90° (20:1 TH intensity

https://doi.org/10.1021/acsphotonics.1c01356
ACS Photonics XXXX, XXX, XXX−XXX

contrast between the two polarization conditions was achieved).

HIGH HARMONIC GENERATION

Research on harmonic generation above the third harmonic order (i.e., high harmonic generation, HHG) has concentrated mostly on the gas phase of matter for many years. The phenomenon originates (in the semiclassical picture) from electron tunneling ionization at very high laser fields, followed by electron acceleration and recombination to the parent atom, accompanied by emitting radiation.[163] Applications of this process include sources of extreme ultraviolet light and soft X-rays, as well as attosecond pulse generation. It was not until 10 years ago that the investigation of HHG became also relevant in bulk solids,[164] opening the door to studies at subwavelength scales through nanostructuring. In nanoscale dielectrics, harmonic generation beyond SHG and THG has been studied only very recently, also addressing hybrid dielectric/gas systems.[165] Beyond their abilities for nonlinear resonant enhancement, nanostructures offer the possibility to efficiently extract generated harmonics at wavelengths within the absorption region of the material, as long as the smallest feature of the resonator is comparable to or smaller than the corresponding attenuation length. In the bulk, this distance becomes even smaller than the coherent length, inhibiting any phase matching effects required for efficient HHG.

Given that the probability of simultaneously absorbing N photons reduces with increasing N, larger pump intensities are needed to produce HHG with comparable efficiencies to lower order harmonics like SHG and THG. This directly implies entering the nonperturbative regime, where the intensity of the emitted light does not scale any more as a power law of the excitation intensity with an exponent equal to the order of the process. In this regime, the physics behind the generation of harmonics relies on intraband carrier dynamics in the individual bands, as well as interband electron−hole excitation and recombination, where the latter effect can be related to the case of HHG in gases. In particular, when the energy of the harmonic is smaller than the bandgap energy of the dielectric, the intraband mechanism is expected to govern.[166]

The first article on HHG in dielectric nanoantennas or metasurfaces, authored by Liu et al.,[167] reported the measurement of odd harmonics up to the 11th order in a Fano-resonant Si metasurface with a unit cell comprising a disk coupled to a bar (see SEM image in Figure 7a). This design is inspired in the work by Yang et al.[123] for THG, described above. The fabricated metasurface supports a Fano resonance when exciting with polarization parallel to the bar at a wavelength of ∼2320 nm, as can be seen in the transmission spectrum of Figure 7c. Nonlinear characterization of the sample exhibited an emission enhancement of up to more than 2 orders of magnitude compared to the unpatterned sample, upon resonant excitation, as is observed in Figure 7b. Even harmonics were not detected in the experiment given the centrosymmetric crystal structure of Si. The growing exponent of the nonlinear signal intensity with the pump power was found to be smaller than the order of the process and further decreased with increasing excitation power, indicating a nonperturbative character. When pumping the metasurface at 70 GW/cm^2, the fifth harmonic conversion efficiency was estimated at $>5 \times 10^{-9}$. It should be noted, however, that the excitation spectrum of the femtosecond laser used was significantly wider than the pumped Fano resonance (as much as an order of magnitude difference in line width in wavelength), and therefore, only a small fraction of the incident power actually coupled to the resonance. As a positive aspect, this experimental condition enabled keeping nearly resonant excitation even if the resonance wavelength shifted due to the high-power densities involved. Another study by Zograf et al.[168] focused on HHG at a quasi-BIC resonant a-Si metasurface using the same design as in Figure 6a, also revealing odd harmonics up to the 11th order. By registering curves of the nonlinear efficiency versus the degree of asymmetry α, the authors discovered that the critical coupling condition occurred at lower values of α for increasing pump power. To explain this behavior, they modeled the induced changes in the complex refractive index of the dielectric associated with the enhanced electron−hole plasma density generated by the large incident powers. As a result, the mode quality factor was found to reduce for rising excitation intensity, and therefore, the asymmetry parameter needed to be lowered to compensate for this effect. Simulations also showed that the quasi-BIC resonance blue-shifted with growing incident power.

Even and odd HHG up to the ninth harmonic was very recently demonstrated by Shcherbakov et al.[31] in a metasurface made of noncentrosymmetric GaP. The meta-atoms consisted of rectangular patches supporting an electric dipole resonance at 3950 nm wavelength (see SEM image and computed electric field distribution at resonance in Figure 7d). Different from the above reviewed high-Q Si reports, the resonance in this case was a few hundreds of nanometers wide and approximately matched the spectral width of the femtosecond laser beam utilized for the pump. Notably, a perturbative behavior was detected in the power dependence measurement for all harmonics up to a pump intensity of (at least) 80 GW/cm^2, as is evident from Figure 7e (the measured HHG spectrum is presented in Figure 7f). To access the nonperturbative regime and avoid damage of the sample, a single-pulse excitation study was also performed, yielding a maximum conversion efficiency for the fifth harmonic of 1.4×10^{-6} at 200 GW/cm^2. In this regime, the corresponding growth exponent with increasing pump intensity lowered drastically, from 5 (perturbative case) to 0.9. However, this coefficient was found to increase when detuning the fundamental wavelength from the resonance (see Figure 7g), given the associated reduction in the field enhancement and hence effective excitation density. For resonant excitation, the damage threshold was found to be ∼280 GW/cm^2 for the resist mask covering the metasurface and ∼480 GW/cm^2 for the actual metasurface. Regarding the output polarization state, while odd orders were copolarized with the fundamental beam, even harmonics showed elliptical polarization due to the asymmetric structure of the even-order susceptibility tensors.

Theoretically, a ZnO nanodisk metasurface on gold has been proposed for HHG up to the 21st harmonic when pumping at 1550 nm, with conversion efficiencies running from 10^{-12} (21st harmonic) to 10^{-7} (9th harmonic) at ∼70 GW/cm^2.[169]

WAVE MIXING

Wave mixing phenomena involve the coherent interaction in a nonlinear medium of two or more incident waves with at least two different frequencies from which light with new frequencies is produced. They are important for signal processing applications,[170] supercontinuum generation,[171] nonlinear imaging,[172] and entangled photon-pair creation,[173]

https://doi.org/10.1021/acsphotonics.1c01356
ACS Photonics XXXX, XXX, XXX−XXX

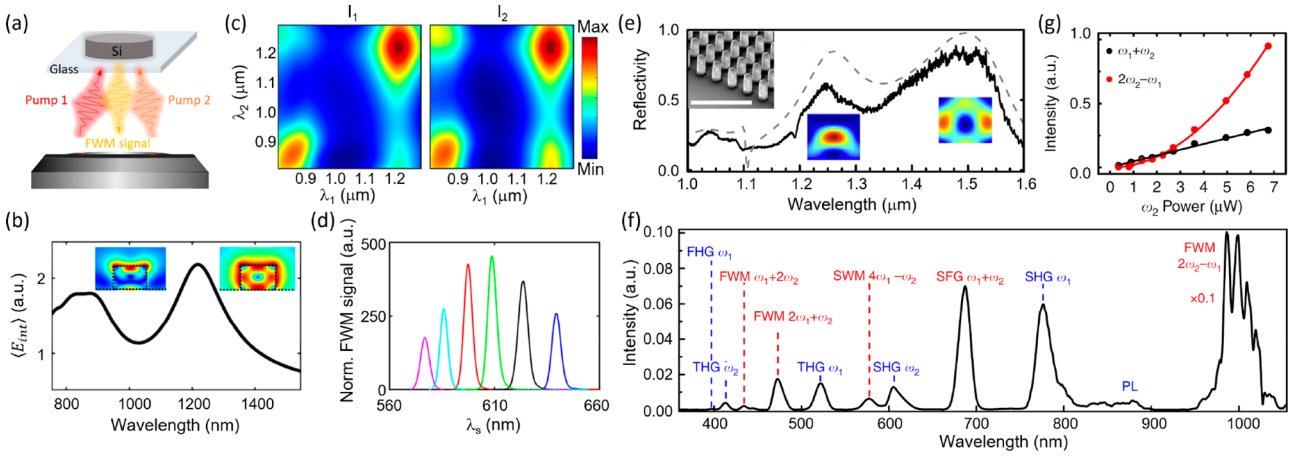

Figure 8. Wave-mixing processes in dielectric nanoantennas and metasurfaces. (a) Schematic of a Si nanodisk on glass analyzed for DFWM. (b) Simulated spectrum of the electric field enhancement averaged inside the dielectric, together with the electric field distributions at the two observed peaks. (c) Dependence of the nonlinear overlap integrals I_1 (left) and I_2 (right) on the two incident wavelengths λ_1 and λ_2. See text for corresponding equations. (d) Experimental DFWM signal of the nanodisk at output wavelength λ_s when pumping at λ_1 = 810 nm while varying λ_2. (e) Reflectivity spectrum of a (100)-GaAs nanodisk metasurface with SEM image displayed in the inset (scale bar, 3 μm). The electric field distributions inside a single meta-atom at the two main maxima, corresponding to the electric (1246 nm) and magnetic (1535 nm) dipole modes, are also shown. (f) Nonlinear output of the metasurface when simultaneously pumping at the electric and magnetic resonances. PL stands for photoluminescence. (g) Dependence of the intensity of the SFG and DFWM signals when varying the power of one of the pump beams. (a–d) Adapted with permission from ref 175. Copyright 2019 American Chemical Society. (e–g) Adapted with permission from ref 29. Copyright 2018 Springer Nature.

among several other uses. Their description through the nonlinear polarization can be extended from the case of harmonic generation by considering multiple frequency components for the fundamental fields. The output frequencies resulting from the nonlinear interactions are consequently multifold. For pumping frequencies $\omega_{1,2}$, second-order wave-mixing processes generate frequencies $\omega_1 \pm \omega_2$ ($\omega_1 > \omega_2$), where the plus and minus signs correspond to sum frequency generation (SFG) and difference frequency generation (DFG), respectively. Similarly, third-order wave-mixing effects with input frequencies ω_{1-3}, referred to as four-wave mixing (FWM), produce all positive-valued combinations of $\pm\omega_1$ $\pm\omega_2$ $\pm\omega_3$. The extension to higher-order wave-mixing phenomena is straightforward. When only two incident frequencies are considered in FWM (i.e., $\omega_2 = \omega_3$), the process receives the name of degenerate FWM (DFWM).

The first reported study on DFWM in resonant nanostructured dielectrics was performed on a-Ge single nanodisks,[174] where the importance of the spatial overlap in the resonator between the modes at the two pump wavelengths was addressed. It was found that the wave-mixing emission diminished when exciting at modes with different field distribution inside the dielectric, compared to using wavelengths at opposite sides of the same resonance peak. Later, Colom et al.[175] analyzed in more detail a single poly-Si nanodisk for DFWM (see illustration of the experiment in Figure 8a). Figure 8b exhibits the spectral dependence of the electric field averaged inside the dielectric, where two peaks at about 1200 and 800 nm wavelengths can be distinguished. They correspond, in that order, to a magnetic dipole and an electric dipole with contribution from a magnetic quadrupole, following a multipolar decomposition performed by the authors. For isotropic poly-Si, the nonlinear polarization associated with the studied $2\omega_1 - \omega_2$ output can be shown to be $\mathcal{P}(2\omega_1 - \omega_2) = 6\varepsilon_0\chi^{(3)}_{1122}(\mathbf{E}(\omega_1)\cdot\bar{\mathbf{E}}(\omega_2))\mathbf{E}(\omega_1)$, so that the

$$+ 3\varepsilon_0\chi^{(3)}_{1221}(\mathbf{E}(\omega_1)\cdot\mathbf{E}(\omega_1))\bar{\mathbf{E}}(\omega_2)$$

relevant overlap integrals to be considered for the pump beams inside the volume Ω of the disk are $I_1 = |\int_\Omega (\boldsymbol{E}(\omega_1)\cdot\bar{\boldsymbol{E}}(\omega_2))\boldsymbol{E}(\omega_1)\ \mathrm{d}\Omega|$ and $I_2 = |\int_\Omega (\boldsymbol{E}(\omega_1)\cdot\boldsymbol{E}(\omega_1))\bar{\boldsymbol{E}}(\omega_2)\ \mathrm{d}\Omega|$. Figure 8c shows the results of these integrals for different pairs of λ_1 and λ_2 (corresponding to frequencies ω_1 and ω_2, respectively). Looking at the diagonals of the contour plots reveals the trivial case of $\lambda_1 = \lambda_2$, marking the limit for the maximum possible spatial overlap value. Near the ends of the cross-diagonals, two maxima associated with the pair of peaks in Figure 8b are observed, which are smaller but comparable to the diagonal maxima, indicating a good mode overlap condition. Figure 8d displays the measured DFWM signals at emission wavelengths λ_s when keeping λ_1 fixed at the 810 nm resonant peak and varying λ_2 between 1100 and 1300 nm. As expected, the highest emission is detected when tuning λ_2 at the magnetic dipole (1200 nm). Compared to the unstructured film, the nanoantenna showed a nonlinear enhancement of more than 2 orders of magnitude. A theoretical work studied later the efficiency of the DFWM process for a Si disk on a SiO_2/ITO/SiO_2 substrate[160] and found that double pumping at the magnetic quadrupole mode and a quasi-BIC resonance yielded an efficiency 50× larger compared to exciting the system at the magnetic dipole and quadrupole modes, which is a similar situation to that described in Figure 8a–d. A further 6 orders of magnitude enhancement, yielding normalized conversion efficiencies as high as ~60 W^{-2} has been predicted by Moretti et al.[111] when exciting a GaP metasurface at two different quasi-BIC resonances.

Liu et al.[29] investigated a (100)-GaAs metasurface with disk meta-atoms using dual excitation at spectrally separated electric and magnetic dipole modes (see reflectivity spectra, field distributions and SEM image of the sample in Figure 8e). As shown in Figure 8f, the experiment detected even and odd order nonlinear mixing processes, including SFG, DFWM, and degenerate six wave mixing (DSWM, the fifth order analog of DFWM), along with SHG, THG, and fourth harmonic generation (FHG) originating from the individual beams.

https://doi.org/10.1021/acsphotonics.1c01356
ACS Photonics XXXX, XXX, XXX−XXX

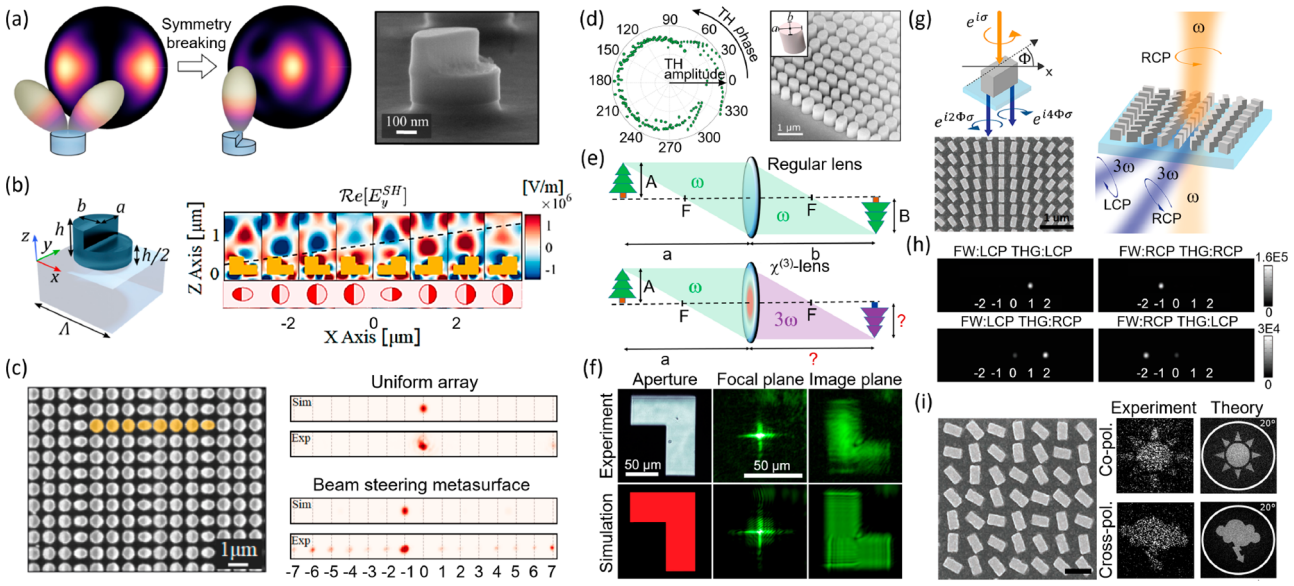

Figure 9. Nonlinear wavefront control and imaging with dielectric metasurfaces. (a) Left: Schematic comparison of the SH radiation pattern of a nanodisk and a nanochair made of (100)-AlGaAs. Right: SEM image of a fabricated AlGaAs nanochair meta-atom. (b) Left: Geometrical parameters of the nanochair meta-atom, where h = 400 nm, Λ = 900 nm, and semiaxes a and b take values in the 200−400 nm range. Right: Near-field SH profile in the vicinity of a $0-2\pi$ phase gradient supercell, designed to build a beam-steerer metasurface. (c) Left: SEM micrograph of the fabricated SH beam-steerer metasurface, where a supercell is highlighted in yellow. Right: Measured and simulated diffraction patterns of the beam-steerer metasurface and a uniform array with identical meta-atoms. (d) Left: Numerically computed TH phase and amplitude of Si nanopillars of varying elliptical basis, designed for $0-2\pi$ nonlinear phase control at nearly constant amplitude (1550 nm pump wavelength). Right: SEM image of a fabricated metalens using a radial phase distribution. (e) Illustration comparing the investigated TH nonlinear imaging of objects with its linear counterpart. (f) Experimental and simulated nonlinear imaging of an L-shape aperture with a metalens as that in (d). (g) Schematic illustrations and SEM image of a a-Si beam-steerer metasurface using the Pancharatnam-Berry geometric-phase approach for wavefront control of the TH emission for circularly polarized light excitation. RCP and LCP stand for right circularly polarized and left circularly polarized, respectively. (h) Experimental RCP and LCP TH diffraction patterns of the metasurface for incident RCP and LCP light. (i) Left: SEM image of a nanofin metasurface with embedded nonlinear hologram. Scale bar, 500 nm. Right: Experimental demonstration of nonlinear holographic multiplexing, where different holograms are produced depending on the observed polarization state of the TH output. (a−c) Adapted with permission from ref 121. Copyright 2021 Optica Publishing Group. (d−f) Adapted with permission from ref 33. Copyright 2020 American Chemical Society. (g−i) Adapted with permission from refs 8 and 178. Copyright 2019 American Chemical Society and Copyright 2020 John Wiley and Sons, respectively.

The strongest signal was found to be the DFWM emission, as it was the only output with wavelength in the transparency region of GaAs. Conversion efficiencies about 10^{-6} to 10^{-5} were determined for the second- and third-order frequency-mixing processes. However, it should be noticed that the field spatial overlap at the fundamental wavelengths was far from optimal, as the electric dipole mode had its maximum field accumulated where the magnetic dipole had a minimum (see Figure 8e). In fact, to produce such efficiencies, peak pump intensities as high as ~10^3 GW/cm^2 (at 1 kHz repetition rate, to minimize heating dissipation) were utilized. Nevertheless, as seen in Figure 8g, linear and quadratic power dependences of the DFWM ($2\omega_2 - \omega_1$) and SFG ($\omega_1 + \omega_2$) signals were still observed in this range when varying the ω_2 pump intensity, respectively, indicating a perturbative regime. More recently, Camacho-Morales et al.[176] demonstrated an improved nonlinear performance for SGF in a (110)-GaAs nanodisk metasurface, achieving a normalized conversion efficiency of 8×10^{-9} W^{-1}, compared to 4×10^{-10} W^{-1} for the report presented in Figure 8e−g. The increased response is attributed to the better spatial overlap of the pumped modes, both containing electric and magnetic dipole contributions, and the more directional emission toward the collecting lens, as enabled by the particular crystalline cut.

Zilli et al.[148] investigated a (100)-AlGaAs nanodisk for frequency tripling via SFG, by pumping the resonator at ω and 2ω ($3\omega = \omega + 2\omega$), so that the SFG signal is degenerate with THG. The nanonantenna was excited at the magnetic dipole or anapole resonance for the lower energy pump, by tuning the disk diameter. Given that the THG emission observed at single beam excitation was more than an order of magnitude smaller than the signal at dual-beam excitation, the latter was attributed principally to the second-order nonlinear processes. The SFG normalized conversion efficiency was determined to be 1.2×10^{-10} W^{-1}, which is smaller compared to the discussed GaAs metasurfaces. The difference in efficiency can be attributed to the (apparent) absence of an engineered resonance at the 2ω pump frequency in the case of the AlGaAs nanodisk. Interestingly, the authors showed that the directionality of the emission toward the normal direction could be significantly improved by crossing the polarization at ω for the anapole state with respect to the beam at 2ω, due to the symmetry of the nonlinear susceptibility tensor and the excited field distributions.

NONLINEAR WAVEFRONT CONTROL AND IMAGING

Photonic metasurfaces have been widely studied for wavefront manipulation of electromagnetic waves in the linear regime. By tailoring the amplitude, phase, and polarization state of the incident light at the subwavelength level, a wide variety of functionalities have been demonstrated, including beam steering, polarization beam splitting, optical vortex generation, lensing, and holography.[177] Extending these and other

https://doi.org/10.1021/acsphotonics.1c01356
ACS Photonics XXXX, XXX, XXX−XXX

operations to nonlinear metasurfaces can be achieved by locally endowing the desired optical properties to the generated nonlinear radiation. The ideal starting point for nonlinear phase control at constant amplitude is a meta-atom emitting in a defined direction (e.g., along the vertical axis) with the desired phase at maximum nonlinear conversion efficiency. By encoding the adequate phase pattern into a packed array of such meta-atoms, control of the directionality of the SHG or THG emission,[8,32,121,178] as well as nonlinear imaging,[33,176] vortex generation,[32] and holography,[7,8,178] have been proven experimentally.

Gigli et al.[121] investigated a (100)-AlGaAs "nanochair" meta-atom to build nonlinear metasurfaces for beam steering and subwavelength focusing of the SH radiation. As illustrated in Figure 9a, the height difference between the two halves of the cylinder defining the nanochair can turn the sideways SH emission distribution of the full cylinder into a vertical radiation pattern[120] due to the symmetry of the corresponding second-order nonlinear susceptibility tensor, as previously discussed. Numerically sweeping through a wide range of geometrical parameters and computing the output SH phase and amplitude, the authors noticed that they could obtain any phase in the $0-2\pi$ range at nearly constant amplitude (i.e., SH efficiency, of order 10^{-5}). By choosing the adequate lateral dimensions of the elliptical basis and in-plane orientation of the nanostructure, eight different meta-atoms were devised to build the unit cell of the beam steering metasurface. Figure 9b (right panel) shows the SH near-field distribution in the vicinity of each of the eight resonators, arranged to produce a $0-2\pi$ linear phase gradient. By repeating such a supercell in a periodic lattice, a sawtooth phase profile metasurface was built to direct the SH beam at an angle of 6.2° with respect to the vertical axis. The SEM image of the fabricated metasurface (one supercell is highlighted in yellow for clarity) and corresponding far-field nonlinear image can be seen in Figure 9c. Nearly 50% of the SH light collected within a numerical aperture of 0.8 corresponded to the first order. Nonlinear Fresnel metalenses with numerical apertures of 0.2 and 0.5 were also successfully fabricated with the same kind of meta-atom, using a hyperboloidal phase pattern for the SH emission.

Different to the case of SHG, a single Si cylinder excited at a superposition of electric and magnetic dipole modes with comparable amplitudes can already provide directional TH emission along the normal axis, due to the more symmetric nature of the third-order nonlinear susceptibility tensor. A representative result of the computed TH phase and amplitude for Si pillars with different elliptical bases is shown in the left panel of Figure 9d, where a collection of elements yielding nearly constant amplitude with phases spanning the $0-2\pi$ range can be defined. Based on this concept, Wang et al.[32] produced a sawtooth phase array as that in Figure 9c, but for THG, using a set of Si nanopillars with different lateral dimensions, demonstrating more than 90% diffraction efficiency (defined as the proportion of TH light emitted in the forward direction going to the first order). The TH conversion efficiency of each of the dielectric resonators was of order 10^{-6}, and more than 90% of the emitted TH light was radiated in the forward direction. This type of meta-atom was also employed to produce a nonlinear vortex beam generator, as well as a lens for nonlinear imaging,[33] where the concept for the latter is schematized in Figure 9e (see also illustration in Figure 1). The object to be analyzed is illuminated with an infrared beam and the output light then directed to the metalens to produce a nonlinear image at the visible TH wavelength (see SEM image of a fabricated metalens in Figure 9d, right side). An imaging example is shown in Figure 9f, where an L-shaped aperture was used as the object. A relatively small ratio of the object distance to the lens with respect to the size of the aperture was used to keep the nonlinear imaging process comparable to its linear counterpart. Increasing this ratio was found to produce strong third-order spatial correlation effects altering the generated image, which could be thought of as a nonlinear optical aberration. However, important information could also be attained in this situation, not available in the linear regime, about the spatial coherence of light arriving from the object. A different nonlinear imaging concept was developed by Camacho-Morales et al.,[176] where a linear infrared image is upconverted to visible wavelengths through SFG using an array of (110)-GaAs nanodisks. In this case, a target illuminated with infrared light is conventionally imaged on the dielectric metasurface, where the image is mixed with a second, high-power, infrared beam to produce a visible SFG output, which is then focused with a regular lens to form a second (visible) image.

Reineke et al.[8,178] investigated a Pancharatnam−Berry geometric-phase approach for nonlinear wavefront control in a-Si metasurfaces, demonstrating polarization-dependent TH beam steering and holographic multiplexing. In this method, the geometry of the meta-atom is kept fixed, and the local phase changes in the nonlinear emission are achieved through the in-plane rotation of the nanostructure. Circularly polarized excitation is used, maintaining a constant TH amplitude for the different orientations. While THG is forbidden in isotropic materials such as a-Si for circularly polarized light in the dipole approximation, it is expected to be nonzero in the metasurface as the symmetry is naturally broken. By modeling the THG response with an effective third-order nonlinear susceptibility, the authors show that rotating a meta-atom an angle Φ induces local nonlinear polarizations with geometric phases of $\pm 2\Phi$ and $\pm 4\Phi$. More specifically, when pumping with left (right) circularly polarized light, the TH emission in the forward direction carries a geometric phase of 2Φ (-4Φ) for the left circularly polarized output, and 4Φ (-2Φ) for the right circularly polarized output. This process is schematically represented in Figure 9g, where the meta-atom is a nanofin. By repeating this nanostructure with the appropriate orientations, a beam steerer metasurface was fabricated, as shown in the SEM image of Figure 9g. The corresponding diffraction patterns for left and right circularly polarized incidences and co- and cross-polarized outputs are shown in Figure 9h, demonstrating the four possible outputs. Keeping all nanofins parallel produces emission in the zeroth diffraction order. Nonlinear holograms designed through a modified Gerchberg−Saxton algorithm were also encoded in nanofin metasurfaces, where an example providing different images of a "sun" or a "thundercloud" for co- and cross-polarized TH emission is shown in Figure 9i. Note that as the phase information is determined only by the geometric orientation of the meta-atoms, it can be retrieved over a wide range of wavelengths. However, this geometric-phase model with circularly polarized excitation yields a very low conversion efficiency of order 10^{-10} given the isotropic crystal structure of a-Si and the lack of a resonant condition with high field confinement in the nanofin due to its subwavelength size. In contrast, metasurfaces with Mie-resonant meta-atoms under linearly polarized excitation can offer good-quality holograms

https://doi.org/10.1021/acsphotonics.1c01356
ACS Photonics XXXX, XXX, XXX−XXX

at the TH wavelength with conversion efficiencies orders of magnitude larger, as has been demonstrated using C-shaped Si resonators.[7] The disadvantage is that they require time-consuming numerical calculations to generate the adequate collection of meta-atoms, they are more sensitive to fabrication imperfections, as slightly different structures can produce very different phase outputs, and they do not (trivially) deliver multiplexing. It should be mentioned here that the Pancharatnam−Berry method was previously applied for phase control of the SH signal in a-Si metasurfaces,[74] but the measured conversion efficiencies were even lower than that for THG, about 10^{-14}, given the centrosymmetric crystal structure of the dielectric material.

Amplitude control of the TH signal, as opposed to phase control, has also been exploited in nanostructured dielectrics. Xu et al.[159] studied a Si metasurface supporting a magnetic dipole quasi-BIC resonance to produce different nonlinear images depending on the orientation of the input linear polarization. The meta-atom consisted of an ultrathin (50 nm thick) disk with a noncentered hole, introduced as the asymmetry to turn the underlying BIC into a polarization-sensitive quasi-BIC. The high-Q resonance could only be excited to produce appreciable THG using a polarization perpendicular to the line joining the hole with the center of the disk. Having different portions of the metasurface with off-axis holes in the x or y directions, the authors embedded TH images of an arrow pointing up (↑) or down (↓), which could only be read when pumping with vertical or horizontal polarizations, respectively. Alternatively, using disks of different sizes and tuning the wavelength instead of the polarization showed similar results. Kruk et al.[179] later used as meta-atom a Mie-resonant a-Si elliptical disk supported by a SiN pillar on a glass substrate to build metasurfaces delivering completely different nonlinear images depending on whether illuminating from the air or glass regions. By changing the elliptical basis, the unit element could either produce efficient THG when exciting from both air and glass sides or only when pumping from air or glass regions or remain dark for both illumination directions.

The enhancement of multiphoton-photoluminescence was also demonstrated in dielectric nanoantennas and metasurfaces,[180−183] and was exploited for optical encoding[181] using mid-index lead halide perovskite as the dielectric, as well as for mapping the magnetic field profile of the excitation beam.[182] The imaging of anapole states and higher order modes inside dielectric nanoantennas through THG scanning was also demonstrated.[138,184]

NONLINEAR ULTRAFAST OPTICAL MODULATION

Beyond frequency conversion and wavefront control at the emission wavelength, optical nonlinearities have also been exploited for ultrafast modulation of optical properties at the incident wavelength, taking advantage of the photoinduced refractive index changes resulting from the optical Kerr effect (OKE), two-photon absorption (TPA), free-carrier effects, and the thermo-optic effect. The time scale of the OKE and TPA is in the range of femtoseconds, while free-carrier and photothermal dynamics extend to the picosecond and nanosecond scales, respectively.[185] The strength of the various nonlinear processes can also be very different, where generally the fastest phenomena have the weakest intrinsic responses. In this Review, I limit myself to analyze the enhancement of optical nonlinearities in the sub-100 fs range originating from the OKE and TPA, which rely on the third-order susceptibility.

In dielectric nanoresonators, the OKE and TPA have been recently studied through pump−probe spectroscopy to produce nearly instantaneous reflectivity and transmission changes at the probe wavelengths.[11,12,186] In a pump−probe experiment, the OKE arises from the nonlinear polarization induced by the response of bound electrons to the incoming pump beam, which modifies the real part of the refractive index of the dielectric and hence its optical response to the probe beam. The fundamental time limit for this effect is estimated at ∼0.1 fs, based on the orbital period of an electron in its motion around the nucleus.[28] On the other hand, TPA varies the imaginary component of the refractive index, modulating the probe beam whenever a probe photon is simultaneously absorbed together with a pump photon. Once the pump beam is turned off, or as soon as the pump and probe pulses no longer temporally overlap, the probe signal immediately recovers its original condition (assuming there is no contribution from other slower photoinduced effects).

In this context, the complex refractive index of a nonlinear medium can be approximated as $\tilde{n} = \tilde{n}_0 + I\tilde{n}_2$, where $\tilde{n}_0 = n_0 + ik_0$ is the low-intensity complex refractive index, I represents the intensity of the pump beam, and $\tilde{n}_2 = n_2 + ik_2$ is the nonlinear complex refractive index. The OKE is responsible for the nonlinear index n_2, while the nonlinear absorption, k_2, relates to the TPA coefficient, β, through the equation $k_2 = (\lambda\beta)/(4\pi)$. In materials with negligible linear absorption (i.e., $k_0 \sim 0$), $n_2(\omega) \propto \chi_R^{(3)}(\omega)$ and $k_2(\omega) \propto \chi_I^{(3)}(\omega)$, where $\chi_R^{(3)}$ and $\chi_I^{(3)}$ are the real and imaginary components of $\chi_{iiii}^{(3)}(\omega; \omega, \omega, -\omega)$, respectively.[187] Following Miller's rule, high-index dielectrics generally possess large $\tilde{n}_2$ values, which can be effectively amplified through light confinement when nanostructuring. In addition, resonant profiles in the reflection/transmission spectrum can further magnify the induced optical variations. To produce clean ultrafast modulations, however, a detailed analysis on all mechanisms contributing to the transient dynamics need to be made, so as to engineer operating windows with complete absence of free-carrier and thermal heating components.[188] Also, the participating resonances must be spectrally wide enough to guarantee a sufficiently fast response, depending on the intended application.

Experimentally, pump−probe measurements performed on a-Si nanoantennas and metasurfaces[11,186] showed modulation depths (i.e., peak differential reflectivity or transmissivity) up to ∼0.5% with time responses as short as <10 fs, when probing at the magnetic dipole or anapole resonances at near-infrared wavelengths. While slower contributions did produce signals in the picosecond range, dispersion tailoring of the resonators enabled spectral regions with a pure ultrafast behavior. Increased modulation performances have been demonstrated using crystalline GaP,[12,189] as can be seen in Figure 10 for single GaP nanodisks. Different to the reported cases for a-Si, which used pumping energies within the absorbing range of the material, the studies on GaP were carried out in its transparency region, where free-carrier contributions and heating effects are minimized. Figure 10a (top graph) shows the differential reflectivity spectrum of GaP nanodisks of different diameters (D) at zero pump−probe delay time, when pumping (probing) with 7 fs pulses containing spectral components in the 650−750 nm (750−1000 nm) wavelength range. The peak modulation, corresponding to the minima in

https://doi.org/10.1021/acsphotonics.1c01356
ACS Photonics XXXX, XXX, XXX−XXX

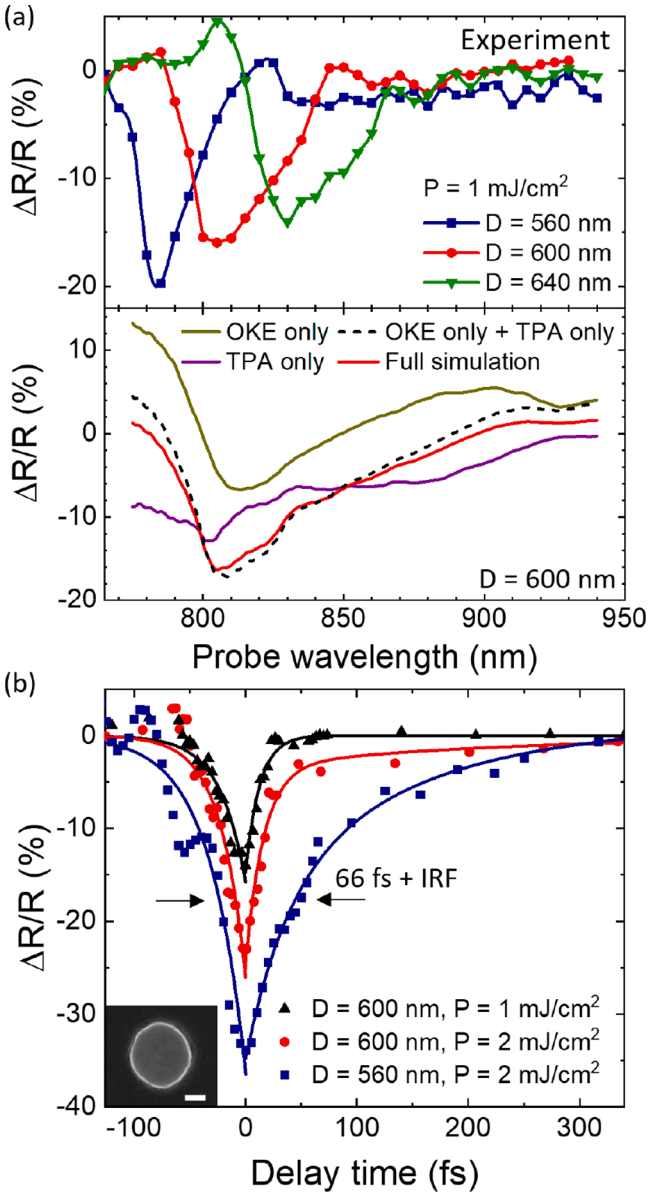

Figure 10. Nonlinear all-optical switching in a GaP nanodisk. (a) Top: Differential reflectivity spectrum of single GaP nanodisks taken at the pump−probe temporal overlap. Bottom: Corresponding numerical simulation for the case with diameter D = 600 nm, computed using experimental values of the Kerr nonlinear index and two-photon absorption coefficient as inputs. (b) Temporal traces for D = 560 and 600 nm, measured at resonance at different pump energy densities. IRF stands for instrument response function. The inset shows a SEM image of a measured GaP nanodisk. Scale bar, 200 nm. Adapted with permission from ref 12. Copyright 2020 The American Association for the Advancement of Science.

the graph, occurred when probing the nanoantenna in the vicinity of the anapole state. In this condition, the OKE and TPA processes contribute with the same modulation sign, with a 40%/60% OKE/TPA relative weight, while they cancel each other out at both lower and longer wavelengths (see nonlinear simulations in the bottom graph of Figure 10a). As shown in the resonant temporal traces in Figure 10b, a maximum differential reflectivity close to 40% with 66 fs fwhm was demonstrated when pumping at 2 mJ/cm^2, suggesting that GaP nanostructures could be promising candidates for ultrafast switching at modulation speeds up to 20 THz. For reference, Shcherbakov et al.[190] reported a modulation depth of 46% with ∼4 ps fwhm at 0.15 mJ/cm^2 when exploiting free-carrier effects in GaAs metasurfaces. That is, a similar differential reflectivity signal can be obtained with 1 order of magnitude smaller pumping power, at the cost of extending 2 orders of magnitude the temporal response of the modulator. It should be noted here that nonlinear refractive index changes using Kerr-type nonlinearities have also been used in mid-index dielectric metasurfaces to control the phase of structured light beams to tune their orbital angular momentum.[191,192]

ROLE OF TOPOLOGY

Topological photonics[193] is a highly active research field that finds inspiration in its condensed matter counterpart, where topological concepts were needed to fully understand the quantum Hall effect and later led to the development of topological insulators and several other topological phases.[194] Briefly, topology is a field of mathematics that studies properties of geometric objects relating to aspects that remain invariant under continuous shape transformations. An important theorem is that of Gauss−Bonnet, which states that the surface integral of the Gaussian curvature (K) of a closed surface object is equal to 2π times an integer number χ, known as the Euler characteristic, that is, $\iint_S K\, dA = 2\pi\chi$.[195] Such an integer number is a topologically invariant quantity, meaning that it remains constant under smooth geometric changes of the object. Geometries having a different Euler characteristic are said to be topologically distinct.

In condensed matter physics, physical properties that are conserved under certain groups of transformations are referred to as topological invariants and are said to be topologically protected. The simplest model describing this concept is that of Su−Shrieffer−Heeger,[196,197] which considers the tight binding problem of a linear chain with a two atoms basis, A and B (i.e., ···A-B-A-B···), with different hopping terms t_{AB} and t_{BA} for the A-B and B-A sections of the chain. When solving for the eigenstates $|n(k)\rangle$, depending on whether t_{AB} is larger or smaller than t_{BA}, a different integer number (0 or 1), called the *winding* number (ν), times π, is found when integrating the Berry potential ($\mathcal{A}_n = \langle n(k)|\nabla_k|n(k)\rangle$) in the first Brillouin zone, that is, $\oint \mathcal{A}_n(k)\, dk = \pi\nu$. Even though systems with $t_{AB} > t_{BA}$ and $t_{AB} < t_{BA}$ can have the exact same energy spectrum, described by two bands separated by a bandgap, they are topologically distinct as they have different ν values, where the chain having $\nu = 0$ is labeled as topologically trivial. Moreover, it can be shown that interfacing topologically distinct chains gives rise to localized states at the boundary, with corresponding eigen-energies within the bandgap. Such localized states are preserved under smooth changes in the Hamiltonian, as long as the chiral symmetry is maintained, and cannot be eliminated without closing the bulk energy gap. The same occurs when substituting the topologically trivial chain with vacuum, as they are topologically equivalent. When increasing the number of spatial dimensions and exploiting different physical phenomena, many topological invariants (such as the winding number) emerge. For example, the Quantum Hall effect, which arises at the interface between vacuum and a 2D electron gas system under an applied magnetic field, is described by a nonzero Chern number, which can be linked to the quantized Hall conductance at the edge.[196] The quantum spin hall effect, also known as the 2D topological

https://doi.org/10.1021/acsphotonics.1c01356
ACS Photonics XXXX, XXX, XXX−XXX

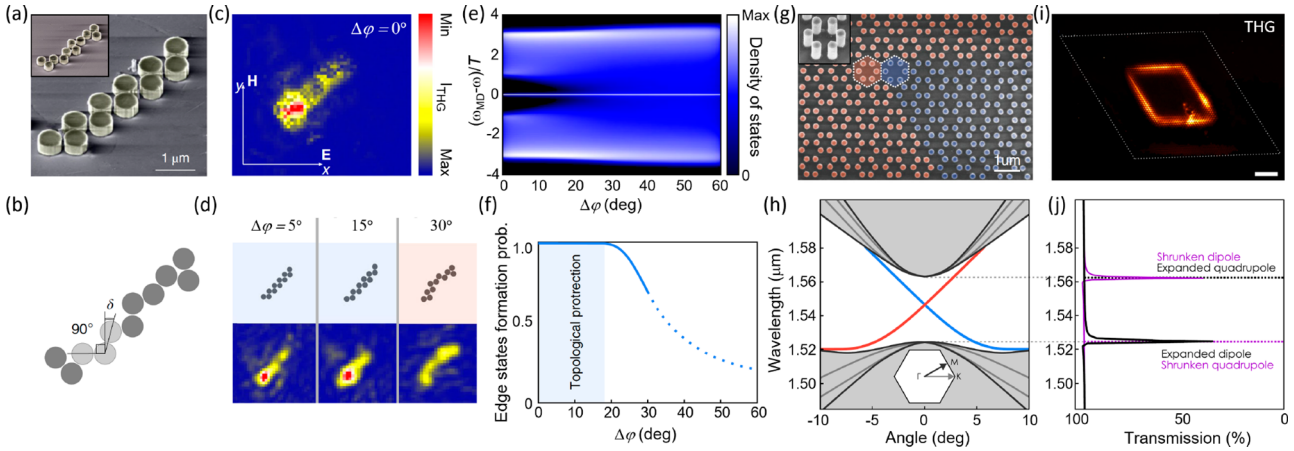

Figure 11. Topological nonlinear nanophotonics. (a) SEM image of a Mie-resonant chain of Si nanodisks studied for THG. The inset shows a case with added disorder explored for topological protection of edge states. (b) Schematic illustrating the analyzed disorder parameter δ. Random zigzag angles $-\Delta\varphi \leq \delta \leq \Delta\varphi$ are introduced along the chain. (c, d) THG images of undistorted (c) and distorted (d) chains with different $\Delta\varphi$ values. (e, f) Theoretical calculations of the photonic density of states (e) and formation probability of edge states (f) when varying $\Delta\varphi$. MD stands for magnetic dipole. (g) SEM image of an array of interfacing contracted (red) and expanded (blue) hexamers of Si nanopillars. Only the top left corner of the parallelogram-shaped domain wall is displayed. The inset shows an amplified view of a single hexamer. (h) Computed photonic band diagram of the array. Red and blue lines correspond to dispersion curves of the edge states. (i) THG image of the sample when pumping at 1533 nm (i.e., within the photonic bandgap). Scale bar, 10 μm. (j) Calculated transmission spectrum of the metasurface showing the origin of the photonic bandgap and the band inversion. (a–f) Adapted with permission from ref 34. Copyright 2019 Springer Nature. (g–j) Adapted with permission from ref 198. Copyright 2019 American Physical Society.

insulator, does not require external fields and supports an insulating bulk state with chiral spin currents at the boundaries, which are protected by time-reversal symmetry and are characterized by the so-called $\mathbb{Z}_2$ invariant.

In photonics, the analogy appears when considering the formation of photonic bands. In nonlinear nanophotonics, the first work exploring topological features was reported in 2019 by Kruk et al.,[34] who studied the THG response of a zigzag array of dielectric cylinders resembling the Su–Shrieffer–Heeger chain. The analyzed design is shown in Figure 11a, consisting of 11 Si nanodisks defining a linear array with a two meta-atoms basis. To characterize the topological stability of the system against structural disorder, the authors fabricated several arrays with random "bond angles" every three consecutive disks, as illustrated in Figure 11b, generated by shifting the 90° angle of the undistorted chain by random δ values uniformly distributed in the range $[-\Delta\varphi, \Delta\varphi]$. Such a distortion preserves the chiral symmetry of the Hamiltonian, and hence, any edge state with energy within the photonic bandgap will be topologically protected. As shown in Figure 11c, the case with $\Delta\varphi = 0°$ delivers strong THG at the edge of the chain, resulting from the resonant field enhancement provided by the excited Mie modes combined with further topological localization of the electric field at the end of the array (see illustration in Figure 1). The authors also found that the degree of localization significantly improved when extending the length of the array by adding more disks, consistent with the topological nature of the observed effect. Moreover, theoretical calculations show that only when $\Delta\varphi$ exceeds ~20°, the bandgap characterizing the photon density of states vanishes, breaking the topological protection of the degenerate edge states, as is evidenced in Figure 11e,f. Experimentally, a similar result is registered when evaluating the THG spatial distribution at different $\Delta\varphi$, as can be seen in Figure 11d (see example of a disordered chain in the inset of Figure 11a). As long as $\Delta\varphi < 20°$, the THG enhancement at the edge of the chain will be topologically protected. The design of nanostructures supporting topologically protected states that enhance nonlinearities can be of great importance for applications due to the robustness against fabrication imperfections, where the concept could eventually even be applied to self-assembled nanosystems like chains of colloidal nanoparticles.

The nanophotonic equivalent of the 2D topological insulator has also been demonstrated using Si cylinders, by interfacing arrays of shrunken and expanded hexamers of nanodisks, as shown in the SEM image of Figure 11g.[198] Such a domain wall presents a topological phase transition characterized by band inversion, where Hamiltonians on each side of the interface cannot be continuously deformed into one another without closing the gap. As is observed in Figure 11h,j, dipolar (quadrupolar) and quadrupolar (dipolar) contributions describe the top (bottom) and bottom (top) bands of the shrunken (expanded) array, respectively. When exciting the topologically protected edge states (blue and red lines within the gap in Figure 11h), enhanced THG is produced only at the boundary, as can be seen in Figure 11i. The phenomenon was found to be present for domain walls of arbitrary shapes, as expected from the topological origin of the studied effect. In addition, right and left guided THG modes along the edge were demonstrated when pumping at a focalized spot next to the edge with either right or left circularly polarized light, respectively, in analogy with the spin-momentum locked electrical currents in the 2D topological insulator. Such waveguiding modes cannot scatter in the backward direction, even when the interface has sharp corners, as the counter-propagating states are topologically decoupled. More recently, in a similar system, Kruk et al.[199] reported the presence of higher-order topological effects leading to 0D corner states living in a mini-bandgap of the 1D edge states, also giving rise to topologically localized and enhanced THG emission. A complete review on nonlinear topological photonics can be found in ref 200.

https://doi.org/10.1021/acsphotonics.1c01356
ACS Photonics XXXX, XXX, XXX–XXX

CONCLUSIONS AND PERSPECTIVES

In this Review, I have examined the main achievements in the field of nonlinear dielectric nanoantennas and metasurfaces with a focus on harmonic generation, wave-mixing effects, nonlinear wavefront control, ultrafast all-optical modulation, and topology. A rapid growth has been observed in the past years in terms of SHG and THG conversion efficiencies, currently reaching values around 0.01%,[42,51,136] with normalized conversion efficiencies up to $\sim 10^{-2}$ W^{-1} (SHG)[58] and $\sim 10^{-5}$ W^{-2} (THG).[106] Numerical predictions anticipate an increase of up to two[110,111] and three[161] orders of magnitude for the normalized values, respectively, based on novel designs of quasi-BIC resonant metasurfaces. High-Q quasi-BIC resonances are receiving tremendous attention at present, as they can highly exceed Mie modes or anapole states in confining electromagnetic fields. A substantial amount of research is expected in this area, accompanied by further advancements in nanofabrication, needed to precisely define the small structural asymmetries characterizing the quasi-BIC systems. It has been also pointed out, however, that maximum absolute conversion efficiencies may not exceed 0.1% given the refractive index changes induced in the dielectric at high pump intensities.[112]

The use of other materials beyond III−V, II−VI, and IV−IV semiconductors and single-element dielectrics could also have a role on improving the nonlinear performance of nanoscale structures. Transition metal dichalcogenides, such as MoS_2, WS_2, $MoSe_2$, and WSe_2, have a very high refractive index (MoS_2 has $n = 5$ and $k = 0$ at 750 nm) and have been reported recently for enhanced harmonic generation through nanopatterning,[201−203] although fabrication control is still behind that of mature semiconductor technologies and the observed nonlinear responses are still relatively poor. Double nonlinear enhancement at geometrical and excitonic resonances could also be a promising avenue for these materials,[203] and specially for perovskites featuring direct bandgap with large excitonic effects.[204] Unpatterned mid-index hybrid organic−inorganic 2D perovskite crystalline films of sub-100 nm thickness have demonstrated resonant visible TH emission at their excitonic wavelengths with conversion efficiencies close to 10^{-4} at <10 GW/cm^2.[205] Integrating monolayer or few-layers semiconductors with dielectric metasurfaces may also become a favorable route to endow additional nonlinear functionalities to the metasurface.[206−210] For example, few-layers GaSe coupled to THG-emitting Fano-resonant[206] or quasi-BIC[210] Si metasurfaces have demonstrated enhancement of SHG and SFG of several orders of magnitude at CW excitation compared to the bare 2D material. Note that given the centrosymmetric structure of Si, its second-order emission is negligible compared to that of GaSe, which possesses a noncentrosymmetric ε-type stacking of the constituting layers. Alternatively, applying a DC bias field to a third-order nonlinear material can also induce a second-order nonlinear susceptibility, enabling electric-field-induced SHG (EFISHG). Electrically tunable dielectric metasurfaces for enhanced and controlled nonlinear optical emission have been recently studied theoretically[211] and also experimentally in bulk GaAs[212] and Si metasurfaces.[213]

Research in high-harmonic generation and wave mixing phenomena started to develop only less than 5 years ago and have the added experimental complexity of multiple beam excitation or extended working spectral ranges. The volume of reported investigations in these areas is significantly smaller compared to SHG or THG and should gain more momentum in the coming years. Mode-matching engineering for increasing wave-mixing conversion efficiencies is still at a very early stage and remains to be explored in depth. Of particular interest in HHG at the moment is the fundamental comprehension of the physics behind the nonperturbative nonlinear regime.

Full $0-2\pi$ phase and amplitude control at the SH and TH emitted wavelengths has been successfully proven in a variety of dielectric metasurfaces, with demonstrated examples in beam steering, holography, optical vortex generation, lensing, and imaging. A crucial issue in these applications is, however, beyond conversion efficiency, that of the intrinsically small operation bandwidth of the optical resonances involved, where their spectral widths generally do not extend more than ∼100 nm in the visible to near-infrared range. Future research could find inspiration in its linear regime counterpart,[177] using alternating regions of space working in different spectral ranges, or multiple meta-atoms per unit cell resonating at various wavelengths, or differently tuned stacked metasurfaces, and so on.

All-optically time-controlled resonators have also been analyzed in this Review, however, limited only to the case of sub-100 fs Kerr-type nonlinearities. Integrating 2D materials with nanostructured dielectrics may also help achieve higher modulation depths at lower pump energies,[214,215] as sub-20 fs differential reflectivity modulations of a few percent have already been demonstrated in 2D hybrid perovskite thin layers.[215] Most of the research effort in this field is, however, now put on the more efficient free-carrier effects for picosecond modulation at the incident or emitted wavelengths.[216−218]

Finally, I have revised the few reported experimental works exploring topological nanophotonics through nonlinear frequency conversion in 1D and 2D Si dielectric arrays, where 0D and 1D topologically protected edge states have been shown to produce enhanced and localized THG emission. The observed effects were found to be robust against a significant degree of added structural disorder due to their topological nature, which could have important implications in the stability of nanophotonic devices against fabrication imperfections and wearing over time. Next steps could involve investigating new geometrical symmetries as well as other materials, gaining more insight in high-order topological effects, and also combining topology with quantum photonics, where nonlinear nanostructured dielectrics also hold great promise.[10,219−221] In the past two years, single nanoantennas[219] and metasurfaces[10] have been reported for the first time for spontaneous parametric down-conversion (SPDC). SPDC is a second-order process where a pump photon of frequency ω_p splits into two entangled photons with lower frequencies ω_s (signal) and ω_i (idler), where $\omega_s + \omega_i = \omega_p$. Nanoscale single- and multiphoton quantum sources are one of the main building blocks required for quantum information processing compact devices.

Nonlinear dielectric nanoantennas and metasurfaces show enormous potential for real-world applications, with possible on-chip all-optical capabilities including frequency conversion and parametric amplification, nonlinear optical sensing, spatial modulation of light, and active switching. Integrated photonic circuitries based on optical nonlinearities (both classical and quantum) are expected to overcome heating and speed limitations of conventional electronics, with operational

https://doi.org/10.1021/acsphotonics.1c01356
ACS Photonics XXXX, XXX, XXX−XXX

bandwidths reaching the THz range. The subject should still see rapid growth in the coming years, pushed by the permanent evolution in the understanding of the underlying physics, accompanied by advancements in design engineering and combination with other materials, as well as progress in nanofabrication technologies.

AUTHOR INFORMATION

Corresponding Author

Gustavo Grinblat − *Departamento de Física, FCEN, IFIBA-CONICET, Universidad de Buenos Aires, C1428EGA Buenos Aires, Argentina;* orcid.org/0000-0002-1637-9524; Email: grinblat@df.uba.ar

Complete contact information is available at: https://pubs.acs.org/10.1021/acsphotonics.1c01356

Notes

The author declares no competing financial interest.

ACKNOWLEDGMENTS

The author acknowledges funding from the Argentine Agency of Research and Technology, Project PICT 2019-01886, and from the University of Buenos Aires, Project UBACyT 20020190200296BA.

REFERENCES

(1) Mesch, M.; Metzger, B.; Hentschel, M.; Giessen, H. Nonlinear Plasmonic Sensing. *Nano Lett.* **2016**, *16* (5), 3155−9.

(2) Regmi, R.; Berthelot, J.; Winkler, P. M.; Mivelle, M.; Proust, J.; Bedu, F.; Ozerov, I.; Begou, T.; Lumeau, J.; Rigneault, H.; Garcia-Parajo, M. F.; Bidault, S.; Wenger, J.; Bonod, N. All-Dielectric Silicon Nanogap Antennas To Enhance the Fluorescence of Single Molecules. *Nano Lett.* **2016**, *16* (8), 5143−51.

(3) Verma, M. S.; Chandra, M. Nonlinear Plasmonic Sensing for Label-Free and Selective Detection of Mercury at Picomolar Level. *ACS Sens* **2020**, *5* (3), 645−649.

(4) Kravtsov, V.; Ulbricht, R.; Atkin, J. M.; Raschke, M. B. Plasmonic nanofocused four-wave mixing for femtosecond near-field imaging. *Nat. Nanotechnol.* **2016**, *11* (5), 459−64.

(5) Deka, G.; Sun, C.-K.; Fujita, K.; Chu, S.-W. Nonlinear plasmonic imaging techniques and their biological applications. *Nanophotonics* **2017**, *6* (1), 31−49.

(6) Frischwasser, K.; Cohen, K.; Kher-Alden, J.; Dolev, S.; Tsesses, S.; Bartal, G. Real-time sub-wavelength imaging of surface waves with nonlinear near-field optical microscopy. *Nat. Photonics* **2021**, *15* (6), 442−448.

(7) Gao, Y.; Fan, Y.; Wang, Y.; Yang, W.; Song, Q.; Xiao, S. Nonlinear Holographic All-Dielectric Metasurfaces. *Nano Lett.* **2018**, *18* (12), 8054−8061.

(8) Reineke, B.; Sain, B.; Zhao, R.; Carletti, L.; Liu, B.; Huang, L.; De Angelis, C.; Zentgraf, T. Silicon Metasurfaces for Third Harmonic Geometric Phase Manipulation and Multiplexed Holography. *Nano Lett.* **2019**, *19* (9), 6585−6591.

(9) Ye, W.; Zeuner, F.; Li, X.; Reineke, B.; He, S.; Qiu, C. W.; Liu, J.; Wang, Y.; Zhang, S.; Zentgraf, T. Spin and wavelength multiplexed nonlinear metasurface holography. *Nat. Commun.* **2016**, *7*, 11930.

(10) Santiago-Cruz, T.; Fedotova, A.; Sultanov, V.; Weissflog, M. A.; Arslan, D.; Younesi, M.; Pertsch, T.; Staude, I.; Setzpfandt, F.; Chekhova, M. Photon Pairs from Resonant Metasurfaces. *Nano Lett.* **2021**, *21* (10), 4423−4429.

(11) Shcherbakov, M. R.; Vabishchevich, P. P.; Shorokhov, A. S.; Chong, K. E.; Choi, D. Y.; Staude, I.; Miroshnichenko, A. E.; Neshev, D. N.; Fedyanin, A. A.; Kivshar, Y. S. Ultrafast All-Optical Switching with Magnetic Resonances in Nonlinear Dielectric Nanostructures. *Nano Lett.* **2015**, *15* (10), 6985−90.

(12) Grinblat, G.; Zhang, H.; Nielsen, M. P.; Krivitsky, L.; Berté, R.; Li, Y.; Tilmann, B.; Cortés, E.; Oulton, R. F.; Kuznetsov, A. I.; Maier, S. A. Efficient ultrafast all-optical modulation in a nonlinear crystalline gallium phosphide nanodisk at the anapole excitation. *Science Advances* **2020**, *6*, abb3123.

(13) Seyler, K. L.; Schaibley, J. R.; Gong, P.; Rivera, P.; Jones, A. M.; Wu, S.; Yan, J.; Mandrus, D. G.; Yao, W.; Xu, X. Electrical control of second-harmonic generation in a WSe2 monolayer transistor. *Nat. Nanotechnol.* **2015**, *10* (5), 407−11.

(14) Minzioni, P.; Lacava, C.; Tanabe, T.; Dong, J.; Hu, X.; Csaba, G.; Porod, W.; Singh, G.; Willner, A. E.; Almaiman, A.; Torres-Company, V.; Schröder, J.; Peacock, A. C.; Strain, M. J.; Parmigiani, F.; Contestabile, G.; Marpaung, D.; Liu, Z.; Bowers, J. E.; Chang, L.; Fabbri, S.; Ramos Vázquez, M.; Bharadwaj, V.; Eaton, S. M.; Lodahl, P.; Zhang, X.; Eggleton, B. J.; Munro, W. J.; Nemoto, K.; Morin, O.; Laurat, J.; Nunn, J. Roadmap on all-optical processing. *J. Opt.* **2019**, *21* (6), 063001.

(15) Rashed, A. N. Z.; Mohammed, A. E.-N. A.; Zaky, W. F.; Amiri, I. S.; Yupapin, P. The switching of optoelectronics to full optical computing operations based on nonlinear metamaterials. *Results Phys.* **2019**, *13*, 102152.

(16) Giannini, V.; Fernandez-Dominguez, A. I.; Heck, S. C.; Maier, S. A. Plasmonic nanoantennas: fundamentals and their use in controlling the radiative properties of nanoemitters. *Chem. Rev.* **2011**, *111* (6), 3888−912.

(17) Zhang, Y.; Grady, N. K.; Ayala-Orozco, C.; Halas, N. J. Three-dimensional nanostructures as highly efficient generators of second harmonic light. *Nano Lett.* **2011**, *11* (12), 5519−23.

(18) Aouani, H.; Navarro-Cia, M.; Rahmani, M.; Sidiropoulos, T. P.; Hong, M.; Oulton, R. F.; Maier, S. A. Multiresonant broadband optical antennas as efficient tunable nanosources of second harmonic light. *Nano Lett.* **2012**, *12* (9), 4997−5002.

(19) Thyagarajan, K.; Butet, J.; Martin, O. J. Augmenting second harmonic generation using Fano resonances in plasmonic systems. *Nano Lett.* **2013**, *13* (4), 1847−51.

(20) Metzger, B.; Schumacher, T.; Hentschel, M.; Lippitz, M.; Giessen, H. Third Harmonic Mechanism in Complex Plasmonic Fano Structures. *ACS Photonics* **2014**, *1* (6), 471−476.

(21) Schlickriede, C.; Waterman, N.; Reineke, B.; Georgi, P.; Li, G.; Zhang, S.; Zentgraf, T. Imaging through Nonlinear Metalens Using Second Harmonic Generation. *Adv. Mater.* **2018**, *30* (8), 1703843.

(22) Aouani, H.; Rahmani, M.; Navarro-Cia, M.; Maier, S. A. Third-harmonic-upconversion enhancement from a single semiconductor nanoparticle coupled to a plasmonic antenna. *Nat. Nanotechnol.* **2014**, *9* (4), 290−4.

(23) Grinblat, G.; Rahmani, M.; Cortes, E.; Caldarola, M.; Comedi, D.; Maier, S. A.; Bragas, A. V. High-efficiency second harmonic generation from a single hybrid ZnO nanowire/Au plasmonic nano-oligomer. *Nano Lett.* **2014**, *14* (11), 6660−5.

(24) Shcherbakov, M. R.; Neshev, D. N.; Hopkins, B.; Shorokhov, A. S.; Staude, I.; Melik-Gaykazyan, E. V.; Decker, M.; Ezhov, A. A.; Miroshnichenko, A. E.; Brener, I.; Fedyanin, A. A.; Kivshar, Y. S. Enhanced third-harmonic generation in silicon nanoparticles driven by magnetic response. *Nano Lett.* **2014**, *14* (11), 6488−92.

(25) Caldarola, M.; Albella, P.; Cortes, E.; Rahmani, M.; Roschuk, T.; Grinblat, G.; Oulton, R. F.; Bragas, A. V.; Maier, S. A. Non-plasmonic nanoantennas for surface enhanced spectroscopies with ultra-low heat conversion. *Nat. Commun.* **2015**, *6*, 7915.

(26) Kuznetsov, A. I.; Miroshnichenko, A. E.; Brongersma, M. L.; Kivshar, Y. S.; Luk'yanchuk, B. Optically resonant dielectric nanostructures. *Science* **2016**, *354* (6314), aag2472.

(27) Kuznetsov, A. I.; Miroshnichenko, A. E.; Fu, Y. H.; Zhang, J.; Luk'yanchuk, B. Magnetic light. *Sci. Rep.* **2012**, *2*, 492.

(28) Boyd, R. W. *Nonlinear Opt.*, 3rd ed.; Academic Press, 2008.

(29) Liu, S.; Vabishchevich, P. P.; Vaskin, A.; Reno, J. L.; Keeler, G. A.; Sinclair, M. B.; Staude, I.; Brener, I. An all-dielectric metasurface as a broadband optical frequency mixer. *Nat. Commun.* **2018**, *9* (1), 2507.

(30) Xu, L.; Saerens, G.; Timofeeva, M.; Smirnova, D. A.; Volkovskaya, I.; Lysevych, M.; Camacho-Morales, R.; Cai, M.; Zangeneh Kamali, K.; Huang, L.; Karouta, F.; Tan, H. H.; Jagadish, C.; Miroshnichenko, A. E.; Grange, R.; Neshev, D. N.; Rahmani, M. Forward and Backward Switching of Nonlinear Unidirectional Emission from GaAs Nanoantennas. *ACS Nano* **2020**, *14* (2), 1379−1389.
(31) Shcherbakov, M. R.; Zhang, H.; Tripepi, M.; Sartorello, G.; Talisa, N.; AlShafey, A.; Fan, Z.; Twardowski, J.; Krivitsky, L. A.; Kuznetsov, A. I.; Chowdhury, E.; Shvets, G. Generation of even and odd high harmonics in resonant metasurfaces using single and multiple ultra-intense laser pulses. *Nat. Commun.* **2021**, *12* (1), 4185.
(32) Wang, L.; Kruk, S.; Koshelev, K.; Kravchenko, I.; Luther-Davies, B.; Kivshar, Y. Nonlinear Wavefront Control with All-Dielectric Metasurfaces. *Nano Lett.* **2018**, *18* (6), 3978−3984.
(33) Schlickriede, C.; Kruk, S. S.; Wang, L.; Sain, B.; Kivshar, Y.; Zentgraf, T. Nonlinear Imaging with All-Dielectric Metasurfaces. *Nano Lett.* **2020**, *20* (6), 4370−4376.
(34) Kruk, S.; Poddubny, A.; Smirnova, D.; Wang, L.; Slobozhanyuk, A.; Shorokhov, A.; Kravchenko, I.; Luther-Davies, B.; Kivshar, Y. Nonlinear light generation in topological nanostructures. *Nat. Nanotechnol.* **2019**, *14* (2), 126−130.
(35) Liu, S.; Sinclair, M. B.; Saravi, S.; Keeler, G. A.; Yang, Y.; Reno, J.; Peake, G. M.; Setzpfandt, F.; Staude, I.; Pertsch, T.; Brener, I. Resonantly Enhanced Second-Harmonic Generation Using III-V Semiconductor All-Dielectric Metasurfaces. *Nano Lett.* **2016**, *16* (9), 5426−32.
(36) Löchner, F. J. F.; Fedotova, A. N.; Liu, S.; Keeler, G. A.; Peake, G. M.; Saravi, S.; Shcherbakov, M. R.; Burger, S.; Fedyanin, A. A.; Brener, I.; Pertsch, T.; Setzpfandt, F.; Staude, I. Polarization-Dependent Second Harmonic Diffraction from Resonant GaAs Metasurfaces. *ACS Photonics* **2018**, *5* (5), 1786−1793.
(37) Vabishchevich, P. P.; Liu, S.; Sinclair, M. B.; Keeler, G. A.; Peake, G. M.; Brener, I. Enhanced Second-Harmonic Generation Using Broken Symmetry III−V Semiconductor Fano Metasurfaces. *ACS Photonics* **2018**, *5* (5), 1685−1690.
(38) Saerens, G.; Tang, I.; Petrov, M. I.; Frizyuk, K.; Renaut, C.; Timpu, F.; Reig Escalé, M.; Shtrom, I.; Bouravleuv, A.; Cirlin, G.; Grange, R.; Timofeeva, M. Engineering of the Second-Harmonic Emission Directionality with III−V Semiconductor Rod Nanoantennas. *Laser Photonics Rev.* **2020**, *14* (9), 2000028.
(39) Sautter, J. D.; Xu, L.; Miroshnichenko, A. E.; Lysevych, M.; Volkovskaya, I.; Smirnova, D. A.; Camacho-Morales, R.; Zangeneh Kamali, K.; Karouta, F.; Vora, K.; Tan, H. H.; Kauranen, M.; Staude, I.; Jagadish, C.; Neshev, D. N.; Rahmani, M. Tailoring Second-Harmonic Emission from (111)-GaAs Nanoantennas. *Nano Lett.* **2019**, *19* (6), 3905−3911.
(40) Timofeeva, M.; Lang, L.; Timpu, F.; Renaut, C.; Bouravleuv, A.; Shtrom, I.; Cirlin, G.; Grange, R. Anapoles in Free-Standing III−V Nanodisks Enhancing Second-Harmonic Generation. *Nano Lett.* **2018**, *18* (6), 3695−3702.
(41) Gili, V. F.; Carletti, L.; Locatelli, A.; Rocco, D.; Finazzi, M.; Ghirardini, L.; Favero, I.; Gomez, C.; Lemaitre, A.; Celebrano, M.; De Angelis, C.; Leo, G. Monolithic AlGaAs second-harmonic nanoantennas. *Opt. Express* **2016**, *24* (14), 15965−71.
(42) Camacho-Morales, R.; Rahmani, M.; Kruk, S.; Wang, L.; Xu, L.; Smirnova, D. A.; Solntsev, A. S.; Miroshnichenko, A.; Tan, H. H.; Karouta, F.; Naureen, S.; Vora, K.; Carletti, L.; De Angelis, C.; Jagadish, C.; Kivshar, Y. S.; Neshev, D. N. Nonlinear Generation of Vector Beams From AlGaAs Nanoantennas. *Nano Lett.* **2016**, *16* (11), 7191−7197.
(43) Ghirardini, L.; Carletti, L.; Gili, V.; Pellegrini, G.; Duo, L.; Finazzi, M.; Rocco, D.; Locatelli, A.; De Angelis, C.; Favero, I.; Ravaro, M.; Leo, G.; Lemaitre, A.; Celebrano, M. Polarization properties of second-harmonic generation in AlGaAs optical nanoantennas. *Opt. Lett.* **2017**, *42* (3), 559−562.
(44) Carletti, L.; Rocco, D.; Locatelli, A.; De Angelis, C.; Gili, V. F.; Ravaro, M.; Favero, I.; Leo, G.; Finazzi, M.; Ghirardini, L.; Celebrano, M.; Marino, G.; Zayats, A. V. Controlling second-harmonic generation at the nanoscale with monolithic AlGaAs-on-AlOx antennas. *Nanotechnology* **2017**, *28* (11), 114005.
(45) Kruk, S. S.; Camacho-Morales, R.; Xu, L.; Rahmani, M.; Smirnova, D. A.; Wang, L.; Tan, H. H.; Jagadish, C.; Neshev, D. N.; Kivshar, Y. S. Nonlinear Optical Magnetism Revealed by Second-Harmonic Generation in Nanoantennas. *Nano Lett.* **2017**, *17* (6), 3914−3918.
(46) Gili, V. F.; Carletti, L.; Chouchane, F.; Wang, G.; Ricolleau, C.; Rocco, D.; Lemaître, A.; Favero, I.; Ghirardini, L.; Finazzi, M.; Celebrano, M.; Angelis, C. D.; Leo, G. Role of the substrate in monolithic AlGaAs nonlinear nanoantennas. *Nanophotonics* **2017**, *7* (2), 517−521.
(47) Rocco, D.; Gili, V. F.; Ghirardini, L.; Carletti, L.; Favero, I.; Locatelli, A.; Marino, G.; Neshev, D. N.; Celebrano, M.; Finazzi, M.; Leo, G.; De Angelis, C. Tuning the second-harmonic generation in AlGaAs nanodimers via non-radiative state optimization. *Photonics Res.* **2018**, *6* (5), B6−B12.
(48) Melik-Gaykazyan, E. V.; Koshelev, K. L.; Choi, J. H.; Kruk, S. S.; Park, H. G.; Fedyanin, A. A.; Kivshar, Y. S. Enhanced Second-Harmonic Generation with Structured Light in AlGaAs Nanoparticles Governed by Magnetic Response. *JETP Lett.* **2019**, *109* (2), 131−135.
(49) Gigli, C.; Marino, G.; Suffit, S.; Patriarche, G.; Beaudoin, G.; Pantzas, K.; Sagnes, I.; Favero, I.; Leo, G. Polarization- and diffraction-controlled second-harmonic generation from semiconductor metasurfaces. *J. Opt. Soc. Am. B* **2019**, *36* (7), E55−E64.
(50) Camacho-Morales, R.; Bautista, G.; Zang, X.; Xu, L.; Turquet, L.; Miroshnichenko, A.; Tan, H. H.; Lamprianidis, A.; Rahmani, M.; Jagadish, C.; Neshev, D. N.; Kauranen, M. Resonant harmonic generation in AlGaAs nanoantennas probed by cylindrical vector beams. *Nanoscale* **2019**, *11* (4), 1745−1753.
(51) Koshelev, K.; Kruk, S.; Melik-Gaykazyan, E.; Choi, J.-H.; Bogdanov, A.; Park, H.-G.; Kivshar, Y. Subwavelength dielectric resonators for nonlinear nanophotonics. *Science* **2020**, *367*, 288−292.
(52) Carletti, L.; Marino, G.; Ghirardini, L.; Gili, V. F.; Rocco, D.; Favero, I.; Locatelli, A.; Zayats, A. V.; Celebrano, M.; Finazzi, M.; Leo, G.; De Angelis, C.; Neshev, D. N. Nonlinear Goniometry by Second-Harmonic Generation in AlGaAs Nanoantennas. *ACS Photonics* **2018**, *5* (11), 4386−4392.
(53) Ghirardini, L.; Marino, G.; Gili, V. F.; Favero, I.; Rocco, D.; Carletti, L.; Locatelli, A.; De Angelis, C.; Finazzi, M.; Celebrano, M.; Neshev, D. N.; Leo, G. Shaping the Nonlinear Emission Pattern of a Dielectric Nanoantenna by Integrated Holographic Gratings. *Nano Lett.* **2018**, *18* (11), 6750−6755.
(54) Marino, G.; Gigli, C.; Rocco, D.; Lemaître, A.; Favero, I.; De Angelis, C.; Leo, G. Zero-Order Second Harmonic Generation from AlGaAs-on-Insulator Metasurfaces. *ACS Photonics* **2019**, *6* (5), 1226−1231.
(55) Gili, V. F.; Ghirardini, L.; Rocco, D.; Marino, G.; Favero, I.; Roland, I.; Pellegrini, G.; Duo, L.; Finazzi, M.; Carletti, L.; Locatelli, A.; Lemaitre, A.; Neshev, D.; De Angelis, C.; Leo, G.; Celebrano, M. Metal-dielectric hybrid nanoantennas for efficient frequency conversion at the anapole mode. *Beilstein J. Nanotechnol.* **2018**, *9*, 2306−2314.
(56) Marino, G.; Rocco, D.; Gigli, C.; Beaudoin, G.; Pantzas, K.; Suffit, S.; Filloux, P.; Sagnes, I.; Leo, G.; De Angelis, C. Harmonic generation with multi-layer dielectric metasurfaces. *Nanophotonics* **2021**, *10* (7), 1837−1843.
(57) Cambiasso, J.; Grinblat, G.; Li, Y.; Rakovich, A.; Cortes, E.; Maier, S. A. Bridging the Gap between Dielectric Nanophotonics and the Visible Regime with Effectively Lossless Gallium Phosphide Antennas. *Nano Lett.* **2017**, *17* (2), 1219−1225.
(58) Anthur, A. P.; Zhang, H.; Paniagua-Dominguez, R.; Kalashnikov, D. A.; Ha, S. T.; Mass, T. W. W.; Kuznetsov, A. I.; Krivitsky, L. Continuous Wave Second Harmonic Generation Enabled by Quasi-Bound-States in the Continuum on Gallium Phosphide Metasurfaces. *Nano Lett.* **2020**, *20* (12), 8745−8751.
(59) Khmelevskaia, D.; Markina, D. I.; Fedorov, V. V.; Ermolaev, G. A.; Arsenin, A. V.; Volkov, V. S.; Goltaev, A. S.; Zadiranov, Y. M.; Tzibizov, I. A.; Pushkarev, A. P.; Samusev, A. K.; Shcherbakov, A. A.;

https://doi.org/10.1021/acsphotonics.1c01356
ACS Photonics XXXX, XXX, XXX−XXX

Belov, P. A.; Mukhin, I. S.; Makarov, S. V. Directly grown crystalline gallium phosphide on sapphire for nonlinear all-dielectric nanophotonics. *Appl. Phys. Lett.* **2021**, *118* (20), 201101.
(60) Ma, C. R.; Yan, J. H.; Liu, P.; Wei, Y. M.; Yang, G. W. Second harmonic generation from an individual all-dielectric nanoparticle: resonance enhancement versus particle geometry. *J. Mater. Chem. C* **2016**, *4* (25), 6063−6069.
(61) Golla, C.; Weber, N.; Meier, C. Zinc oxide based dielectric nanoantennas for efficient nonlinear frequency conversion. *J. Appl. Phys.* **2019**, *125* (7), 073103.
(62) Bahng, J. H.; Jahani, S.; Montjoy, D. G.; Yao, T.; Kotov, N.; Marandi, A. Mie Resonance Engineering in Meta-Shell Supraparticles for Nanoscale Nonlinear Optics. *ACS Nano* **2020**, *14*, 17203−17212.
(63) Semmlinger, M.; Tseng, M. L.; Yang, J.; Zhang, M.; Zhang, C.; Tsai, W. Y.; Tsai, D. P.; Nordlander, P.; Halas, N. J. Vacuum Ultraviolet Light-Generating Metasurface. *Nano Lett.* **2018**, *18* (9), 5738−5743.
(64) Ma, C.; Yan, J.; Wei, Y.; Liu, P.; Yang, G. Enhanced second harmonic generation in individual barium titanate nanoparticles driven by Mie resonances. *J. Mater. Chem. C* **2017**, *5* (19), 4810−4819.
(65) Timpu, F.; Reig Escalé, M.; Timofeeva, M.; Strkalj, N.; Trassin, M.; Fiebig, M.; Grange, R. Enhanced Nonlinear Yield from Barium Titanate Metasurface Down to the Near Ultraviolet. *Adv. Opt. Mater.* **2019**, *7* (22), 1900936.
(66) Timpu, F.; Sergeyev, A.; Hendricks, N. R.; Grange, R. Second-Harmonic Enhancement with Mie Resonances in Perovskite Nanoparticles. *ACS Photonics* **2017**, *4* (1), 76−84.
(67) Savo, R.; Morandi, A.; Müller, J. S.; Kaufmann, F.; Timpu, F.; Reig Escalé, M.; Zanini, M.; Isa, L.; Grange, R. Broadband Mie driven random quasi-phase-matching. *Nat. Photonics* **2020**, *14* (12), 740−747.
(68) Timpu, F.; Sendra, J.; Renaut, C.; Lang, L.; Timofeeva, M.; Buscaglia, M. T.; Buscaglia, V.; Grange, R. Lithium Niobate Nanocubes as Linear and Nonlinear Ultraviolet Mie Resonators. *ACS Photonics* **2019**, *6* (2), 545−552.
(69) Fedotova, A.; Younesi, M.; Sautter, J.; Vaskin, A.; Lochner, F. J. F.; Steinert, M.; Geiss, R.; Pertsch, T.; Staude, I.; Setzpfandt, F. Second-Harmonic Generation in Resonant Nonlinear Metasurfaces Based on Lithium Niobate. *Nano Lett.* **2020**, *20* (12), 8608−8614.
(70) Ma, J.; Xie, F.; Chen, W.; Chen, J.; Wu, W.; Liu, W.; Chen, Y.; Cai, W.; Ren, M.; Xu, J. Nonlinear Lithium Niobate Metasurfaces for Second Harmonic Generation. *Laser Photonics Rev.* **2021**, *15*, 2000521.
(71) Carletti, L.; Zilli, A.; Moia, F.; Toma, A.; Finazzi, M.; De Angelis, C.; Neshev, D. N.; Celebrano, M. Steering and Encoding the Polarization of the Second Harmonic in the Visible with a Monolithic LiNbO3Metasurface. *ACS Photonics* **2021**, *8* (3), 731−737.
(72) Wang, J.; Liu, Z.; Xiang, J.; Chen, B.; Wei, Y.; Liu, W.; Xu, Y.; Lan, S.; Liu, J. Ultraviolet second harmonic generation from Mie-resonant lithium niobate nanospheres. *Nanophotonics* **2021**, *0* (0), na.
(73) Makarov, S. V.; Petrov, M. I.; Zywietz, U.; Milichko, V.; Zuev, D.; Lopanitsyna, N.; Kuksin, A.; Mukhin, I.; Zograf, G.; Ubyivovk, E.; Smirnova, D. A.; Starikov, S.; Chichkov, B. N.; Kivshar, Y. S. Efficient Second-Harmonic Generation in Nanocrystalline Silicon Nanoparticles. *Nano Lett.* **2017**, *17* (5), 3047−3053.
(74) Bar-David, J.; Levy, U. Nonlinear Diffraction in Asymmetric Dielectric Metasurfaces. *Nano Lett.* **2019**, *19* (2), 1044−1051.
(75) Tilmann, B.; Grinblat, G.; Berte, R.; Ozcan, M.; Kunzelmann, V. F.; Nickel, B.; Sharp, I. D.; Cortes, E.; Maier, S. A.; Li, Y. Nanostructured amorphous gallium phosphide on silica for nonlinear and ultrafast nanophotonics. *Nanoscale Horiz* **2020**, *5* (11), 1500−1508.
(76) Ma, C. R.; Yan, J. H.; Wei, Y. M.; Yang, G. W. Second harmonic generation from an individual amorphous selenium nanosphere. *Nanotechnology* **2016**, *27* (42), 425206.
(77) Das Gupta, T.; Martin-Monier, L.; Butet, J.; Yang, K.-Y.; Leber, A.; Dong, C.; Nguyen-Dang, T.; Yan, W.; Martin, O. J. F.; Sorin, F. Second harmonic generation from Chalcogenide metasurfaces via mode coupling engineering. *Nanophotonics* **2021**, *10*, 3465.
(78) Papatryfonos, K.; Angelova, T.; Brimont, A.; Reid, B.; Guldin, S.; Smith, P. R.; Tang, M.; Li, K.; Seeds, A. J.; Liu, H.; Selviah, D. R. Refractive indices of MBE-grown AlxGa(1−x)As ternary alloys in the transparent wavelength region. *AIP Adv.* **2021**, *11* (2), 025327.
(79) Kachare, A. H.; Spitzer, W. G.; Fredrickson, J. E. Refractive index of ion-implanted GaAs. *J. Appl. Phys.* **1976**, *47* (9), 4209−4212.
(80) Shoji, I.; Kondo, T.; Kitamoto, A.; Shirane, M.; Ito, R. Absolute scale of second-order nonlinear-optical coefficients. *J. Opt. Soc. Am. B* **1997**, *14*, 2268−2293.
(81) Adachi, S. GaAs, AlAs, and AlxGa1−xAs: Material parameters for use in research and device applications. *J. Appl. Phys.* **1985**, *58* (3), R1−R29.
(82) Ohashi, M.; Kondo, T.; Ito, R.; Fukatsu, S.; Shiraki, Y.; Kumata, K.; Kano, S. S. Determination of quadratic nonlinear optical coefficient of AlxGa1−xAs system by the method of reflected second harmonics. *J. Appl. Phys.* **1993**, *74* (1), 596−601.
(83) Jellison, G.E. Optical functions of GaAs, GaP, and Ge determined by two-channel polarization modulation ellipsometry. *Opt. Mater.* **1992**, *1*, 151−160.
(84) Bond, W. L. Measurement of the Refractive Indices of Several Crystals. *J. Appl. Phys.* **1965**, *36* (5), 1674−1677.
(85) Bergstrom, L.; Meurk, A.; Arwin, H.; Rowcliffe, D. J. Estimation of Hamaker Constants of Ceramic Materials from Optical Data Using Lifshitz Theory. *J. Am. Ceram. Soc.* **1996**, *79*, 339−348.
(86) Wang, G.; Wong, G. K. L.; Ketterson, J. B. Redetermination of second-order susceptibility of zinc oxide single crystals. *Appl. Opt.* **2001**, *40*, 5436−5438.
(87) Philipp, H. R. T. In *Silicon Carbide - A High Temperature Semiconductor*; O'Connor, J. R., Smiltens, J., Eds.; Pergamon Press, 1960.
(88) In *Handbook of Optical Constants of Solids*; Palik, E. D., Ed.; Academic Press: Burlington, 1997.
(89) Niedermeier, S.; Schillinger, H.; Sauerbrey, R.; Adolph, B.; Bechstedt, F. Second-harmonic generation in silicon carbide polytypes. *Appl. Phys. Lett.* **1999**, *75* (5), 618−620.
(90) Schunemann, P. G.; Pollak, T. M.; Yang, Y.; Teng, Y.-Y.; Wong, C. Effects of feed material and annealing atmosphere on the photorefractive properties of Barium Titanate Crystals. *J. Opt. Soc. Am. B* **1988**, *5*, 1702−1710.
(91) Zelmon, D. E.; Small, D. L.; Schunemann, P. Refractive Index Measurements of Barium Titanate From. 4 to 5.0 Microns and Implications for Periodically Poled Frequency Conversion Devices. *Mater. Res. Soc. Symp. Proc.* **1997**, *484*, 537−541.
(92) Nikogosyan, D. N. *Nonlinear Optical Crystals: A Complete Survey*; Springer, 2005.
(93) Yan, X.; Tian, T.; Wang, M.; Shen, H.; Zhou, D.; Zhang, Y.; Xu, J. High Homogeneity of Magnesium Doped LiNbO3 Crystals Grown by Bridgman Method. *Crystals* **2020**, *10* (2), 71.
(94) Kozlova, N. S.; Shayapov, V. R.; Zabelina, E. V.; Kozlova, A. P.; Zhukov, R. N.; Kiselev, D. A.; Malinkovich, M. D.; Voronova, M. I. Spectrophotometric determination of optical parameters of lithium niobate films. *Modern Electronic Materials* **2017**, *3* (3), 122−126.
(95) Zelmon, D. E.; Small, D. L.; Jundt, D. Infrared corrected Sellmeier coefficients for congruently grown lithium niobate and 5 mol. % magnesium oxide−doped lithium niobate. *J. Opt. Soc. Am. B* **1997**, *14*, 3319−3322.
(96) Roberts, D. A. Simplified Characterization of Uniaxial and Biaxial Nonlinear Optical Crystals: A Plea for Standardization of Nomenclature and Conventions. *IEEE J. Quantum Electron.* **1992**, *28*, 2057−2074.
(97) Rodriguez, A.; Soljacic, M.; Joannopoulos, J. D.; Johnson, S. G. $\chi(2)$ and $\chi(3)$ harmonic generation at a critical power in inhomogeneous doublyresonant cavities. *Opt. Express* **2007**, *15*, 7303−7318.
(98) Lin, Z.; Liang, X.; Lončar, M.; Johnson, S. G.; Rodriguez, A. W. Cavity-enhanced second-harmonic generation via nonlinear-overlap optimization. *Optica* **2016**, *3* (3), 233−238.

https://doi.org/10.1021/acsphotonics.1c01356
ACS Photonics XXXX, XXX, XXX−XXX

(99) Noor, A.; Damodaran, A. R.; Lee, I. H.; Maier, S. A.; Oh, S. H.; Ciraci, C. Mode-Matching Enhancement of Second-Harmonic Generation with Plasmonic Nanopatch Antennas. *ACS Photonics* **2020**, *7* (12), 3333−3340.
(100) Carletti, L.; Locatelli, A.; Stepanenko, O.; Leo, G.; De Angelis, C. Enhanced second-harmonic generation from magnetic resonance in AlGaAs nanoantennas. *Opt. Express* **2015**, *23* (20), 26544−50.
(101) Celebrano, M.; Wu, X.; Baselli, M.; Grossmann, S.; Biagioni, P.; Locatelli, A.; De Angelis, C.; Cerullo, G.; Osellame, R.; Hecht, B.; Duo, L.; Ciccacci, F.; Finazzi, M. Mode matching in multiresonant plasmonic nanoantennas for enhanced second harmonic generation. *Nat. Nanotechnol.* **2015**, *10* (5), 412−7.
(102) Hurlbut, W. C.; Lee, Y.-S.; Vodopyanov, K. L.; Kuo, P. S.; Fejer, M. M. Multiphoton absorption and nonlinear refraction of GaAs in the mid-infrared. *Opt. Lett.* **2007**, *32*, 668−670.
(103) Rocco, D.; Vincenti, M.; De Angelis, C. Boosting Second Harmonic Radiation from AlGaAs Nanoantennas with Epsilon-Near-Zero Materials. *Appl. Sci.* **2018**, *8* (11), 2212.
(104) Rocco, D.; De Angelis, C.; de Ceglia, D.; Carletti, L.; Scalora, M.; Vincenti, M.A. Dielectric nanoantennas on epsilon-near-zero substrates: Impact of losses on second order nonlinear processes. *Opt. Commun.* **2020**, *456*, 124570.
(105) Hsu, C. W.; Zhen, B.; Stone, A. D.; Joannopoulos, J. D.; Soljačić, M. Bound states in the continuum. *Nature Reviews Materials* **2016**, *1*, 16048.
(106) Liu, Z.; Xu, Y.; Lin, Y.; Xiang, J.; Feng, T.; Cao, Q.; Li, J.; Lan, S.; Liu, J. High-Q Quasibound States in the Continuum for Nonlinear Metasurfaces. *Phys. Rev. Lett.* **2019**, *123* (25), 253901.
(107) Rybin, M. V.; Koshelev, K. L.; Sadrieva, Z. F.; Samusev, K. B.; Bogdanov, A. A.; Limonov, M. F.; Kivshar, Y. S. High-Q Supercavity Modes in Subwavelength Dielectric Resonators. *Phys. Rev. Lett.* **2017**, *119* (24), 243901.
(108) Volkovskaya, I.; Xu, L.; Huang, L.; Smirnov, A. I.; Miroshnichenko, A. E.; Smirnova, D. Multipolar second-harmonic generation from high-Q quasi-BIC states in subwavelength resonators. *Nanophotonics* **2020**, *9* (12), 3953−3963.
(109) Koshelev, K.; Lepeshov, S.; Liu, M.; Bogdanov, A.; Kivshar, Y. Asymmetric Metasurfaces with High-Q Resonances Governed by Bound States in the Continuum. *Phys. Rev. Lett.* **2018**, *121* (19), 193903.
(110) Han, Z.; Ding, F.; Cai, Y.; Levy, U. Significantly enhanced second-harmonic generations with all-dielectric antenna array working in the quasi-bound states in the continuum and excited by linearly polarized plane waves. *Nanophotonics* **2021**, *10* (3), 1189−1196.
(111) Moretti, G. Q.; Cortes, E.; Maier, S. A.; Bragas, A. V.; Grinblat, G. Engineering gallium phosphide nanostructures for efficient nonlinear photonics and enhanced spectroscopies. *Nanophotonics* **2021**, DOI: 10.1515/nanoph-2021-0388.
(112) Ning, T.; Li, X.; Zhang, Z.; Huo, Y.; Yue, Q.; Zhao, L.; Gao, Y. Ultimate conversion efficiency of second harmonic generation in all-dielectric resonators of quasi-BICs in consideration of nonlinear refraction of dielectrics. *Opt. Express* **2021**, *29* (11), 17286−17294.
(113) Gandhi, H. K.; Rocco, D.; Carletti, L.; De Angelis, C. Gain-loss engineering of bound states in the continuum for enhanced nonlinear response in dielectric nanocavities. *Opt. Express* **2020**, *28* (3), 3009−3016.
(114) Frizyuk, K.; Volkovskaya, I.; Smirnova, D.; Poddubny, A.; Petrov, M. Second-harmonic generation in Mie-resonant dielectric nanoparticles made of noncentrosymmetric materials. *Phys. Rev. B: Condens. Matter Mater. Phys.* **2019**, *99* (7), 075425.
(115) Huang, Z.; Lu, H.; Xiong, H.; Li, Y.; Chen, H.; Qiu, W.; Guan, H.; Dong, J.; Zhu, W.; Yu, J.; Luo, Y.; Zhang, J.; Chen, Z. Fano Resonance on Nanostructured Lithium Niobate for Highly Efficient and Tunable Second Harmonic Generation. *Nanomaterials* **2019**, *9* (1), 69.
(116) Kang, L.; Bao, H.; Werner, D. H. Efficient second-harmonic generation in high Q-factor asymmetric lithium niobate metasurfaces. *Opt. Lett.* **2021**, *46* (3), 633−636.
(117) Timbrell, D.; You, J. W.; Kivshar, Y. S.; Panoiu, N. C. A comparative analysis of surface and bulk contributions to second-harmonic generation in centrosymmetric nanoparticles. *Sci. Rep.* **2018**, *8* (1), 3586.
(118) Carletti, L.; Locatelli, A.; Neshev, D.; De Angelis, C. Shaping the Radiation Pattern of Second-Harmonic Generation from AlGaAs Dielectric Nanoantennas. *ACS Photonics* **2016**, *3* (8), 1500−1507.
(119) Xu, L.; Rahmani, M.; Smirnova, D.; Zangeneh Kamali, K.; Zhang, G.; Neshev, D.; Miroshnichenko, A. Highly-Efficient Longitudinal Second-Harmonic Generation from Doubly-Resonant AlGaAs Nanoantennas. *Photonics* **2018**, *5* (3), 29.
(120) Rocco, D.; Gigli, C.; Carletti, L.; Marino, G.; Vincenti, M. A.; Leo, G.; De Angelis, C. Vertical Second Harmonic Generation in Asymmetric Dielectric Nanoantennas. *IEEE Photonics J.* **2020**, *12* (3), 1−7.
(121) Gigli, C.; Marino, G.; Artioli, A.; Rocco, D.; De Angelis, C.; Claudon, J.; Gérard, J.-M.; Leo, G. Tensorial phase control in nonlinear meta-optics. *Optica* **2021**, *8* (2), 269.
(122) Shcherbakov, M. R.; Shorokhov, A. S.; Neshev, D. N.; Hopkins, B.; Staude, I.; Melik-Gaykazyan, E. V.; Ezhov, A. A.; Miroshnichenko, A. E.; Brener, I.; Fedyanin, A. A.; Kivshar, Y. S. Nonlinear Interference and Tailorable Third-Harmonic Generation from Dielectric Oligomers. *ACS Photonics* **2015**, *2* (5), 578−582.
(123) Yang, Y.; Wang, W.; Boulesbaa, A.; Kravchenko, I. I.; Briggs, D. P.; Puretzky, A.; Geohegan, D.; Valentine, J. Nonlinear Fano-Resonant Dielectric Metasurfaces. *Nano Lett.* **2015**, *15* (11), 7388−7393.
(124) Shorokhov, A. S.; Melik-Gaykazyan, E. V.; Smirnova, D. A.; Hopkins, B.; Chong, K. E.; Choi, D. Y.; Shcherbakov, M. R.; Miroshnichenko, A. E.; Neshev, D. N.; Fedyanin, A. A.; Kivshar, Y. S. Multifold Enhancement of Third-Harmonic Generation in Dielectric Nanoparticles Driven by Magnetic Fano Resonances. *Nano Lett.* **2016**, *16* (8), 4857−61.
(125) Melik-Gaykazyan, E. V.; Shcherbakov, M. R.; Shorokhov, A. S.; Staude, I.; Brener, I.; Neshev, D. N.; Kivshar, Y. S.; Fedyanin, A. A. Third-harmonic generation from Mie-type resonances of isolated all-dielectric nanoparticles. *Philos. Trans. R. Soc., A* **2017**, *375* (2090), 20160281.
(126) Chen, S.; Rahmani, M.; Li, K. F.; Miroshnichenko, A.; Zentgraf, T.; Li, G.; Neshev, D.; Zhang, S. Third Harmonic Generation Enhanced by Multipolar Interference in Complementary Silicon Metasurfaces. *ACS Photonics* **2018**, *5* (5), 1671−1675.
(127) Melik-Gaykazyan, E. V.; Kruk, S. S.; Camacho-Morales, R.; Xu, L.; Rahmani, M.; Zangeneh Kamali, K.; Lamprianidis, A.; Miroshnichenko, A. E.; Fedyanin, A. A.; Neshev, D. N.; Kivshar, Y. S. Selective Third-Harmonic Generation by Structured Light in Mie-Resonant Nanoparticles. *ACS Photonics* **2018**, *5* (3), 728−733.
(128) Deka, J.; Jha, K. K.; Menon, S.; Lal Krishna, A. S.; Biswas, R.; Raghunathan, V. Microscopic study of resonant third-harmonic generation from amorphous silicon nanodisk arrays. *Opt. Lett.* **2018**, *43* (21), 5242−5245.
(129) Kroychuk, M. K.; Yagudin, D. F.; Shorokhov, A. S.; Smirnova, D. A.; Volkovskaya, I. I.; Shcherbakov, M. R.; Shvets, G.; Kivshar, Y. S.; Fedyanin, A. A. Tailored Nonlinear Anisotropy in Mie-Resonant Dielectric Oligomers. *Adv. Opt. Mater.* **2019**, *7* (20), 1900447.
(130) Okhlopkov, K. I.; Shafirin, P. A.; Ezhov, A. A.; Orlikovsky, N. A.; Shcherbakov, M. R.; Fedyanin, A. A. Optical Coupling between Resonant Dielectric Nanoparticles and Dielectric Nanowires Probed by Third Harmonic Generation Microscopy. *ACS Photonics* **2019**, *6* (1), 189−195.
(131) Shcherbakov, M. R.; Werner, K.; Fan, Z.; Talisa, N.; Chowdhury, E.; Shvets, G. Photon acceleration and tunable broadband harmonics generation in nonlinear time-dependent metasurfaces. *Nat. Commun.* **2019**, *10* (1), 1345.
(132) Shi, L.; Evlyukhin, A. B.; Reinhardt, C.; Babushkin, I.; Zenin, V. A.; Burger, S.; Malureanu, R.; Chichkov, B. N.; Morgner, U.; Kovacev, M. Progressive Self-Boosting Anapole-Enhanced Deep-Ultraviolet Third Harmonic During Few-Cycle Laser Radiation. *ACS Photonics* **2020**, *7* (7), 1655−1661.

https://doi.org/10.1021/acsphotonics.1c01356
ACS Photonics XXXX, XXX, XXX−XXX

(133) Kroychuk, M. K.; Shorokhov, A. S.; Yagudin, D. F.; Shilkin, D. A.; Smirnova, D. A.; Volkovskaya, I.; Shcherbakov, M. R.; Shvets, G.; Fedyanin, A. A. Enhanced Nonlinear Light Generation in Oligomers of Silicon Nanoparticles under Vector Beam Illumination. *Nano Lett.* **2020**, *20* (5), 3471−3477.
(134) Tognazzi, A.; Okhlopkov, K. I.; Zilli, A.; Rocco, D.; Fagiani, L.; Mafakheri, E.; Bollani, M.; Finazzi, M.; Celebrano, M.; Shcherbakov, M. R.; Fedyanin, A. A.; De Angelis, C. Third-harmonic light polarization control in magnetically resonant silicon metasurfaces. *Opt. Express* **2021**, *29*, 11605−11612.
(135) Shibanuma, T.; Grinblat, G.; Albella, P.; Maier, S. A. Efficient Third Harmonic Generation from Metal-Dielectric Hybrid Nanoantennas. *Nano Lett.* **2017**, *17* (4), 2647−2651.
(136) Xu, L.; Rahmani, M.; Zangeneh Kamali, K.; Lamprianidis, A.; Ghirardini, L.; Sautter, J.; Camacho-Morales, R.; Chen, H.; Parry, M.; Staude, I.; Zhang, G.; Neshev, D.; Miroshnichenko, A. E. Boosting third-harmonic generation by a mirror-enhanced anapole resonator. *Light: Sci. Appl.* **2018**, *7*, 44.
(137) Grinblat, G.; Li, Y.; Nielsen, M. P.; Oulton, R. F.; Maier, S. A. Enhanced Third Harmonic Generation in Single Germanium Nanodisks Excited at the Anapole Mode. *Nano Lett.* **2016**, *16* (7), 4635−40.
(138) Grinblat, G.; Li, Y.; Nielsen, M. P.; Oulton, R. F.; Maier, S. A. Efficient Third Harmonic Generation and Nonlinear Subwavelength Imaging at a Higher-Order Anapole Mode in a Single Germanium Nanodisk. *ACS Nano* **2017**, *11* (1), 953−960.
(139) Semmlinger, M.; Zhang, M.; Tseng, M. L.; Huang, T.-T.; Yang, J.; Tsai, D. P.; Nordlander, P.; Halas, N. J. Generating Third Harmonic Vacuum Ultraviolet Light with a TiO2Metasurface. *Nano Lett.* **2019**, *19*, 8972−8978.
(140) Smirnova, D. A.; Khanikaev, A. B.; Smirnov, L. A.; Kivshar, Y. S. Multipolar Third-Harmonic Generation Driven by Optically Induced Magnetic Resonances. *ACS Photonics* **2016**, *3* (8), 1468−1476.
(141) Schinke, C.; Christian Peest, P.; Schmidt, J.; Brendel, R.; Bothe, K.; Vogt, M. R.; Kröger, I.; Winter, S.; Schirmacher, A.; Lim, S.; Nguyen, H. T.; MacDonald, D. Uncertainty analysis for the coefficient of band-to-band absorption of crystalline silicon. *AIP Adv.* **2015**, *5* (6), 067168.
(142) Pierce, D. T.; Spicer, W. E. Electronic Structure of Amorphous Si from Photoemission and Optical Studies. *Phys. Rev. B* **1972**, *5* (8), 3017−3029.
(143) Li, H. H. Refractive index of silicon and germanium and its wavelength and temperature derivatives. *J. Phys. Chem. Ref. Data* **1980**, *9* (3), 561−658.
(144) Hon, N. K.; Soref, R.; Jalali, B. The third-order nonlinear optical coefficients of Si, Ge, and Si1−xGex in the midwave and longwave infrared. *J. Appl. Phys.* **2011**, *110* (1), 011301.
(145) Narayanan, K.; Preble, S. F. Optical nonlinearities in hydrogenated-amorphous silicon waveguides. *Opt. Express* **2010**, *18*, 8998−9005.
(146) Amotchkina, T.; Trubetskov, M.; Hahner, D.; Pervak, V. Characterization of e-beam evaporated Ge, YbF3, ZnS, and LaF3 thin films for laser-oriented coatings. *Appl. Opt.* **2020**, *59* (5), A40−A47.
(147) Connell, G. A. N.; Temkin, R. J.; Paul, W. Amorphous germanium III. Optical properties. *Adv. Phys.* **1973**, *22* (5), 643−665.
(148) Zilli, A.; Rocco, D.; Finazzi, M.; Di Francescantonio, A.; Duò, L.; Gigli, C.; Marino, G.; Leo, G.; De Angelis, C.; Celebrano, M. Frequency Tripling via Sum-Frequency Generation at the Nanoscale. *ACS Photonics* **2021**, *8*, 1175−1182.
(149) Zappettini, A.; D'Amore, F.; Pietralunga, S. M.; Terio, A.; Martinelli, M.; Bliss, D. F.; Callahan, M. J. Wavelength dependence of the third order non-linear coefficient in hydrothermally grown ZnO crystals. *physica status solidi (c)* **2004**, *1* (4), 997−1000.
(150) Siefke, T.; Kroker, S.; Pfeiffer, K.; Puffky, O.; Dietrich, K.; Franta, D.; Ohlídal, I.; Szeghalmi, A.; Kley, E. B.; Tünnermann, A. Materials Pushing the Application Limits of Wire Grid Polarizers further into the Deep Ultraviolet Spectral Range. *Adv. Opt. Mater.* **2016**, *4* (11), 1780−1786.
(151) Ratzsch, S.; Kley, E. B.; Tunnermann, A.; Szeghalmi, A. Influence of the oxygen plasma parameters on the atomic layer deposition of titanium dioxide. *Nanotechnology* **2015**, *26* (2), 024003.
(152) Guan, X.; Hu, H.; Oxenlowe, L. K.; Frandsen, L. H. Compact titanium dioxide waveguides with high nonlinearity at telecommunication wavelengths. *Opt. Express* **2018**, *26* (2), 1055−1063.
(153) Semmlinger, M.; Zhang, M.; Tseng, M. L.; Huang, T. T.; Yang, J.; Tsai, D. P.; Nordlander, P.; Halas, N. J. Generating Third Harmonic Vacuum Ultraviolet Light with a TiO2Metasurface. *Nano Lett.* **2019**, *19* (12), 8972−8978.
(154) Miroshnichenko, A. E.; Evlyukhin, A. B.; Yu, Y. F.; Bakker, R. M.; Chipouline, A.; Kuznetsov, A. I.; Luk'yanchuk, B.; Chichkov, B. N.; Kivshar, Y. S. Nonradiating anapole modes in dielectric nanoparticles. *Nat. Commun.* **2015**, *6*, 8069.
(155) Yang, Y.; Miroshnichenko, A. E.; Kostinski, S. V.; Odit, M.; Kapitanova, P.; Qiu, M.; Kivshar, Y. S. Multimode directionality in all-dielectric metasurfaces. *Phys. Rev. B: Condens. Matter Mater. Phys.* **2017**, *95* (16), 165426.
(156) Yang, Y.; Bozhevolnyi, S. I. Nonradiating anapole states in nanophotonics: from fundamentals to applications. *Nanotechnology* **2019**, *30* (20), 204001.
(157) Yin, Y.; Yao, J.; Ye, L.; Cai, G.; Liu, Q. H. Tailoring Third Harmonic Generation From Anapole Mode in a Metal-Dielectric Hybrid Nanoantenna. *IEEE Photonics J.* **2021**, *13* (4), 1−6.
(158) Koshelev, K.; Tang, Y.; Li, K.; Choi, D.-Y.; Li, G.; Kivshar, Y. Nonlinear Metasurfaces Governed by Bound States in the Continuum. *ACS Photonics* **2019**, *6* (7), 1639−1644.
(159) Xu, L.; Zangeneh Kamali, K.; Huang, L.; Rahmani, M.; Smirnov, A.; Camacho-Morales, R.; Ma, Y.; Zhang, G.; Woolley, M.; Neshev, D.; Miroshnichenko, A. E. Dynamic Nonlinear Image Tuning through Magnetic Dipole Quasi-BIC Ultrathin Resonators. *Adv. Sci. (Weinh)* **2019**, *6* (15), 1802119.
(160) Carletti, L.; Kruk, S. S.; Bogdanov, A. A.; De Angelis, C.; Kivshar, Y. High-harmonic generation at the nanoscale boosted by bound states in the continuum. *Physical Review Research* **2019**, *1* (2), 023016.
(161) Gandolfi, M.; Tognazzi, A.; Rocco, D.; De Angelis, C.; Carletti, L. Near-unity third-harmonic circular dichroism driven by a quasibound state in the continuum in asymmetric silicon metasurfaces. *Phys. Rev. A: At., Mol., Opt. Phys.* **2021**, *104*, 023524.
(162) Wang, L.; Kruk, S.; Xu, L.; Rahmani, M.; Smirnova, D.; Solntsev, A.; Kravchenko, I.; Neshev, D.; Kivshar, Y. Shaping the third-harmonic radiation from silicon nanodimers. *Nanoscale* **2017**, *9* (6), 2201−2206.
(163) Eden, J. G. High-Order Harmonic Generation and Other Intense Optical Field-Matter Interactions: Review of Recent Experimental and Theoretical Advances. *Prog. Quantum Electron.* **2004**, *28*, 197−246.
(164) Ghimire, S.; DiChiara, A. D.; Sistrunk, E.; Agostini, P.; DiMauro, L. F.; Reis, D. A. Observation of high-order harmonic generation in a bulk crystal. *Nat. Phys.* **2011**, *7* (2), 138−141.
(165) Ginsberg, J. S.; Overvig, A. C.; Jadidi, M. M.; Malek, S. C.; Patwardhan, G. N.; Swenson, N.; Yu, N.; Gaeta, A. L. Enhanced harmonic generation in gases using an all-dielectric metasurface. *Nanophotonics* **2020**, *10* (1), 733−740.
(166) Vampa, G.; McDonald, C. R.; Orlando, G.; Klug, D. D.; Corkum, P. B.; Brabec, T. Theoretical analysis of high-harmonic generation in solids. *Phys. Rev. Lett.* **2014**, *113* (7), 073901.
(167) Liu, H.; Guo, C.; Vampa, G.; Zhang, J. L.; Sarmiento, T.; Xiao, M.; Bucksbaum, P. H.; Vučković, J.; Fan, S.; Reis, D. A. Enhanced high-harmonic generation from an all-dielectric metasurface. *Nat. Phys.* **2018**, *14* (10), 1006−1010.
(168) Zograf, G.; Koshelev, K.; Zalogina, A.; Korolev, V.; Choi, D.-Y.; Zürch, M.; Spielmann, C.; Luther-Davies, B.; Kartashov, D.; Makarov, S.; Kruk, S.; Kivshar, Y. High-harmonic generation from metasurfaces empowered by bound states in the continuum. *arXiv:2008.11481* **2020**, na.

https://doi.org/10.1021/acsphotonics.1c01356
ACS Photonics XXXX, XXX, XXX−XXX

(169) An, J.-K.; Kim, K.-H. Efficient non-perturbative high-harmonic generation from nonlinear metasurfaces with low pump intensity. *Opt. Laser Technol.* **2021**, *135*, 106702.
(170) Salem, R.; Foster, M. A.; Turner, A. C.; Geraghty, D. F.; Lipson, M.; Gaeta, A. L. Signal regeneration using low-power four-wave mixing on silicon chip. *Nat. Photonics* **2008**, *2* (1), 35−38.
(171) Wadsworth, W. J.; Joly, N.; Knight, J. C.; Birks, T. A.; Biancalana, F.; Russell, P. S. J. Supercontinuum and four-wave mixing with Q-switched pulses in endlessly single-mode photonic crystal fibres. *Opt. Express* **2004**, *12*, 299−309.
(172) Wang, Y.; Lin, C.-Y.; Nikolaenko, A.; Raghunathan, V.; Potma, E. O. Four-wave mixing microscopy of nanostructures. *Adv. Opt. Photonics* **2011**, *3* (1), 1−52.
(173) Takesue, H.; Inoue, K. Generation of polarization-entangled photon pairs and violation of Bell's inequality using spontaneous four-wave mixing in a fiber loop. *Phys. Rev. A: At., Mol., Opt. Phys.* **2004**, *70* (3), 031802.
(174) Grinblat, G.; Li, Y.; Nielsen, M. P.; Oulton, R. F.; Maier, S. A. Degenerate Four-Wave Mixing in a Multiresonant Germanium Nanodisk. *ACS Photonics* **2017**, *4* (9), 2144−2149.
(175) Colom, R.; Xu, L.; Marini, L.; Bedu, F.; Ozerov, I.; Begou, T.; Lumeau, J.; Miroshnishenko, A. E.; Neshev, D.; Kuhlmey, B. T.; Palomba, S.; Bonod, N. Enhanced Four-Wave Mixing in Doubly Resonant Si Nanoresonators. *ACS Photonics* **2019**, *6* (5), 1295−1301.
(176) Camacho-Morales, R.; Xu, L.; Dimitrov, N.; Stoyanov, L.; Ma, Z.; Dreischuh, A. A.; Tan, H. H. H.; De Angelis, C.; Jagadish, C.; Miroshnichenko, A. E.; Rocco, D.; Gili, V. F.; Komar, A.; Lysevych, M.; Karouta, F.; Leo, G.; Rahmani, M.; Neshev, D. N. Infrared upconversion imaging in nonlinear metasurfaces. *Advanced Photonics* **2021**, *3* (03), 036002.
(177) Kamali, S. M.; Arbabi, E.; Arbabi, A.; Faraon, A. A review of dielectric optical metasurfaces for wavefront control. *Nanophotonics* **2018**, *7* (6), 1041−1068.
(178) Liu, B.; Sain, B.; Reineke, B.; Zhao, R.; Meier, C.; Huang, L.; Jiang, Y.; Zentgraf, T. Nonlinear Wavefront Control by Geometric-Phase Dielectric Metasurfaces: Influence of Mode Field and Rotational Symmetry. *Adv. Opt. Mater.* **2020**, *8* (9), 1902050.
(179) Kruk, S.; Wang, L.; Sain, B.; Dong, Z.; Yang, J.; Zentgraf, T.; Kivshar, Y. Asymmetric parametric generation of images with nonlinear dielectric metasurfaces. *arXiv:2108.04425* **2021**, na.
(180) Remesh, V.; Grinblat, G.; Li, Y.; Maier, S. A.; van Hulst, N. F. Coherent Multiphoton Control of Gallium Phosphide Nanodisk Resonances. *ACS Photonics* **2019**, *6* (10), 2487−2491.
(181) Fan, Y.; Wang, Y.; Zhang, N.; Sun, W.; Gao, Y.; Qiu, C. W.; Song, Q.; Xiao, S. Resonance-enhanced three-photon luminesce via lead halide perovskite metasurfaces for optical encoding. *Nat. Commun.* **2019**, *10* (1), 2085.
(182) Li, G. C.; Xiang, J.; Zhang, Y. L.; Deng, F.; Panmai, M.; Zhuang, W.; Lan, S.; Lei, D. Mapping the Magnetic Field Intensity of Light with the Nonlinear Optical Emission of a Silicon Nanoparticle. *Nano Lett.* **2021**, *21* (6), 2453−2460.
(183) Fan, Y.; Tonkaev, P.; Wang, Y.; Song, Q.; Han, J.; Makarov, S. V.; Kivshar, Y.; Xiao, S. Enhanced Multiphoton Processes in Perovskite Metasurfaces. *Nano Lett.* **2021**, *21*, 7191.
(184) Cui, T.; Zhang, M.; Zhao, Y.; Yang, Y.; Bai, B.; Sun, H. B. Near-field nonlinear imaging of an anapole mode beyond diffraction limit. *Opt. Lett.* **2021**, *46* (9), 2095−2098.
(185) Makarov, S. V.; Zalogina, A. S.; Tajik, M.; Zuev, D.; Rybin, M. V.; Kuchmizhak, A. A.; Juodkazis, S.; Kivshar, Y. Light-Induced Tuning and Reconfiguration of Nanophotonic Structures. *Laser and Photonics Reviews* **2017**, *11*, 1700108.
(186) Grinblat, G.; Berte, R.; Nielsen, M. P.; Li, Y.; Oulton, R. F.; Maier, S. A. Sub-20 fs All-Optical Switching in a Single Au-Clad Si Nanodisk. *Nano Lett.* **2018**, *18* (12), 7896−7900.
(187) del Coso, R.; Solis, J. Relation between nonlinear refractive index and third-order susceptibility in absorbing media. *J. Opt. Soc. Am. B* **2004**, *21*, 640−644.
(188) Della Valle, G.; Hopkins, B.; Ganzer, L.; Stoll, T.; Rahmani, M.; Longhi, S.; Kivshar, Y. S.; De Angelis, C.; Neshev, D. N.; Cerullo, G. Nonlinear Anisotropic Dielectric Metasurfaces for Ultrafast Nanophotonics. *ACS Photonics* **2017**, *4* (9), 2129−2136.
(189) Grinblat, G.; Nielsen, M. P.; Dichtl, P.; Li, Y.; Oulton, R. F.; Maier, S. A. Ultrafast sub-30 fs all-optical switching based on gallium phosphide. *Science Advances* **2019**, *5*, eaaw3262.
(190) Shcherbakov, M. R.; Liu, S.; Zubyuk, V. V.; Vaskin, A.; Vabishchevich, P. P.; Keeler, G.; Pertsch, T.; Dolgova, T. V.; Staude, I.; Brener, I.; Fedyanin, A. A. Ultrafast all-optical tuning of direct-gap semiconductor metasurfaces. *Nat. Commun.* **2017**, *8* (1), 17.
(191) Xu, Y.; Sun, J.; Frantz, J.; Shalaev, M. I.; Walasik, W.; Pandey, A.; Myers, J. D.; Bekele, R. Y.; Tsukernik, A.; Sanghera, J. S.; Litchinitser, N. M. Reconfiguring structured light beams using nonlinear metasurfaces. *Opt. Express* **2018**, *26* (23), 30930−30943.
(192) Xu, Y.; Sun, J.; Frantz, J.; Shalaev, M.; Walasik, W.; Pandey, A.; Myers, J.; Bekele, R.; Tsukernik, A.; Litchinitser, J. Nonlinear Metasurface for Structured Light with Tunable Orbital Angular Momentum. *Appl. Sci.* **2019**, *9* (5), 958.
(193) Ozawa, T.; Price, H. M.; Amo, A.; Goldman, N.; Hafezi, M.; Lu, L.; Rechtsman, M. C.; Schuster, D.; Simon, J.; Zilberberg, O.; Carusotto, I. Topological photonics. *Rev. Mod. Phys.* **2019**, *91* (1), 015006.
(194) Hasan, M. Z.; Kane, C. L. Colloquium: Topological insulators. *Rev. Mod. Phys.* **2010**, *82* (4), 3045−3067.
(195) Nakahara, M. *Geometry, Topology and Physics*; IOP Publishing, 2003.
(196) Kane, C. L. Topological Band Theory and the Z2 Invariant. *Topological Insulators* **2013**, *6*, 3−34.
(197) Su, W. P.; Schrieffer, J. R.; Heeger, A. J. Solitons in Polyacetylene. *Phys. Rev. Lett.* **1979**, *42* (25), 1698−1701.
(198) Smirnova, D.; Kruk, S.; Leykam, D.; Melik-Gaykazyan, E.; Choi, D. Y.; Kivshar, Y. Third-Harmonic Generation in Photonic Topological Metasurfaces. *Phys. Rev. Lett.* **2019**, *123* (10), 103901.
(199) Kruk, S. S.; Gao, W.; Choi, D. Y.; Zentgraf, T.; Zhang, S.; Kivshar, Y. Nonlinear Imaging of Nanoscale Topological Corner States. *Nano Lett.* **2021**, *21* (11), 4592−4597.
(200) Smirnova, D.; Leykam, D.; Chong, Y.; Kivshar, Y. Nonlinear topological photonics. *Appl. Phys. Rev.* **2020**, *7* (2), 021306.
(201) Busschaert, S.; Reimann, R.; Cavigelli, M.; Khelifa, R.; Jain, A.; Novotny, L. Transition Metal Dichalcogenide Resonators for Second Harmonic Signal Enhancement. *ACS Photonics* **2020**, *7* (9), 2482−2488.
(202) Nauman, M.; Yan, J.; de Ceglia, D.; Rahmani, M.; Zangeneh Kamali, K.; De Angelis, C.; Miroshnichenko, A. E.; Lu, Y.; Neshev, D. N. Tunable Unidirectional Nonlinear Emission from transition-metal-dichalcogenide metasurfaces. *Nat. Commun.* **2021**, *12*, na.
(203) Antropov, I. M.; Popkova, A. A.; Tselikov, G. I.; Ermolaev, G. A.; Ozerov, I.; Bedu, F.; Kirtaev, R. V.; Novikov, S. M.; Evlyukhin, A. B.; Arsenin, A. V.; Bessonov, V. O.; Volkov, V. S.; Fedyanin, A. A. Double-resonant second-harmonic generation in MoS_2 nanoantennas. *arXiv:2105.04985* **2021**, na.
(204) Abdelwahab, I.; Dichtl, P.; Grinblat, G.; Leng, K.; Chi, X.; Park, I.-H.; Nielsen, M. P.; Oulton, R. F.; Loh, K. P.; Maier, S. A. Giant and Tunable Optical Nonlinearity in Single-Crystalline 2D Perovskites due to Excitonic and Plasma Effects. *Adv. Mater.* **2019**, *31*, 1902685.
(205) Abdelwahab, I.; Grinblat, G.; Leng, K.; Li, Y.; Chi, X.; Rusydi, A.; Maier, S. A.; Loh, K. P. Highly Enhanced Third-Harmonic Generation in 2D Perovskites at Excitonic Resonances. *ACS Nano* **2018**, *12* (1), 644−650.
(206) Yuan, Q.; Fang, L.; Fang, H.; Li, J.; Wang, T.; Jie, W.; Zhao, J.; Gan, X. Second Harmonic and Sum-Frequency Generations from a Silicon Metasurface Integrated with a Two-Dimensional Material. *ACS Photonics* **2019**, *6* (9), 2252−2259.
(207) Deka, J.; Dandu, M.; Krishna, A. S. L.; Menon, S.; Jyothsna, K. M.; Biswas, R.; Majumdar, K.; Raghunathan, V. Polarization independent enhancement of zeroth order diffracted second harmonic from multilayer gallium selenide on a silicon resonant metasurface. *Opt. Express* **2020**, *28* (24), 35695−35707.

https://doi.org/10.1021/acsphotonics.1c01356
ACS Photonics XXXX, XXX, XXX−XXX

(208) Löchner, F. J. F.; George, A.; Koshelev, K.; Bucher, T.; Najafidehaghani, E.; Fedotova, A.; Choi, D.-Y.; Pertsch, T.; Staude, I.; Kivshar, Y.; Turchanin, A.; Setzpfandt, F. Hybrid Dielectric Metasurfaces for Enhancing Second-Harmonic Generation in Chemical Vapor Deposition Grown MoS2Monolayers. *ACS Photonics* **2021**, *8* (1), 218−227.
(209) Bernhardt, N.; Koshelev, K.; White, S. J. U.; Meng, K. W. C.; Froch, J. E.; Kim, S.; Tran, T. T.; Choi, D. Y.; Kivshar, Y.; Solntsev, A. S. Quasi-BIC Resonant Enhancement of Second-Harmonic Generation in WS2Monolayers. *Nano Lett.* **2020**, *20* (7), 5309−5314.
(210) Liu, Z.; Wang, J.; Chen, B.; Wei, Y.; Liu, W.; Liu, J. Giant Enhancement of Continuous Wave Second Harmonic Generation from Few-Layer GaSe Coupled to High-Q Quasi Bound States in the Continuum. *Nano Lett.* **2021**, *21*, 7405.
(211) Salary, M. M.; Farazi, S.; Mosallaei, H. A Dynamically Modulated All-Dielectric Metasurface Doublet for Directional Harmonic Generation and Manipulation in Transmission. *Adv. Opt. Mater.* **2019**, *7* (23), 1900843.
(212) Lee, K.; Park, J.; Kang, B. J.; Kim, W. T.; Kim, H. D.; Baek, S.; Ahn, K. J.; Min, B.; Rotermund, F. Electrically Controllable Terahertz Second-Harmonic Generation in GaAs. *Adv. Opt. Mater.* **2020**, *8* (18), 2000359.
(213) Lee, K.-T.; Taghinejad, M.; Yan, J.; Kim, A. S.; Raju, L.; Brown, D. K.; Cai, W. Electrically Biased Silicon Metasurfaces with Magnetic Mie Resonance for Tunable Harmonic Generation of Light. *ACS Photonics* **2019**, *6* (11), 2663−2670.
(214) Kravtsov, V.; Khestanova, E.; Benimetskiy, F. A.; Ivanova, T.; Samusev, A. K.; Sinev, I. S.; Pidgayko, D.; Mozharov, A. M.; Mukhin, I. S.; Lozhkin, M. S.; Kapitonov, Y. V.; Brichkin, A. S.; Kulakovskii, V. D.; Shelykh, I. A.; Tartakovskii, A. I.; Walker, P. M.; Skolnick, M. S.; Krizhanovskii, D. N.; Iorsh, I. V. Nonlinear polaritons in a monolayer semiconductor coupled to optical bound states in the continuum. *Light: Sci. Appl.* **2020**, *9* (1), 56.
(215) Grinblat, G.; Abdelwahab, I.; Nielsen, M. P.; Dichtl, P.; Leng, K.; Oulton, R. F.; Loh, K. P.; Maier, S. A. Ultrafast All-Optical Modulation in 2D Hybrid Perovskites. *ACS Nano* **2019**, *13* (8), 9504−9510.
(216) Mazzanti, A.; Pogna, E. A. A.; Ghirardini, L.; Celebrano, M.; Schirato, A.; Marino, G.; Lemaitre, A.; Finazzi, M.; De Angelis, C.; Leo, G.; Cerullo, G.; Della Valle, G. All-Optical Modulation with Dielectric Nanoantennas: Multi-Resonant Control and Ultrafast Spatial Inhomogeneities. *Small Science* **2021**, *1*, 2000079.
(217) Lemasters, R.; Shcherbakov, M. R.; Yang, G.; Song, J.; Lian, T.; Harutyunyan, H.; Shvets, G. Deep Optical Switching on Subpicosecond Timescales in an Amorphous Ge Metamaterial. *Adv. Opt. Mater.* **2021**, *9*, 2100240.
(218) Pogna, E. A. A.; Celebrano, M.; Mazzanti, A.; Ghirardini, L.; Carletti, L.; Marino, G.; Schirato, A.; Viola, D.; Laporta, P.; De Angelis, C.; Leo, G.; Cerullo, G.; Finazzi, M.; Della Valle, G. Ultrafast, All Optically Reconfigurable, Nonlinear Nanoantenna. *ACS Nano* **2021**, *15*, 11150−11157.
(219) Marino, G.; Solntsev, A. S.; Xu, L.; Gili, V. F.; Carletti, L.; Poddubny, A. N.; Rahmani, M.; Smirnova, D. A.; Chen, H.; Lemaître, A.; Zhang, G.; Zayats, A. V.; De Angelis, C.; Leo, G.; Sukhorukov, A. A.; Neshev, D. N. Spontaneous photon-pair generation from a dielectric nanoantenna. *Optica* **2019**, *6* (11), 1416.
(220) Nikolaeva, A.; Frizyuk, K.; Olekhno, N.; Solntsev, A.; Petrov, M. Directional emission of down-converted photons from a dielectric nanoresonator. *Phys. Rev. A: At., Mol., Opt. Phys.* **2021**, *103* (4), 043703.
(221) Parry, M.; Mazzanti, A.; Poddubny, A. N.; Valle, G. D.; Neshev, D. N.; Sukhorukov, A. A. Enhanced generation of nondegenerate photon pairs in nonlinear metasurfaces. *Advanced Photonics* **2021**, *3*, 055001.

https://doi.org/10.1021/acsphotonics.1c01356
ACS Photonics XXXX, XXX, XXX−XXX